TESI DI DOTTORATO

UNIVERSITÀ DEGLI STUDI DI NAPOLI FEDERICO II

DIPARTIMENTO DI INGEGNERIA BIOMEDICA, ELETTRONICA
E DELLE TELECOMUNICAZIONI

DOTTORATO DI RICERCA IN
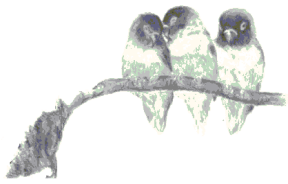INGEGNERIA ELETTRONICA E DELLE TELECOMUNICAZIONI

Electromagnetic Models for the Retrieval of Surface Parameters through SAR Images

ANTONIO NATALE

Il Coordinatore del Corso di Dottorato   Il Tutore
Ch.mo Prof. Niccolò Rinaldi   Ch.mo Prof. Antonio Iodice

ANNO ACCADEMICO 2010/2011

Don't worry about a thing
'cause every little thing's gonna be alright...

Contents

Introduction

"The Earth is blue. How wonderful. It is amazing."

This is how Y. A. Gagarin reported to Ground Control during his spacewalk around our planet, on April 1961.

Starting from then, we observe the Earth and we try to understand more and more how it is and how it changes.

To this aim, in the last decades the spatial agencies have planned several missions to explore the space and, in particular, to monitor our planet.

Actually, a great amount of data relevant to the Earth surface is available today and, of course, much more than the beauty of its colors and shapes can be deduced exploiting this information.

As a matter of fact, remote sensing instruments are the best candidates to provide, in a comparatively short time, useful information about wide areas of any part in the world. The potentialities implied in these data, as usual, lie in the use we make of them; therefore, the opportunity to observe a quantity of interest through the remote sensing instruments depends on the performances of the technique employed for the information mining.

Nowadays, several private or public institutions, such as the Civil Defense, require the knowledge of many ground physical parameters i.e., permittivity, ground roughness, soil moisture content, vegetation biomass-index, and so on. In particular, the soil moisture content represents a key parameter in the hydrological cycle, indeed it determines the repartition of the rainfalls into the surface run-off, seepage and evapotranspiration. Hence, the knowledge on the space-temporal behavior of the soil moisture content is a fundamental information in several applications as in predicting rivers floods, rainfalls and landslides.

As the deep bond between the soil moisture content and the soil permittivity, then it is possible to estimate the former starting from the retrieval of the ground dielectric constant. However, this opportunity can be exploited on condition that a proper model is used to describe

how the permittivity affects the electromagnetic field scattered from the ground and measured by the sensor; moreover, the estimation technique should be able to separate the scattering field effects due to the permittivity from those owing to the other parameters involved in the scattering process.

Of course, such a model should be as reliable and realistic as possible in describing the scattering phenomena, but at the same time not too involved, in order to allow the parameters inversion. Unfortunately, most of already existing simple methods, like the Small Perturbation Method (SPM) or the Physical Optics (PO), do not take into account depolarization and cross-polarization effects, so it is necessary to attain a new model which provides a good matching with measured data, at the same time retaining an acceptable complexity.

Accordingly, the key goal of this thesis lies in the modeling of the electromagnetic scattering from bare soils and its usage to perform the ground permittivity, soil moisture content and surface roughness retrieval from polarimetric Synthetic Aperture Radar (SAR) data.

So, in Chapter 1 the operating principles of SAR are presented, in order to give an idea of what is the SAR image employed in the retrieving procedure and in which way such signal depends on the observed scene. By the way, in Chapter 2 the fundamental concepts of the polarimetry are outlined, with particular emphasis to the analytical tools used to describe the polarimetric scattering and to the classical scattering solutions from bare soils. The first innovative contribution of this thesis is presented in this section and regards the physical meaning of the Kirchhoff solution for the scattering from both classical and fractal surfaces. In Chapter 3 some of the principal mixing models employed to relate the ground permittivity to the soil moisture content are instead shown.

Chapter 4 is devoted to illustrate the main theoretical contribution presented in this thesis, that is the Polarimetric Two-Scale Model (PTSM) developed to describe the scattering from a bare soil surface. In order to account for de-polarization and cross-polarization phenomena observed in real data, a two-scale description of the scattering surface is here considered. In particular, the surface is assumed to be composed by rough randomly-tilted facets, which give rise to a random drift of the local incidence angle and a random rotation of the local incidence plane. Unlike other existing approaches, the PTSM accounts for both these effects, which come straight from

the surface model; moreover, the model allows to express the Normalized Radar Cross Sections (NRCS) for the whole surface by averaging over the facets slopes the power density relevant to a single facet. The prediction on the diffuse field provided by such NRCS represents the key concept on which the estimate procedure is founded. Accordingly, in Chapter 5 a retrieval algorithm able to return retrieval maps from measured co-polar and cross-polar ratio is proposed.

An idea of its performances and the PTSM validation is given by applying the retrieval procedure on a wide variety of SAR data acquired at different bands and exploiting, when possible, in "situ" measurements.

Chapter 1

SAR: Operating Principles

This chapter is intended to recall the basic principles on which a Synthetic Aperture Radar (SAR) is founded.

In particular, here we will focus on the system operating in the StripMap mode, for which the observation of the scene is performed by not varying the antenna beam direction during the sensor flight.

The chapter is organized as follows: first section is addressed to describe the pulse response of the SAR, while the transfer function of the system, useful to perform an efficient simulation and processing of SAR raw data, is evaluated in the second section; finally, some constraints on system design are discussed in the last section.

1.1   SAR point-spread function

In order to evaluate the point-spread function, we need a simple model to describe how the sensor acquires data as it goes along its trajectory of flight. To this aim, let us assume that the sensor moves with velocity $\underline{v}$ and that during its flight it illuminates an area on the ground, whose extent depends on the sensor height, as well as on both the electrical size and the tilt of the antenna.

This geometry can be effectively described in a system of cylindrical coordinates (see Fig. 1.1), in which the distance r (slant range) between the line-of-flight and a scattering point P on the ground, the elevation angle ϑ through which the sensor sees the ground-point and finally the position x (azimuth) of P along the axis of flight, are represented.

During the flight, the sensor periodically transmits microwave pulses that hit the target and return in the backscattering direction after the round-trip time.

A frequency modulated pulse is usually employed to get a better geometric range resolution Δr, with respect to the one obtained considering unmodulated pulses.

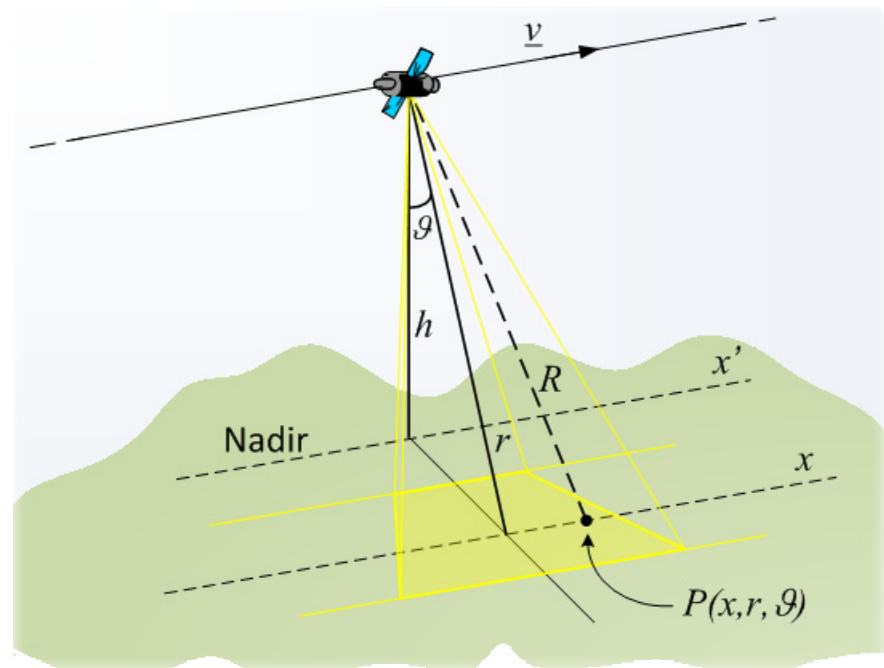**Figure 1.1: geometry of SAR acquisition.**

Indeed, for unmodulated pulses, it results:

$$\Delta r = \frac{c\tau}{2} \quad ,$$

(1.1)

where c the speed of light, τ is the pulse duration and factor 2 accounts for the round-trip propagation [1].

Of course, from (1.1), an improvement in resolution requires a reduction of the pulse width τ and high peak power for prescribed mean power operation.

Therefore, in order to overcome this limitation, the pulse transmitted by a SAR is usually a chirp, whose complex envelope can be expressed as:

$$p(t - t_n) = \exp\left\{ j\frac{\alpha}{2}(t - t_n)^2 \right\} rect\left(\frac{t - t_n}{\tau}\right) \quad , \quad \text{with } |t - t_n| < \frac{\tau}{2}, \tag{1.2}$$

where t_n represents the transmission time and α is the modulation factor.

It can be shown that, after the pulse compression processing, the range resolution of a chirp decreases with its duration, as it is equal to

$$\Delta r = \frac{c}{2} T_{chirp} = \frac{c}{2} \frac{1}{B_{chirp}} = \frac{c}{2} \frac{2\pi}{\alpha\tau} \quad , \tag{1.3}$$

with T_{chirp} and B_{chirp} representing, respectively, the significant duration of the chirp auto-correlation function and the chirp bandwidth [2].

The range resolution gain got transmitting a chirp instead of an unmodulated pulse is then $\rho_{range} = (\pi c)/(\alpha\tau)$.
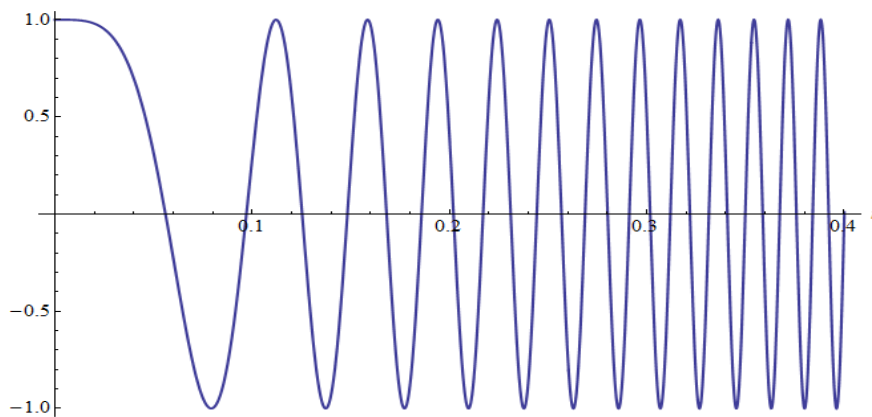

Figure 1.2: chirp waveform for $\tau = 0.4$ s and $\alpha = 10^3$ s^{-2}.

So, assuming that the transmitted pulse is a chirp, the signal backscattered by the target and received onboard, after the heterodyne, is given by:

$$f_{Rx}\left(t-t_n-\frac{2R}{c}\right)=W^2\left(\frac{x'-x}{X}\right)p\left(t-t_n-\frac{2R}{c}\right)\exp\left\{-j\frac{\omega}{c}2R\right\} \quad , \tag{1.4}$$

where x' is the sensor position, $R=\sqrt{(x-x')^2+r^2}$, $\omega=2\pi f$ is the angular frequency with f the carrier frequency (λ is the carrier wavelength), W is a function representing the antenna radiation pattern and X is the footprint, i.e. the synthetic antenna dimension.
As we are interested in geometric resolutions, at this stage it is convenient to express the received signal in function of space coordinates, so, after the substitution $t-t_n=2r'/c$, (1.4) can be expressed as:

$$f_{Rx}(x'-x,r',r)=W^2\left(\frac{x'-x}{X}\right)p\left(\frac{2r'}{c}-\frac{2R}{c}\right)\exp\left\{-j\frac{4\pi}{\lambda}R\right\} \quad , \tag{1.5}$$

that represents the SAR point-spread function, or pulse response.

1.2   SAR transfer function

Once the SAR pulse response is known, it is possible to express the signal pertinent to an extended scene by superimposing all the elementary returns. Accordingly, the SAR raw signal is

$$h(x',r')=\iint dx\,dr\,\gamma(x,r)f_{Rx}(x'-x,r',r) \quad , \tag{1.6}$$

where the weighting function $\gamma(x,r)$ is the reflectivity pattern, which accounts for both the electromagnetic properties and the acquisition geometry of each of the scattering points in the sensed scene. In particular, $\gamma(x,r)$ is related to the Normalized Radar Cross Section [3], that will be defined in next chapter.

Of course, the ultimate goal of SAR remote sensing is to get the best estimate of the reflectivity function from the raw data (SAR focusing).

As shown afterwards, a possible and efficient way to meet this task is to process SAR raw data in the frequency domain.

Starting from (1.5) and (1.6), let's define $\tilde{\gamma}(x,r) = \gamma(x,r)\exp\{-j\,4\pi r/\lambda\}$, $\Delta r = R - r$ and

$$g(x'-x, r'-r, r) = W^2\left(\frac{x'-x}{X}\right)p\left[\frac{2(r'-r-\Delta r)}{c}\right]\exp\left\{-j\frac{4\pi}{\lambda}\Delta r\right\} \quad , \qquad (1.7)$$

whence (1.6) becomes

$$h(x', r') = \iint dx\,dr\,\tilde{\gamma}(x,r)g(x'-x, r'-r, r) \quad , \qquad (1.8)$$

from which it is possible to express the Fourier Transform of the raw signal:

$$H(\xi,\eta) = \iint dx\,dr\,G(\xi,\eta;r)\tilde{\gamma}(x,r)\exp\{-j(\xi x + \eta r)\} \quad , \qquad (1.9)$$

where $G(\cdot)$ is the space-variant (i.e., range-variant) SAR Transfer Function:

$$G(\xi,\eta,r) = \iint dx'\,dr'\,g(x'-x, r'-r, r)\exp\{-j[\xi(x'-x) + \eta(r'-r)]\} \quad , \qquad (1.10)$$

whose asymptotic evaluation can be computed using the stationary phase method, due to the presence of the fast varying phase term [1]. Accordingly, by letting $b = 2\alpha/c^2$,

$$\begin{cases} u = x' - x \\ w = r' - r - \Delta r \end{cases} \qquad (1.11)$$

and

$$\begin{cases} \psi_1(u) = \xi u + \dfrac{4\pi}{\lambda}\Delta r\left(1 + \dfrac{\eta\lambda}{4\pi}\right) \\[4mm] \psi_2(w) = \eta w - \dfrac{2\alpha}{c^2}w^2 = \eta w - bw^2 \end{cases} \quad , \qquad (1.12)$$

equation (1.9) can be rewritten as follows:

$$G(\xi,\eta,r) = \iint du\,dw\,W^2\left(\frac{u}{X}\right)rect\left(\frac{2w}{c\tau}\right)\exp\{-j\psi_1(u)\}\exp\{-j\psi_2(w)\} \quad . \qquad (1.13)$$

The derivatives of phase terms in (1.12) vanishes in correspondence of the stationary points u_S and w_S equal to:

$$\begin{cases} u_S = -\dfrac{r\xi}{\sqrt{\left(\dfrac{4\pi}{\lambda}\right)^2\left(1+\dfrac{\eta\lambda}{4\pi}\right)^2-\xi^2}} \quad , \\[2em] w_S = \dfrac{\eta}{2b} \end{cases} \qquad (1.14)$$

which allows to attain in closed form the SAR transfer function as follows

$$G(\xi,\eta,r) \cong rect\left(\frac{2w_S}{c\tau}\right)W^2\left(\frac{u_S}{X}\right)\exp\{-j\psi_1(u_s)\}\exp\{-j\psi_2(w_s)\} \quad . \qquad (1.15)$$

At this stage, by setting $a=(2\pi)/(r_0\lambda)$, with r_0 slant range at the center of the footprint, and reasonably assuming that the antenna pattern is substantially constant within the footprint (i.e., substantially independent on the range coordinate), the transfer function can be expressed as:

$$G(\xi,\eta,r) = rect\left(\frac{\eta}{bc\tau}\right)W^2\left(\frac{\xi}{2aX}\right)\exp\{-j\psi(\xi,\eta,r)\} \quad , \qquad (1.16)$$

where the only space-variance is due to the following phase term

$$\psi(\xi,\eta,r) = \frac{\eta^2}{4b} - \frac{\dfrac{\xi^2}{4a}\dfrac{r}{r_0}}{\left(1+\dfrac{\eta\lambda}{4\pi}\right)} \quad . \qquad (1.17)$$

Of course, it is possible to consider the r-invariant transfer function at the center of the scene $G_0(\xi,\eta)=G(\xi,\eta,r_0)$, through which it is possible to express the raw signal in a very effective way:

$$H(\xi,\eta)=G_0(\xi,\eta)\iint dx\,dr\,\widetilde{\gamma}(x,r)\exp\{-j(\xi x+\eta r)\}\exp\{-jK(\xi,\eta,r)\} \quad , \qquad (1.18)$$

with

$$K(\xi,\eta,r)=-\frac{\xi^2}{4ar_0\left(1+\dfrac{\eta\lambda}{4\pi}\right)}(r-r_0) \quad . \qquad (1.19)$$

The only space-variant phase term K in (1.18) exhibits a linear dependence on the range coordinate and so it can be included in the Fourier kernel in (1.18). This leads to the expression on which is founded the efficient focusing

$$H(\xi,\eta)=G_0(\xi,\eta)\exp\{jK(\xi,\eta,0)\}\widetilde{\Gamma}(\xi,\eta+K(\xi,\eta,0)) \quad , \qquad (1.20)$$

being $\widetilde{\Gamma}(\xi,\eta+K(\xi,\eta,0))$ the Fourier Transform of $\widetilde{\gamma}(\cdot)$ computed on the grid $(\xi,\eta+K(\xi,\eta,0))$ instead of the grid (ξ,η).

From (1.20) it follows that it is possible to account for the system space-variance (and then perform an efficient processing in the frequency domain) simply balancing the above mentioned grid deformation, i.e. inserting an interpolation-resampling block in the focus processor (Figure 1.3).

Notice that the output of the "interpolation and sampling" block is

$$\hat{\Gamma}(\xi',\eta')=\widetilde{\Gamma}(\xi',\eta')rect\left(\frac{\xi'}{2aX}\right)rect\left(\frac{\eta'}{bc\tau}\right) \quad , \qquad (1.21)$$

which can be useful to get an idea of the low-pass-filtering imposed by the SAR on the reflectivity. Accordingly, the estimate of the reflectivity function is the inverse Fourier Transform of (1.21), i.e. the convolution

$$\hat{\gamma}(x,r)=\iint dx'\,dr'\,\widetilde{\gamma}(x',r')\text{sinc}[aX(x-x')]\text{sinc}\left[b\frac{c\tau}{2}(r-r')\right] \quad , \qquad (1.22)$$

whence it is possible to express the astigmatism degree of the system (i.e., the energy amount spread by a point on its neighbors in the recovered signal).

$$h(x',r')$$

$$2D\text{-FFT}$$

$$H(\xi,\eta)$$

$$e^{-jK(\xi,\eta,0)}G_0^{-1}(\xi,\eta) \longrightarrow \otimes$$

$$\hat{\Gamma}\big(\xi,\eta+K(\xi,\eta,0)\big)$$

Interpolation
&
Resampling

$$\hat{\Gamma}(\xi',\eta')$$

$$2D\text{-IFFT}$$

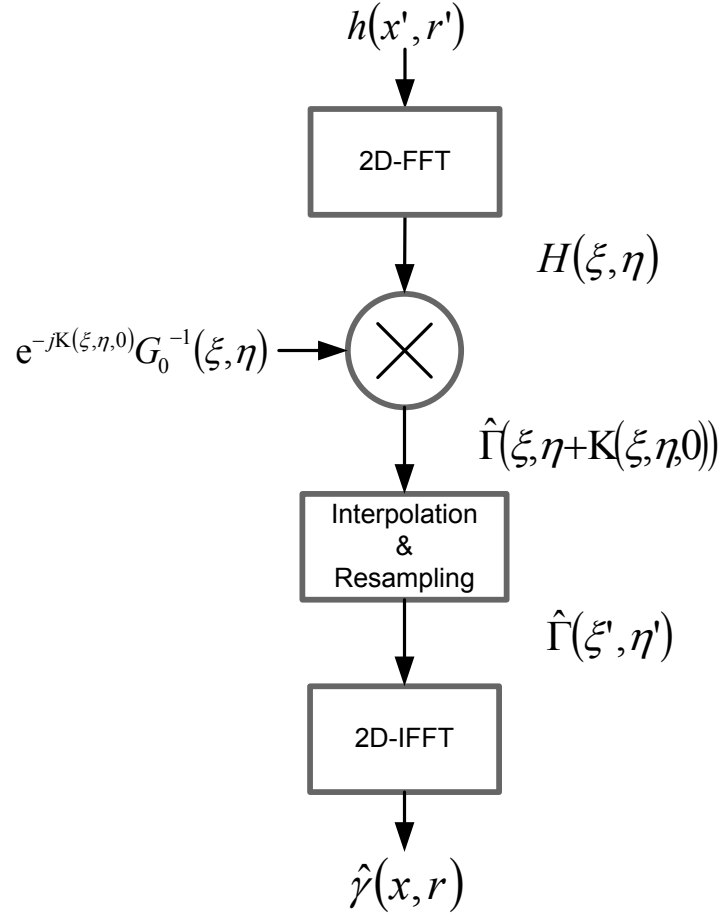$$\hat{\gamma}(x,r)$$

Figure 1.3: block scheme of the efficient SAR focusing.

A quantitative measure of this spreading can be obtained considering $\tilde{\gamma}(x',r') = \delta(x'-\bar{x}, r'-\bar{r})$ (where δ is the Dirac pulse), and so the focused signal is:

$$i(x,r) = \mathrm{sinc}\big[aX(x-\bar{x})\big]\mathrm{sinc}\left[b\frac{c\tau}{2}(r-\bar{r})\right] \quad . \tag{1.23}$$

As it appears from (1.23), the only ground scattering-point spreads its energy over a wider region in the reconstructed signal, whose width is determined by the SAR spatial resolution (i.e., the 3 dB width of the sinc function):

$$\begin{cases} \Delta r = \dfrac{2\pi}{bc\tau} = \dfrac{c}{2}\dfrac{1}{B_{chirp}} = \dfrac{cT_{chirp}}{2} \\[2ex] \Delta x = \dfrac{\pi}{aX} = \dfrac{L}{2} \end{cases} , \qquad (1.24)$$

where L is the antenna dimension in the azimuth direction and is related to the footprint by the relation $X \cong r_0 \lambda / L$.

As already mentioned in Paragraph 1, first of (1.24) is the range resolution attainable transmitting a chirp waveform instead of an unmodulated pulse.

Concerning the second of (1.24), it is the azimuth resolution for the considered SAR system. Its value, if compared to what obtainable using a RAR (Real Aperture Radar, i.e., a radar not performing the synthetic antenna) yield to an azimuth resolution gain equal to $\rho_{azimuth} = (4r_0\lambda)/(L^2)$, which explains the reason to employ SAR systems instead of RAR ones.

1.3   Constraints on the system design

Starting from (1.23), it is possible to compute the spatial bandwidths for the considered SAR systems:

$$\begin{cases} B_{range} = \dfrac{2}{c}B_{chirp} \\[2ex] B_{azimuth} = \dfrac{2}{L} \end{cases} . \qquad (1.25)$$

Of course, the system transmitting rate (i.e., the pulse-repetition frequency prf) should be larger than the azimuth temporal bandwidth,

that is $prf>2|\underline{v}|/L$, and this provides a practical lower-bound on the azimuth resolution in order to avoid a huge computational charge [4].

Moreover, sensors usually employ a circulator to switch from the transmission period to the reception one so, to avoid that received pulses reach the platform during the transmission stage, the prf cannot be chosen too large. In particular, the time required to receive the signal pertinent to the whole scene is $T_r \cong \tau + 2Ssin\vartheta_0/c \cong Ssin\vartheta_0/c$, where S is the ground-range coverage (swath), which leads to a further constraint on the pulse-repetition frequency $prf<1/T_r$, that is a lower bound on the antenna size in the across-track direction $D>2\lambda(prf/c)r_0 tan\vartheta_0$.

References

[1] G. Franceschetti, R. Lanari, "*Synthetic Aperture Radar Processing*", CRC Press, Boca Raton (FL), 1999.

[2] A. Hein, "*Processing of SAR data: fundamentals, signal processing and interferometry*", Springer, Berlin, 2004.

[3] G. Franceschetti, M. Migliaccio, D. Riccio, G. Schirinzi, "SARAS: a Synthetic Aperture Radar (SAR) raw signal simulator", *IEEE Transactions on Geoscience and Remote Sensing*, Vol. 30, No 1, January 1992.

[4] G. Rees, "*Physical Principles of Remote Sensing*", Cambridge University Press, Cambridge, 2001.

Chapter 2

Classical Models for the Polarimetric Scattering

Since the ultimate goal of SAR systems is to get the best estimate of the reflectivity function $\gamma(x,r)$, then describing how the properties of the sensed scene affect the diffuse field is a fundamental step to correctly interpret information provided by SAR data.

By the way, as mentioned in previous chapter, the reflectivity function can be linked to the Normalized Radar Cross Section (NRCS); this quantity is deducible from the output of a radar system and its expression depends on the second order statistics of the backscattered field measured by the sensor. Accordingly, this chapter is addressed to recall some basilar concepts of polarimetric scattering from natural surfaces and it is organized as follows: first paragraph is devoted to outline the mathematical representation of the polarimetric scattering, quoting the rigorous definition of scattering coefficients and NRCS; in second section the principal results provided by classical – analytical – models for the scattering evaluation are instead reported, together with a new interpretation of the Kirchhoff scattering integral.

2.1 Polarimetric concepts for the scattering problem

2.1.1 Polarization state of a plane wave

The space-time behavior of electromagnetic waves is ruled by the Maxwell equations, whose solution, fixed the sources and the boundary conditions, allows to completely express the electromagnetic field propagating in the considered space.

In particular, among all the possible solutions of the wave equation, the simplest one is relevant to a linear, source-free, homogeneous, isotropic and spatially nondispersive medium, referred as plane wave solution.

According to these assumptions, the electric field of a plane wave can be represented in the frequency domain as:

$$\underline{E}(\underline{r}) = \underline{E}_0 \exp\{- j\underline{k} \cdot \underline{r}\} \ , \tag{2.1}$$

where $\underline{E}_0$ is the constant complex amplitude vector, $\underline{r}$ is the position vector and $\underline{k}$ is the wave vector, that defines the direction of propagation and satisfies the relations $\underline{k} \cdot \underline{k} = \omega^2 \varepsilon \mu$, $\underline{k} \cdot \underline{E}_0 = 0$, with ω being the angular frequency of the monochromatic wave, and ε and μ the medium electric permittivity and magnetic permeability, respectively.

Although the plane wave is the simplest solution of the wave equation, it permits to introduce the concept of the polarization state of an electromagnetic wave, which is intrinsically linked to its vectorial nature. Hence, introducing an arbitrary orthogonal coordinate system (h,v,k), the field vector can be decomposed in two complex orthogonal components

$$\underline{E}_0 = E_h \hat{h} + E_v \hat{v} \ , \tag{2.2}$$

leading to the following time representation of the electric field:

$$\underline{e}(\underline{r},t) = \mathrm{Re}\{\underline{E}(\underline{r})\exp(- j\omega t)\} = \begin{cases} e_h(\underline{r},t) = |E_h|\cos(\omega t - \underline{k} \cdot \underline{r} + \varphi_h) \\ e_v(\underline{r},t) = |E_v|\cos(\omega t - \underline{k} \cdot \underline{r} + \varphi_v) \end{cases} , \tag{2.3}$$

wherein φ_h and φ_v are, respectively, the phase terms of E_h and E_v.
Equation (2.3) defines, for any fixed t, the spatial evolution of both the components of the electric field along the propagation direction $\hat{k}$ whose combination generally results in an helicoidal trajectory (Figs. 2.1 and 2.2).
Conversely, for any fixed $\underline{r}$, e_h and e_v represent the parametric components of an ellipse lying on the equi-phase plane. This means that the tip of the electric field vector moves in time on the equi-phase plane along the polarization ellipse, whose shape defines the polarization state of the monochromatic wave (Figure 2.3).
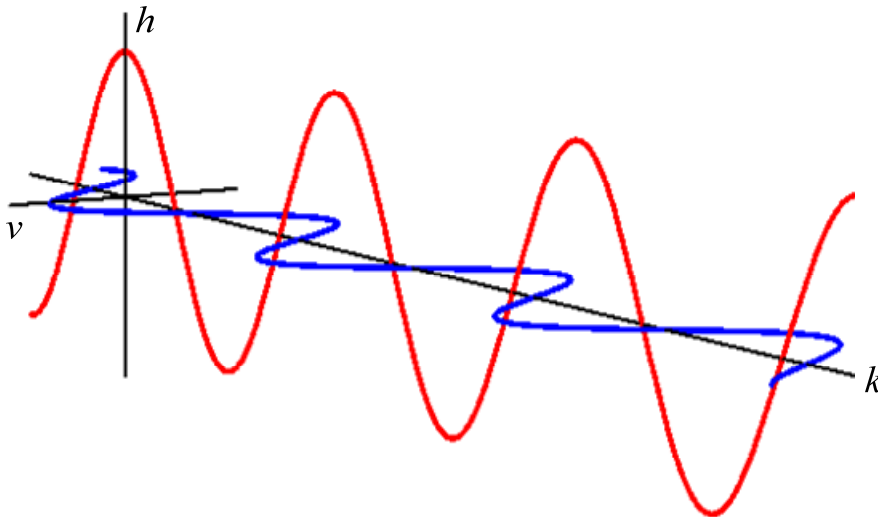

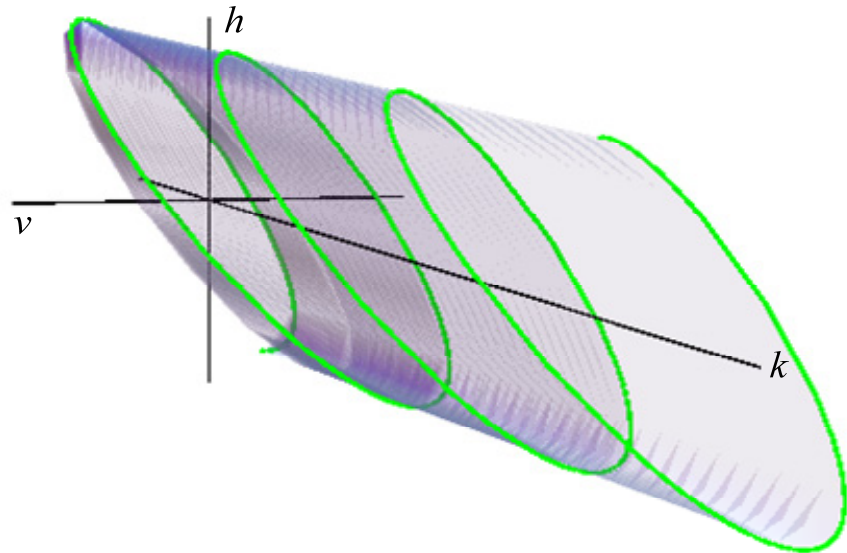**Figure 2.1: spatial evolution of the wave components at $t=t_0$.**

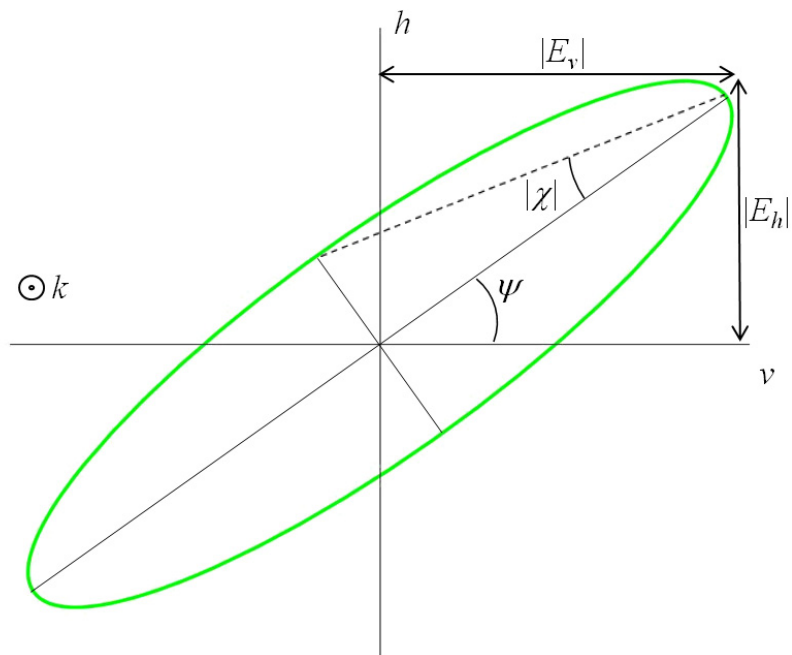**Figure 2.2: spatial evolution of a monochromatic plane wave at $t=t_0$.**

Figure 2.3: polarization ellipse at $\underline{r}=\underline{r}_0$.

The polarization state is completely described by giving both the magnitude and the phase of the two components E_h and E_v or, equivalently, by the orientation angle ψ and the ellipticity angle χ, defined as

$$\begin{cases} \psi = \dfrac{1}{2}\tan^{-1}\left(2\dfrac{|E_h E_v|}{|E_h|^2 - |E_v|^2}\cos(\varphi_h - \varphi_v) \right) & \in [0,\pi] \\[4mm] \chi = \dfrac{1}{2}\sin^{-1}\left(2\dfrac{|E_h E_v|}{|E_h|^2 + |E_v|^2}\sin(\varphi_h - \varphi_v) \right) & \in \left[-\dfrac{\pi}{4}, \dfrac{\pi}{4} \right] \end{cases} , \qquad (2.4)$$

The orientation angle expresses the inclination of the ellipse with respect to the v-axis. The ellipticity angle, instead, describes the shape of the ellipse: at $\chi=0$ the ellipse degenerates to a straight line (linear polarization state), while at $\chi=\pi/4$ the ellipse becomes a circle (circular polarization state). The ellipticity angle χ also defines the sense of rotation of the electric field vector: indeed, if χ is negative then the rotation is right-handed, while a clockwise rotation is due to a positive value of χ.

Notice that, even though the polarization state is completely defined by the orientation and ellipticity angle, a whole wave description needs the knowledge of the ellipse amplitude and the initial absolute phase reference, too. In particular, the ellipse amplitude A_0 is defined as the magnitude of the $\underline{E}$ vector, i.e.

$$A_0 = |\underline{E}_0| = \sqrt{|E_h|^2 + |E_v|^2} \quad . \qquad (2.5)$$

In addition, it is worthwhile highlighting that the polarization state is invariant with respect to the coordinate system used to describe it.

2.1.2 Stokes parameters and the Poincaré sphere

In the previous section, the representation of the polarization state of a plane wave has been presented in function of only two real parameters, i.e. the orientation and the ellipticity angles. Even so, the actual capability to fix these quantities depends on the knowledge about the parameters of the complex electric field vector.

Consequently, if the goal of a given system is to measure the polarization state of an electromagnetic wave, then this system must record both the amplitude and the phase of the wave.

The availability of coherent systems able to measure the amplitude and phase of the incoming waves is relatively recent. In the past, only non-coherent systems were available. These systems are only able to measure the power of an incoming wave. Consequently, it was necessary to characterize the polarization of a wave only by power measurements. This characterization is carried out by the so-called Stokes vector.

Accordingly, starting from the electric field vector, it is possible to define the Stokes parameters as

$$\underline{E}_0 \cdot \underline{E}_0^{\dagger} = \begin{bmatrix} |E_h|^2 & E_h E_v^* \\ E_h^* E_v & |E_v|^2 \end{bmatrix} = \frac{1}{2}\left(g_0 \sigma_0 + g_1 \sigma_1 + g_2 \sigma_2 + g_3 \sigma_3\right) \ , \qquad (2.6)$$

wherein † denotes the transposed conjugate while * denotes the conjugate,

$$\sigma_0 = \begin{bmatrix} 1 & 0 \\ 0 & 1 \end{bmatrix}, \sigma_1 = \begin{bmatrix} 1 & 0 \\ 0 & -1 \end{bmatrix}, \sigma_2 = \begin{bmatrix} 0 & 1 \\ 1 & 0 \end{bmatrix}, \sigma_3 = \begin{bmatrix} 0 & j \\ -j & 0 \end{bmatrix} \qquad (2.7)$$

is the Pauli matrices basis set and finally

$$\underline{g}_S = \begin{pmatrix} g_0 \\ g_1 \\ g_2 \\ g_3 \end{pmatrix} = \begin{pmatrix} |E_h|^2 + |E_v|^2 \\ |E_h|^2 - |E_v|^2 \\ 2\,\mathrm{Re}\{E_h E_v^*\} \\ -2\,\mathrm{Im}\{E_h E_v^*\} \end{pmatrix} = \begin{pmatrix} |E_h|^2 + |E_v|^2 \\ |E_h|^2 - |E_v|^2 \\ 2|E_h E_v|\cos(\varphi_h - \varphi_v) \\ 2|E_h E_v|\sin(\varphi_h - \varphi_v) \end{pmatrix} \qquad (2.8)$$

represents the definition of the Stokes vector [2].

It is evident that only three of the Stokes parameters are independent, since they are related by the identity

$$g_0^2 = g_1^2 + g_2^2 + g_3^2 \ \ . \qquad (2.9)$$

Moreover, from (2.9) it results that g_0 is proportional to the total density power of the wave, while the other parameters are related to the orientation angle and to the ellipticity angle by the following relation

$$(g_1, g_2, g_3)^T = A_0 (\cos 2\chi \cos 2\psi, \cos 2\chi \sin 2\psi, \sin 2\chi)^T \qquad , \qquad (2.10)$$

which indicates that g_0, g_1 and g_3 may be regarded as the Cartesian coordinates of a point P on a sphere of radius g_0.

Polarization Ellipse   Poincaré Sphere

$\chi=20.3°$, $\psi=39.7°$ $g_1=0.59$, $g_2=0.49$, $g_3=0.65$
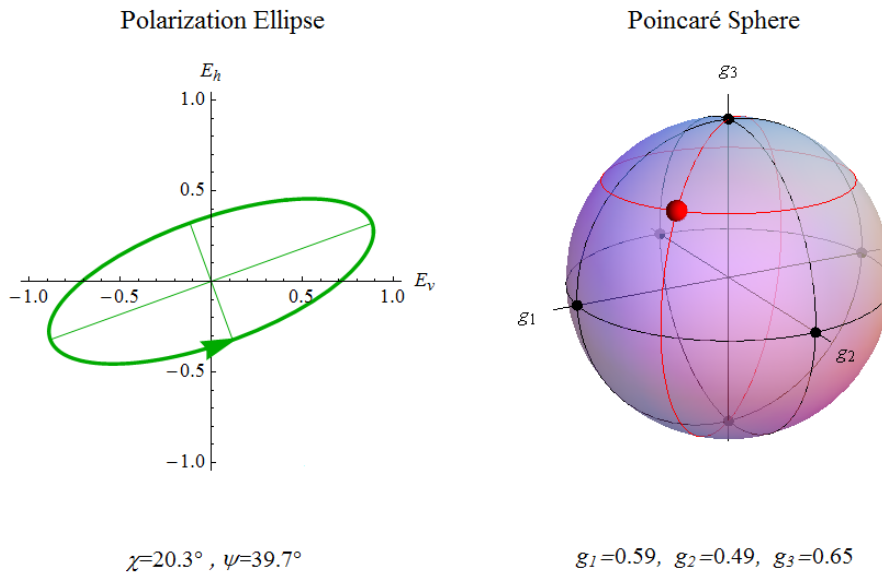
Figure 2.4: the Poincaré sphere and the polarization ellipse.

Thus, every possible polarization state of a plane monochromatic wave (of a fixed intensity g_0) corresponds to a point on this sphere and vice versa (see Fig. 2.4). This sphere is usually referred as the Poincaré sphere.

Since χ is positive or negative according as the polarization is right-handed or left-handed, it follows from (2.10) that counterclockwise polarization states are represented by points on the Poincaré sphere which lie above the equatorial plane (g_1, g_2 – plane), while clockwise polarization states by points which lie below this plane. Further, for linear polarization states $g_3=0$, and so these states are represented by

points in the equatorial plane. Concerning the circular polarization states, they are characterized by $g_1=g_2=0$, and so they are represented by the north-pole (right-handed) or the south-pole (left-handed).

2.1.3 Partially polarized waves

As stated up to here, the tip of the electric field vector of a monochromatic wave moves in time periodically along an exact trajectory defined by the polarization ellipse, which may, of course, reduce in special cases to a circle or straight line.

Therefore, in this case, the right position of the moving tip can be provided if the polarization state is known and so the wave is said completely polarized.

A second important class of waves are the so-called quasi monochromatic or partially polarized waves. Such waves can be considered as wave packets of multiple frequencies of a bandwidth centered at the mean wave frequency. In contrast to fully polarized waves, for which both the amplitude and the phase of the electric field are independent of time and space, partially polarized waves are characterized by temporally and/or spatially varying electric field amplitude, phase and polarization. Thus, the electric field vector no longer describes a well defined ellipse but one that varies in time.

In this case, polarization can be defined only in the sense of statistical averaging over time. To this aim, it is useful to introduce the concept coherence. Loosely speaking, the coherence of the field is its ability to maintain stable relationships linking amplitude and polarization with other reference fields as time elapses [1]; its quantitative measure can be provided by the coherency matrix

$$\underline{\underline{C}} = \left\langle \underline{E} \cdot \underline{E}^{\dagger} \right\rangle = \begin{bmatrix} \left\langle \left| E_h \right|^2 \right\rangle & \left\langle E_h E_v^{\ *} \right\rangle \\ \left\langle E_v E_h^{\ *} \right\rangle & \left\langle \left| E_v \right|^2 \right\rangle \end{bmatrix} , \tag{2.11}$$

which is an hermitian positive semi-definite matrix, whose entries are proportional to the second order moments of the components of the electric field.

The diagonal elements of the coherency matrix corresponds to the intensities of each of them, so that the trace of $\underline{\underline{C}}$ equals the total

intensity of the wave. The off-diagonal elements contain the cross-correlation between the components of the electric field vector and express the amount of correlated structure in the field. In absence of any correlation between E_h and E_v the matrix becomes diagonal with equal diagonal elements. In this case, the wave does not contain any polarized structure and is called totally unpolarized. Such a wave has only one degree of freedom, namely its amplitude. On the opposite, if the determinant of $\underline{\underline{C}}$ is equal to zero, the correlation between E_h and E_v is maximum, and the wave is completely polarized with three degrees of freedom (as in the case of monochromatic fields). Between these two limiting cases there lies the general one of a partially polarized wave (with four degrees of freedom), for which there is a certain amount of correlation between the h and v components. Accordingly, a synthetic measure of this amount is given by

$$\gamma = \frac{\left|\left\langle E_h E_v^* \right\rangle\right|}{\sqrt{\left\langle |E_h|^2 \right\rangle \left\langle |E_v|^2 \right\rangle}} = \frac{\left|\left\langle g_2 \right\rangle - j\left\langle g_3 \right\rangle\right|}{\sqrt{\left\langle g_0 \right\rangle^2 - \left\langle g_1 \right\rangle^2}} \quad , \tag{2.12}$$

which represents the degree of coherence of the wave and ranges from 0 (totally unpolarized waves) to 1 (completely polarized waves). Moreover, let's consider the identity

$$\left\langle g_0 \right\rangle^2 - \left\langle g_1 \right\rangle^2 - \left\langle g_2 \right\rangle^2 - \left\langle g_3 \right\rangle^2 = 4\left(\left\langle |E_h|^2 \right\rangle \left\langle |E_v|^2 \right\rangle - \left|\left\langle E_h E_v^* \right\rangle\right|^2 \right) \quad , \tag{2.13}$$

whence it is possible (being the right-hand side of (2.13) always nonnegative) to derive the relationship existing between the Stokes parameters in the most general case, i.e.

$$\left\langle g_0 \right\rangle^2 \geq \left\langle g_1 \right\rangle^2 + \left\langle g_2 \right\rangle^2 + \left\langle g_3 \right\rangle^2 \quad . \tag{2.14}$$

Previous inequality states that the total power of the wave is always greater than or equal to the intensity associated to its "polarized component" and that a partially polarized wave is represented by a point P lying within the Poincaré sphere (by the origin, if the wave is totally unpolarized, see Fig. 2.5).

Besides, from (2.14) it is straightforward to define the degree of polarization of a wave as the ratio:

$$\text{DoP} = \frac{\sqrt{\langle g_1 \rangle^2 + \langle g_2 \rangle^2 + \langle g_3 \rangle^2}}{\langle g_0 \rangle^2} \quad , \qquad\qquad (2.15)$$

related to the degree of coherence by the following

$$\left(1 - \text{DoP}^2\right) = \frac{\langle g_0 \rangle^2 - \langle g_1 \rangle^2}{\langle g_0 \rangle^2}\left(1 - \gamma^2\right) \qquad\qquad . \qquad\qquad (2.16)$$

completely polarized wave   totally unpolarized wave   partially polarized wave

$\gamma = \text{DoP} = 1$ $\gamma = \text{DoP} = 0$ $\gamma < 1 \quad \text{DoP} < 1$
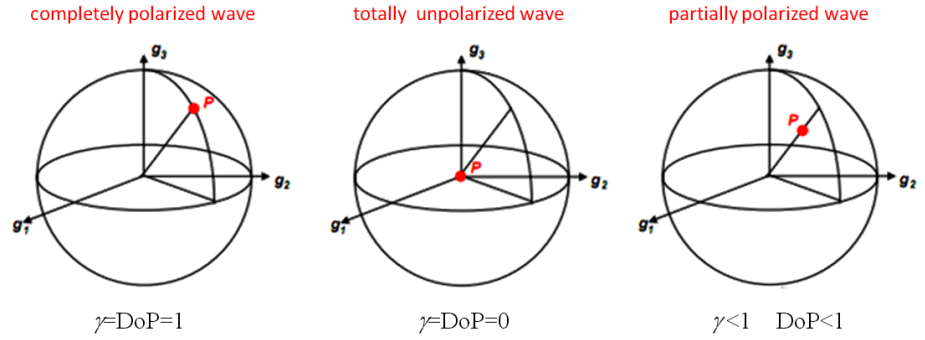
Figure 2.5: representation on the Poincaré sphere at the variance of the degree of polarization.

2.1.4 The polarimetric scattering problem

In previous sections, the main properties deriving from the vectorial nature of the electromagnetic field have been discussed.
At this stage, let us consider a wave that, during its travel along the direction $\hat{k}^i$, encounters a target and interacts with it (Figure 2.6).
As a consequence of this interaction, part of the energy carried by the incident wave is absorbed by the target itself, whereas the rest is reradiated as a new electromagnetic wave towards all directions; let us focalize our attention on one scattering direction $\hat{k}^s$. Of course, the properties of the scattered wave depend on the target and can be different from those of the incident one. Then, the question which rises at this point is to relate the scattered wave to the target: indeed,

once this relationship is supplied, the diffuse field could be employed to characterize or identify the target.
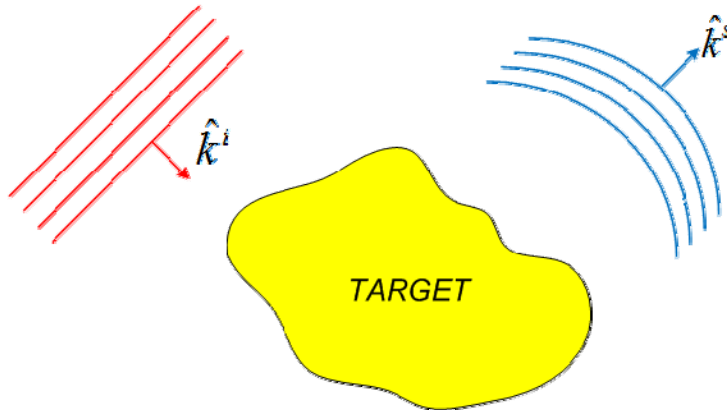

Figure 2.6: interaction between the wave and a target.

The most fundamental form to describe the interaction of an electromagnetic wave with a given target is the radar equation. This equation establishes the relation between the power which the target intercepts from the incident electromagnetic wave $\underline{E}^i$ and the power reradiated by the same target in the form of the scattered wave $\underline{E}^s$. The radar equation allows to express the power detected P_r at the receiving system as [1, 3-8]

$$P_r = \frac{P_t G_t}{4\pi R_t^2} \; \sigma \; \frac{A_r}{4\pi R_r^2} \quad , \tag{2.17}$$

where the first factor represents the amount of the transmitted power density impinging on the target (being P_t the transmitted power, G_t the transmitting antenna gain and R_t the distance between the transmitter and the target), the last factor represents the capability of the receiving system to catch power (being A_r the effective area of the receiver and R_r the distance between the target and receiver), while σ constitutes the target descriptor in such a power balance. As σ has units of an area, it represents the effective area which characterizes the target, from which its name, Radar Cross Sections (RCS), follows,

An important fact which arises at this point is the way the target reradiates the intercepted power in a given direction of the space.

In order to be independent of this property, the Radar Cross Section shall be referenced to and idealized isotropic scatterer. Thus, the RCS of an object is the cross section of an equivalent isotropic scatterer that generates the same scattered power density as the object in the observed direction

$$\sigma = 4\pi R^2 \frac{\left|\underline{E}^S\right|^2}{\left|\underline{E}^i\right|^2} = 4\pi R^2 \left|S\right|^2 \quad , \tag{2.18}$$

where S is the complex scattering amplitude of the object. The final value of σ is a function of a large number of parameters, among which the wave frequency, the wave polarization, both the incident and scattering directions, the geometry of the target and its dielectric properties.

It is worthwhile underlining that radar equation in (2.17) is valid for those cases in which the target of interest is smaller than the radar coverage, that is, a point target. For those targets presenting an extent larger than the radar coverage, a different model to represent the target is needed. Accordingly, in these situations, a target is represented as an infinite collection of statistically identical point targets (Fig. 2.7).
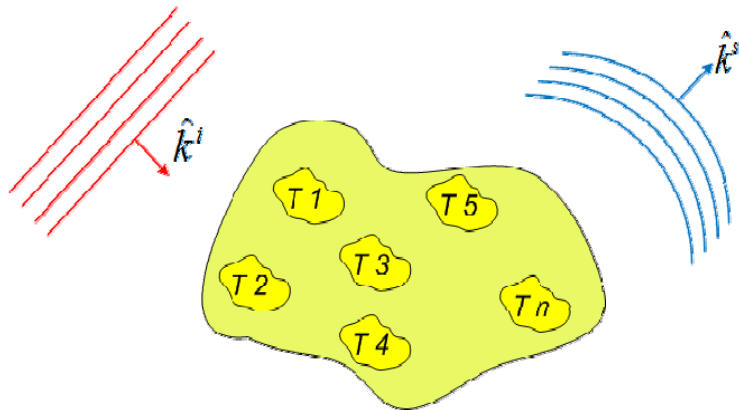

Figure 2.7: interaction between the wave and an extended target.

As a consequence, the resulting scattered field is due to the coherent summation of the scattered waves from every one of the independent targets which model the distributed scatterer. In order to express the scattering properties of the extended target independently of its extent, we consider every elementary target as being described by a differential Radar Cross Section $d\sigma$. Therefore, to separate the effects of the target extent, it useful to consider $d\sigma$ as the product of the averaged RCS per unit area σ^0 and the differential area ds occupied by the target.

Then, the differential power received by the systems due to an elementary scatterer can be written as

$$dP_r = \frac{P_t G_t}{4\pi R_t^2} \frac{A_r}{4\pi R_r^2} d\sigma \quad, \tag{2.19}$$

from which it is possible to obtain the total power received from the whole target integrating over the illuminated area A_0

$$P_r = \iint_{A_0} \frac{P_t G_t}{4\pi R_t^2} \frac{A_r}{4\pi R_r^2} \sigma^0 ds \quad. \tag{2.20}$$

Due the nature of the problem, (2.20) is to be intended in a statistical sense, according to the definition of the Normalized Radar Cross Section (NRCS) [1, 3-8]:

$$\sigma^0 = \frac{\langle \sigma \rangle}{A_0} = \frac{4\pi R^2}{A_0} \frac{\left\langle \left| \underline{E}^s \right|^2 \right\rangle}{\left| \underline{E}^i \right|^2} = \frac{4\pi}{A_0} \left\langle |S|^2 \right\rangle \quad. \tag{2.21}$$

As mentioned before, NRCS depends, among other things, on the polarization of both the incident and diffuse waves.

In order to express explicitly this dependence NRCS is usually defined as

$$\sigma_{pq}^{0} = \frac{\langle \sigma_{pq} \rangle}{A_0} = \frac{4\pi R^2}{A_0} \frac{\left\langle \left| \underline{E}_{pq}^{s} \right|^2 \right\rangle}{\left| \underline{E}_{q}^{i} \right|^2} = \frac{4\pi}{A_0} \left\langle \left| S_{pq} \right|^2 \right\rangle, \quad p,q \in \{h,v\} \ , \tag{2.22}$$

being p and q the polarizations of the incident and scattered field, respectively, and can each stand for h or v, while S_{pq} is the complex polarimetric scattering coefficient of the target.

These coefficients allow to express the scattering process by relating the diffuse field to the incident one in a very simple way. Indeed, by considering the polarimetric scattering matrix $\underline{\underline{S}}$, the following relation holds

$$\underline{E}^{S} = \begin{bmatrix} E_{h}^{s} \\ E_{v}^{s} \end{bmatrix} = \frac{e^{-jkR}}{R} \underline{\underline{S}} \cdot \underline{E}^{i} = \frac{e^{-jkR}}{R} \begin{bmatrix} S_{hh} & S_{hv} \\ S_{vh} & S_{vv} \end{bmatrix} \cdot \begin{bmatrix} E_{h}^{i} \\ E_{v}^{i} \end{bmatrix} \ , \tag{2.23}$$

from which it is possible to implicitly define the scattering coefficients as

$$S_{pq} = \left[\underline{\underline{S}} \right]_{pq} = R \frac{E_{p}^{s}}{E_{q}^{i}} \Bigg|_{\underline{E}^{i} = E_{q}^{i} \hat{q}} \ , \quad p,q \in \{h,v\} \ . \tag{2.24}$$

The diagonals elements of the scattering matrix receive the name of co-polar terms, since they relate the same polarization for the incident and the scattered fields. Nevertheless, the off-diagonal elements are known as cross-polar terms as they relate orthogonal polarization states. Finally, the common factor in (2.23) takes into account the propagation effects both in amplitude and phase. It must be taken into account that the relation expressed by (2.23) is only valid for the far field zone, where the planar wave assumption is considered for the incident and the scattered fields.

The polarimetric scattering matrix has, in the most general case and ignoring a common phase term, 7 real degrees of freedom, while in the backscattering case ($\hat{k}^{s} = -\hat{k}^{i}$), for reciprocal targets, result $S_{hv}=S_{vh}$ and so $\underline{\underline{S}}$ can be parameterized by only 5 real degrees of freedom.

Concerning the total scattered power, it is known as SPAN and it is defined as

$$\text{SPAN} = \left\langle \left| S_{hh} \right|^2 \right\rangle + \left\langle \left| S_{hv} \right|^2 \right\rangle + \left\langle \left| S_{vh} \right|^2 \right\rangle + \left\langle \left| S_{vv} \right|^2 \right\rangle \quad ; \qquad (2.25)$$

unlike the scattering matrix, it can be proved that the SPAN does not depend on the basis employed to represent the polarization state of the wave.

2.1.5 Polarimetric decompositions

The Normalized Radar Cross Sections as well as the scattering coefficients, depend on both the geometrical and electrical parameters of they observed target. This dependence, for a given target, may change in function of the polarimetric channel and so, in principle, it is possible to extract some features about the scatterer performing a polarimetric analysis [6-8].

To this purpose, the polarimetric decomposition techniques can be used: they allow reorganizing the information associated to the different polarimetric channels in order to have a simpler interpretation of the scattering mechanisms.

The key concept of target decompositions may be summarized by the following theorem [9]:

"A general distributed target may be decomposed into the sum of three single targets";

this means that, whatever the considered distributed target is, then it is possible to associate to it three simple scattering mechanisms (relevant to the three single targets). Accordingly, decomposition techniques allow us to extract the basic features of a general distributed target in order to facilitate the interpretation of its electromagnetic response.

There are several techniques to decompose a target [10], in both the coherent and incoherent way, depending on wheter they are performed on the scattering matrix or on the coherence or covariance scattering matrices.

The objective of the coherent decompositions is to express the measured scattering matrix by the radar as a the combination of the scattering responses of simpler objects, that is

$$\underline{\underline{S}} = \sum_{i=1}^{3} w_i \underline{\underline{S}}_i \quad . \tag{2.26}$$

In (2.26), the symbol $\underline{\underline{S}}_i$ stands for the response of every one the simpler objects, also known as canonical objects, whereas w_i indicates the weight of $\underline{\underline{S}}_i$ in the combination leading to the measured scattering matrix.

In order to simplify the understanding of (2.26), it is desirable that the matrices $\underline{\underline{S}}_i$ are independent to avoid that a particular scattering behavior to be present in more than one scattering matrix relevant to a canonical object. Often the most restrictive property of orthogonality is imposed.

In real situations, the measured scattering matrix by the radar corresponds to a distributed target. Only in a few occasions, this matrix will correspond to a simpler or canonical object, which a good example is, for instance, the trihedral employed to calibrate SAR imagery. An example of coherent decomposition can be obtained expressing the measured scattering matrix though the Pauli basis set of (2.7), i.e. the Pauli decomposition.

Assuming to be in the backscattering case, the reciprocity applies, and so the Pauli basis reduces to the set $\{\sigma_0, \sigma_1, \sigma_2\}$.

Therefore, the measured scattering matrix can be expressed as follows

$$\underline{\underline{S}} = \begin{bmatrix} S_{hh} & S_{hv} \\ S_{hv} & S_{vv} \end{bmatrix} = s_1^P \frac{\sigma_0}{\sqrt{2}} + s_2^P \frac{\sigma_1}{\sqrt{2}} + s_3^P \frac{\sigma_2}{\sqrt{2}} \quad , \tag{2.27}$$

wherein the weights are defined as the components of the Pauli scattering vector

$$\underline{s}^P = \left(s_1^P, s_2^P, s_3^P \right)^T = \frac{1}{\sqrt{2}} \left(S_{hh} + S_{vv}, S_{hh} - S_{vv}, 2S_{hv} \right)^T \quad . \tag{2.28}$$

The interpretation of the Pauli decomposition is founded on the physical reading associated to each of the matrices $\sigma_0, \sigma_1,$ and σ_2.
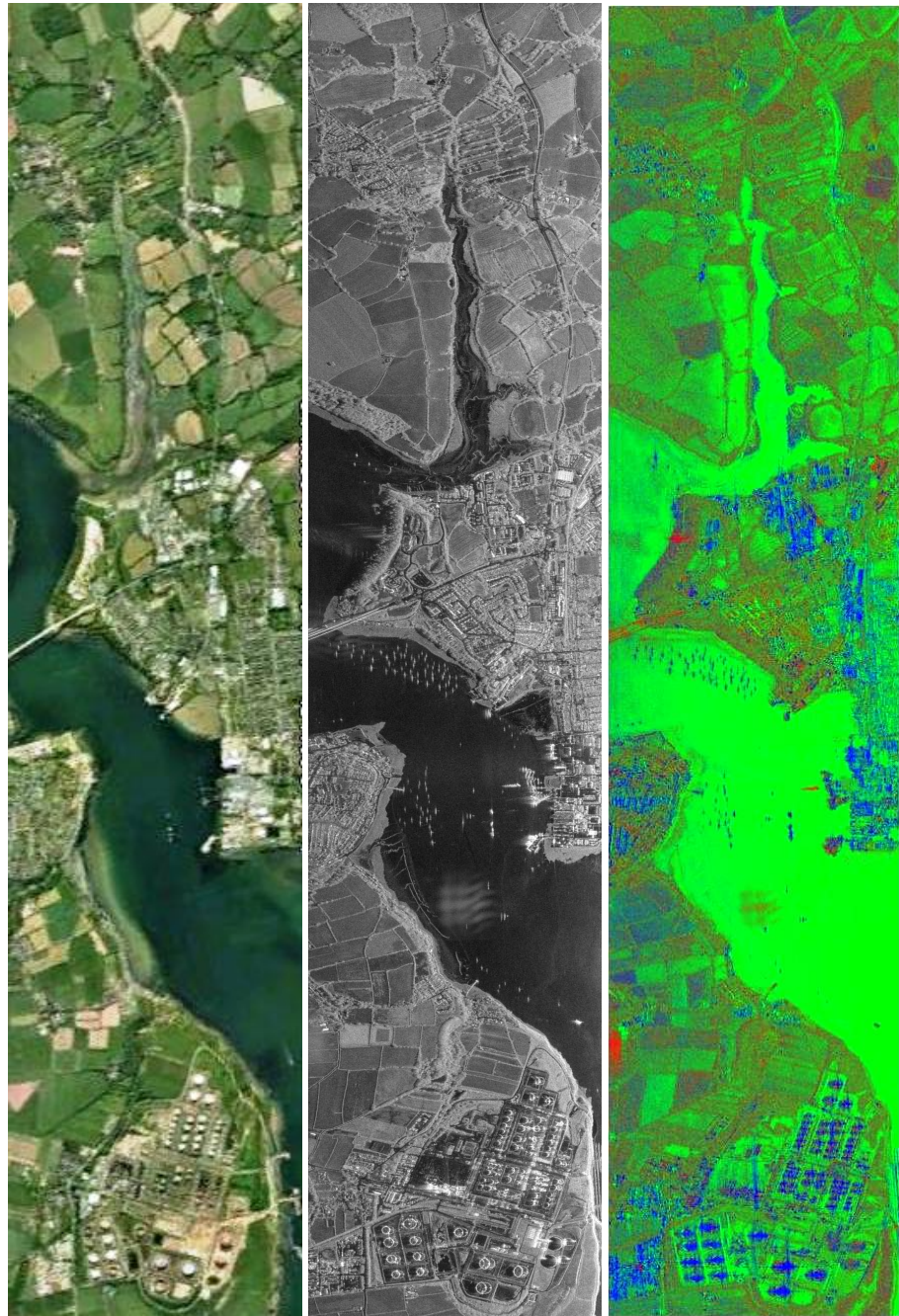
In particular σ_0 is representative of a single- or odd-bounce scattering mechanism (i.e., flat surfaces and thriedrals), and so $\left|s_1^P\right|^2$ is the power provided by this mechanism to the overall scattering process; similarly, σ_1 represents a double- or even-bounce scattering mechanism (i.e., dihedrals), so that $\left|s_2^P\right|^2$ is the power scattered by this type of target; finally, σ_2 corresponds to the scattering of a 45°-oriented diplane. As it can be observed from the expression of σ_2, it is representative of a target which returns a wave whose polarization is orthogonal to that of the incident one (i.e., volume scattering due to the forestry canopy), and so $\left|s_3^P\right|^2$ is the amount of power due to the volume-like component in the considered distributed target.

Moreover, from (2.28) it is easy to show that the SPAN of the measured scattering matrix is

$$\text{SPAN} = \left|s_1^P\right|^2 + \left|s_2^P\right|^2 + \left|s_3^P\right|^2 \quad . \tag{2.29}$$

An example of the information deducible by means of this analysis is shown in Figure 2.8-(c), where the Pauli decomposition is carried out on polarimetric SAR data acquired at S-band (f=3.2 GHz) over the Pembroke Dock area (UK) by the Astrium airborne demonstrator (see Figure 2.8, where both the optical image (a) and the HV channel (b) are depicted).

In particular, the RGB combination of the power pertinent to the three fundamental scattering mechanisms, normalized by the SPAN, i.e. $\left(\left|s_3^P\right|^2 \middle/ \text{SPAN} \to \text{Red}, \; \left|s_1^P\right|^2 \middle/ \text{SPAN} \to \text{Green}, \; \left|s_2^P\right|^2 \middle/ \text{SPAN} \to \text{Blue} \right)$, is shown in Figure 2.8-(c).

Figure 2.8: optical view (a), SAR image (HV channel) (b) and RGB-coded Pauli decomposition (c) for the Pembroke Dock area.

Accordingly, the soft classification performed by the Pauli decomposition is evident. Indeed, even though a greenish overall aspect can be observed, due to the clear prevalence of sea and almost-flat surfaces in the image, all the built-up areas are correctly represented in shades of blue, as the double-bounce is there the dominant scattering mechanism (see, for instance, the boats or the cylindrical tanks), while a reddish color is associated to the vegetated areas (see, for instance, the tree-lined shores at the center of the image), where the canopy scattering contribution rules.

Concerning the incoherent decompositions, as mentioned, they are performed on matrices containing the second order moments of the scattered field, including the coherence matrix or the covariance matrix, and hence they are more suitable (with respect to coherent ones) to extract information from very chaotic targets [8]. Again, the goal of these decompositions is to separate such matrices in order to obtain the combination of second order descriptors corresponding to simpler targets.

To give an idea of this kind of polarimetric analysis, here the Eigenvectors-Eigenvalues based decomposition [10] is considered.

To this aim, notice that the coherency matrix for the backscattered field can be expressed in terms of the Pauli vector

$$\underline{\underline{T}}_S = \left\langle \underline{s}^P \cdot \underline{s}^{P\dagger} \right\rangle \; ; \tag{2.30}$$

the rank of such a dyadic product is usually raised from 1 to 3 (in the most general case) by the average operator, but coherency matrix is always hermitian and nonnegative.

Accordingly, $\underline{\underline{T}}_S$ is always diagonalizable, that is

$$\underline{\underline{T}}_S = \underline{\underline{U}} \cdot \underline{\underline{\Lambda}} \cdot \underline{\underline{U}}^{-1} \; , \tag{2.31}$$

wherein $\underline{\underline{U}}$ is the unitary matrix containing the orthonormal eigenvectors $\underline{u}_1$, $\underline{u}_2$, and $\underline{u}_3$, respectively relevant to the eigenvalues λ_1, λ_2 and λ_3 ($\lambda_1 \geq \lambda_2 \geq \lambda_3 \geq 0$) belonging to the diagonal matrix $\underline{\underline{\Lambda}}$.

As regards the eigenvectors, they have 5 degrees of freedom and so they can be expressed as

$$\underline{u}_i = \left(\cos\alpha_i e^{j\varphi_{1i}}, \cos\beta_i \sin\alpha_i e^{j\varphi_{2i}}, \sin\beta_i \sin\alpha_i e^{j\varphi_{3i}} \right)^T \; ; \qquad (2.32)$$

moreover, due to their orthogonality, the coherency matrix can be expressed as

$$\underline{\underline{T}}_S = \sum_{i=1}^{3} \lambda_i \underline{u}_i \cdot \underline{u}_i^{\dagger} = \sum_{i=1}^{3} \lambda_i \underline{\underline{T}}_i \quad , \qquad (2.33)$$

being $\underline{\underline{T}}_i$ the rank 1 coherency matrix describing the scattering from a single target.

An interpretation of the single scattering mechanisms described by each of the rank 1 matrices in (2.33), can be carried out comparing the general expression of the eigenvectors in (2.32) with the (normalized) Pauli scattering vector defined in (2.28).

Indeed, independently of the phase terms φ_1, φ_2, and φ_3, which account just for the phase relations between the components of $\underline{s}^P$, every single scattering mechanism can be described at the variance of α and β [10]. As a matter of fact, the angle β just represents a physical rotation of the scatterers around the line of sight (LOS) of the sensor, while the angle α represents an internal degree of freedom of the target, i.e. α is associated to the type of scattering mechanism.

Accordingly, assuming $\beta=0°$,

- if $\alpha=0°$ then $\underline{u}_i=(1,0,0)$ represents the scattering vector of an isotropic surface (i.e., HH=VV);
- if $\alpha=45°$ then $\underline{u}_i=1/\sqrt{2}\,(1,1,0)$ and so it corresponds to the scattering vector of an horizontally oriented dipole, i.e. volume scattering;
- if $\alpha=90°$ then $\underline{u}_i=(0,1,0)$ and so it is the scattering vector representative of a dihedral (i.e., HH=−VV).

Generally, independently of β, the range of possible variations in scattering mechanism can be illustrated by the variation of α in the range (0°, 90°), as depicted in Fig. 2.9.

As a consequence, (2.33) represents the incoherent summations of three single scattering mechanisms, whose physical reading depends on the value of the three scattering angles α_i. Each of the single scattering mechanism is weighted by its eigenvalue λ_i , which corresponds to a quote of the total power

$$\text{SPAN} = \lambda_1 + \lambda_2 + \lambda_3 \quad . \tag{2.34}$$

Anyway, in order to have a deeper understanding of the overall scattering process, secondary parameters can be defined as functions of the eigenvectors and the eigenvalues of the coherency matrix.
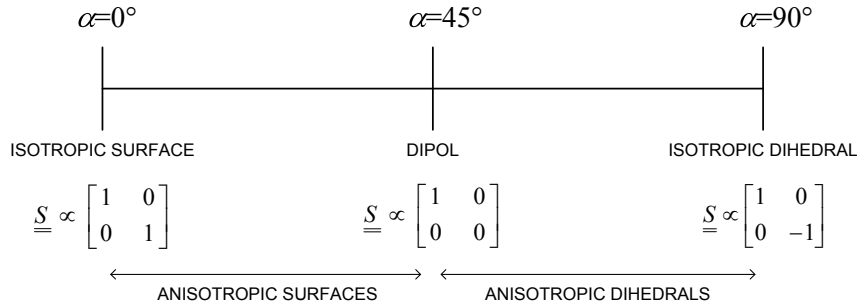

Figure 2.9: schematic representation of α-angle interpretation.

Accordingly, by setting $p_i = \lambda_i / (\lambda_1 + \lambda_2 + \lambda_3)$, the polarimetric entropy H is defined as

$$H = -\sum_{i=1}^{3} p_i \log_3 p_i \tag{2.35}$$

and represents the degree of confusion associated to the scattering process (the larger is the entropy, the greater is the uncertainty associated to the scattering mechanism), while the mean scattering angle is defined as

$$\alpha_M = \sum_{i=1}^{3} p_i \alpha_i \quad , \tag{2.36}$$

which, in agreement with figure 2.9, is representative of the dominant scattering mechanism.

Therefore, a hard classification can be performed using these secondary parameters. In particular, it is possible to identify some meaningful regions on the H/α plane, corresponding to as many scattering mechanisms [11].

Accordingly, depending on both H and α values, the following 9 regions can be considered (see the bottom of Fig. 2.11-(b)):

- Z9={$(H, \alpha) \in$[0,0.5)×[0°,42.5°)}-Low Entropy Surface Scattering: physical surfaces such as water at L and P-Bands, sea-ice at L-Band, as well as very smooth land surfaces, all fall into this category;

- Z8={$(H, \alpha) \in$[0,0.5)×[42.5°,47.5°)}-Low   Entropy   Dipole Scattering: an isolated dipole scatterer would appear here, as would scattering from vegetation with strongly correlated orientation of anisotropic scattering elements;

- Z7={$(H, \alpha) \in$[0,0.5)×[47.5°,90°]}-Low   Entropy   Multiple Scattering: this zone corresponds to low entropy double- or even-bounce scattering events, such as provided by isolated dielectric and metallic dihedral scatterers;

- Z6={$(H, \alpha) \in$[0.5,0.9)×[0°,40°)}-Medium   Entropy   Surface Scattering: this zone describes the increase in entropy due to changes in surface roughness and due to canopy propagation effects;

- Z5={$(H, \alpha) \in$[0.5,0.9)×[40°,50°)}-Medium   Entropy   Canopy Scattering: moderate entropy but with a dominant dipole type scattering mechanism. The increased entropy is due to a central statistical distribution of orientation angle. Such a zone would include scattering from vegetated surfaces with anisotropic scatterers and moderate correlation of scatterer orientations;

- Z4={$(H, \alpha) \in$[0.5,0.9)×[50°,90°]}-Medium   Entropy   Multiple Scattering: this zone accounts for dihedral scattering with moderate entropy. This occurs for example in forestry applications, where double bounce mechanisms occur at lower bands following propagation through a canopy. Canopy tends to increase the entropy of the scattering process. A second important process in this category is urban areas;

- Z3={$(H, \alpha) \in [0.9,1] \times [0°,40°)$}-High Entropy Surface Scattering: this class is not part of the feasible region in space i.e., it is not possible to distinguish surface scattering with entropy .This is a direct consequence of our increasing inability to classify scattering types as entropy increases;
- Z2={$(H, \alpha) \in [0.9,1] \times [40°,55°)$}-High Entropy Vegetation Scattering: scattering from forest canopies lies in this region, as does the scattering from some types of vegetated surfaces with random highly anisotropic scattering elements (no polarization dependence is observed in this class);
- Z1={$(H, \alpha) \in [0.9,1] \times [55°,90°]$}-High Entropy Vegetation Scattering: in this region it is still possible to distinguish double-bounce mechanisms in a high entropy environment. Again such mechanisms can be observed in forestry applications or in scattering from vegetation which has a well developed branch and crown structure.

It is worthwhile highlighting that these regions are not equally populated; as a matter of facts, real targets lie within a theoretical bound (the continuous line at the top of Fig. 2.11(a)) representing the minimum and maximum allowable value of α as a function of the entropy.

As done in the case of the Pauli decomposition, the H/α hard classification has been applied on the polarimetric SAR data relevant to Pembroke Dock.
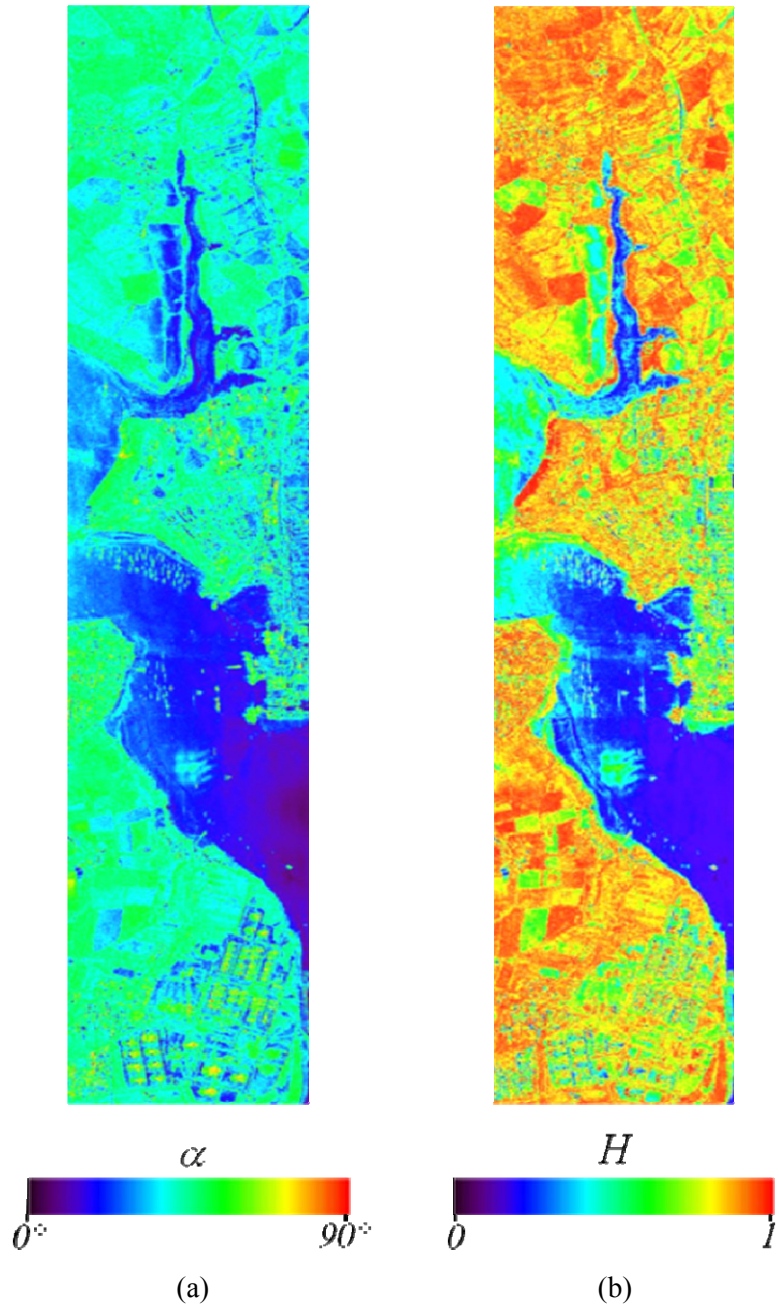
(a)   (b)

Figure 2.10: mean scattering angle (a) and polarimetric entropy (b) for the Pembroke Dock area.

(a)   (b)
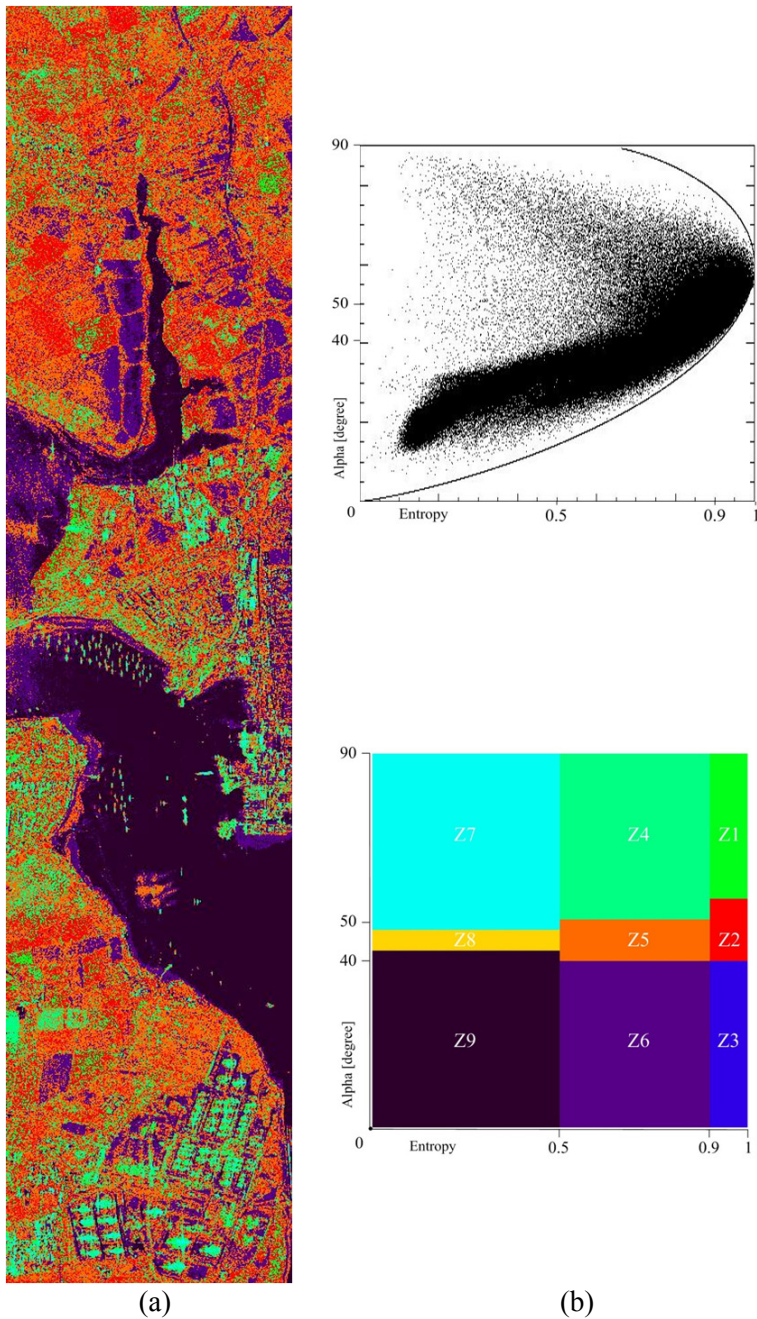
Figure 2.11- (a): *H/α* **classification for the Pembroke Dock area; (b): image pixels distribution (on top) on Z1-Z9 regions (on bottom).**

Hence, in Figure 2.10 the mean scattering angle (a) and the polarimetric entropy for the considered zone (b) are represented, while in Figure 2.11-(a) the H/α hard classification according to the color code represented at bottom of Fig. 2.11-(b) is depicted, together with the image pixel distribution on the H/α plane (at the top of the Fig. 2.11-(b)).

Unlike the soft classification provided by the Pauli decomposition, here only one of the nine colors is associated to every pixel, depending on the specific region on the H/α in which the pixel lies.

In this case, the surface scattering mechanism is dominant just in the sea region of the image, while most of the vegetated fields belong to the medium (Z5) or high entropy canopy (Z2) scattering regions. As for the Pauli decomposition, double-bounce is the dominant scattering mechanism in the urban areas, so that they are correctly detected as points of Z7, Z4 or Z1 regions.

2.2 Classical solutions for the scattering from natural surfaces

This section is intended to recall some well-established solutions for the electromagnetic scattering from natural surfaces.

In particular, here is considered the scattering from natural surfaces modeled through fractal processes.

As a matter of fact, natural surfaces exhibit statistical scale invariance properties that are not met by classical surface models. Of course, a better surface description can be obtained by using models based on fractal concepts [12, 13].Accordingly, a stochastic process $z(x,y)$ describes a fBm (fractional Brownian motion) surface if, for every x, y, x', y', it satisfies the following relation:

$$\Pr\{z(x,y)-z(x',y')<\overline{\zeta}\}=\frac{1}{\sqrt{2\pi}s\tau^{H_t}}\int_{-\infty}^{\overline{\zeta}}\exp\left(-\frac{\zeta^2}{2s^2\tau^{2H_t}}\right)d\zeta \quad , \qquad (2.37)$$

being $\tau=\sqrt{\tau_x^2+\tau_y^2}=\sqrt{(x-x')^2+(y-y')^2}$, H_t the Hurst coefficient, and s the incremental standard deviation, measured in m^{1-H_t} .

It can be demonstrated [12, 13] that a process satisfying (2.37) exists with probability 1 if $0 < H_t < 1$, that it is statistically self-affine, and that an fBm sample surface has a fractal dimension $D=3- H_t$. It must be noted that the fBm process is defined by means of two fractal parameters and is non-stationary [13, 14]; however, according to (2.37), its increments over any fixed horizontal distance τ are stationary isotropic zero mean Gaussian processes, with variance equal to $s^2\tau^{2H_t}$. Furthermore, it can be verified by using (2.37) that the slope of chords joining points on the surface at fixed distance τ is a Gaussian random variable with a root mean square (rms) value equal to s/τ^{1-H_t}.
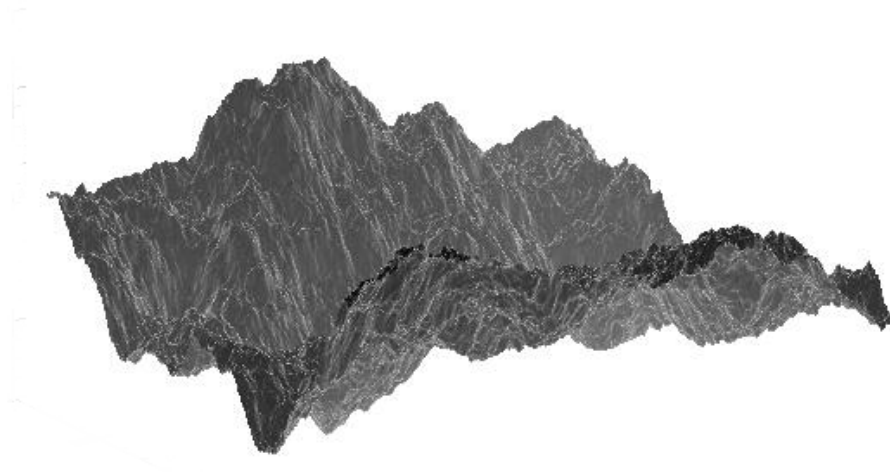
An example of fBm surface is depicted in Figure 2.12.

Figure 2.12: fBm surface (H_t=0.9, s=0.7 m$^{0.1}$).

Direct use of fBm definition makes it possible to obtain closed form expressions of the expected scattered power density computed via both the Kirchhoff Approach (KA) and the Small Perturbation Method (SPM) [14]. Accordingly, main results regarding these two solutions for the scattering from fBm surfaces are recalled, together with a new interpretation of the Kirchhoff scattering integral.

2.2.1 KA solution for the scattered power density

Let us consider a source illuminating a rough surface that separates air (or vacuum) from a homogeneous medium with complex relative permittivity ε_r (see Fig. 2.13). If the source is in far zone with respect to the illuminated surface area, then the incident field is a locally plane wave and, assuming linear polarization, its electric field in a generic point $\underline{r}=(x,y,z(x,y))$ of the scattering surface is

$$\underline{E}^i(\underline{r}) = \hat{p}E_p \exp\{-j\underline{k}_i \cdot \underline{r}\} \quad , \tag{2.38}$$

wherein the unit vector $\hat{p}$ describes the polarization of the field: if $\hat{p}$ is orthogonal to the plane of incidence we have horizontal polarization ($\hat{p}=\hat{h}_i$), whereas the polarization is vertical ($\hat{p}=\hat{v}_i$) if $\hat{p}$ lies in the plane of incidence and is orthogonal to the incident wave propagation vector, $\underline{k}_i=k(\sin\vartheta_i,0,-\cos\vartheta_i)$ where k is the wavenumber. Similar definitions apply for the scattered polarization vector $\hat{q}$ (referred to as $\hat{h}_S$ or $\hat{v}_S$ in the case of horizontal and vertical polarization, respectively), where reference is made to the scattering plane.
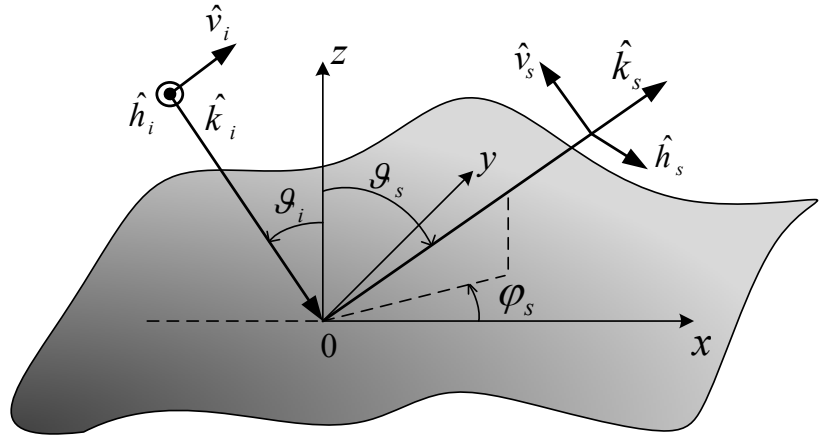

Figure 2.13: scattering rough surface and reference parameters.

By using the Kirchhoff Approach and the small-slope approximation the generic component of the scattered field in the Fraunhofer region is expressed by [3]:

$$\hat{q} \cdot \underline{E}^S(\underline{r}) = E_{pq} = \frac{jkE_p \exp\{-jkR_0\}}{4\pi R_0} f_{pq}(\vartheta_i, \vartheta_S, \varphi_S) \iint_A \exp\{-j\underline{u} \cdot \underline{r}'\} dA \quad , \quad (2.39)$$

where $\underline{k}_S$ is the propagation vector of the scattered wave and $\underline{u} = \underline{k}_i - \underline{k}_S$ i.e.,

$$\begin{cases} u_x = k(\sin\vartheta_i - \sin\vartheta_s \cos\varphi_s) \\ u_y = -k\sin\vartheta_s \sin\varphi_s \\ u_z = -k(\cos\vartheta_i + \cos\vartheta_s) \end{cases} , \qquad (2.40)$$

ϑ_i the incidence angle, and ϑ_s, φ_s the scattering angles (see Fig. 2.13), A is the surface illuminated area and R_0 the distance from its centre to the receiver.

In addition, f_{pq} is a dimensionless function depending on ε_r, incidence and scattering angles, and polarization of incident wave (p) and receiving antenna (q).

Therefore, according to the Physical Optics solution (PO), the mean square value of the generic component of the scattered field can be expressed as

$$< |E_{pq}|^2 > = \frac{k^2 |E_p|^2 |f_{pq}|^2 A}{(4\pi R_0)^2} I \quad , \qquad (2.41)$$

where the term I is the (polarization independent) Kirchhoff scattering integral

$$I = \iint_A \exp\{-ju_x\tau_x - ju_y\tau_y\} \exp\left\{-\frac{1}{2}u_z^2 Q(\tau)\right\} d\tau_x d\tau_y \quad , \qquad (2.42)$$

depending on the fBm structure function $Q(\tau)$, defined as

$$Q(\tau) = < |z(x,y) - z(x',y')|^2 > = s^2 \tau^{2H_t} \quad . \qquad (2.43)$$

The evaluation of the Kirchhoff integral of (2.42) leads to represent the scattered power density by means of the two following series expansions [14-16]

$$
I = 2\pi \begin{cases} 2H_t \sum_{n=1}^{+\infty} \dfrac{(-1)^{n+1} 2^{2nH_t}}{n!} \dfrac{n\Gamma(1+nH_t)}{\Gamma(1-nH_t)} \dfrac{\left(\sqrt{2}|u_z|s/2\right)^{2n}}{\left(u_x^2 + u_y^2\right)^{nH_t+1}}, & H_t \leq \dfrac{1}{2} \\[4mm] \dfrac{1}{2H_t} \sum_{n=0}^{+\infty} \dfrac{(-1)^n}{2^{2n}(n!)^2} \Gamma\left(\dfrac{1+n}{H_t}\right) \dfrac{\left(u_x^2 + u_y^2\right)^{2nH_t+2}}{\left(\sqrt{2}|u_z|s/2\right)^{\frac{2n+2}{H_t}}}, & H_t \geq \dfrac{1}{2} \end{cases} \tag{2.44}
$$

(being $\Gamma(\cdot)$ the Gamma function) which are, to some extent, complementary and whose truncation criteria are detailed in [17]. Concerning the expression of f_{pq}, in the backscattering case (identified by $\varphi_s = \pi$ and $\vartheta_s = \vartheta_i$) its expression simplifies to $f_{pq} = 0$ for $p \neq q$, and $f_{pq} = -2R_p(\overline{\vartheta})/\cos\vartheta_i$ for $p = q$, with R_p being the surface Fresnel reflection coefficient

$$
R_p = \begin{cases} \dfrac{\cos\vartheta - \sqrt{\varepsilon_r - sen^2\vartheta}}{\cos\vartheta + \sqrt{\varepsilon_r - sen^2\vartheta}}, & p = h \\[4mm] \dfrac{\varepsilon_r \cos\vartheta - \sqrt{\varepsilon_r - sen^2\vartheta}}{\varepsilon_r \cos\vartheta + \sqrt{\varepsilon_r - sen^2\vartheta}}, & p = v \end{cases}, \tag{2.45}
$$

evaluated at $\overline{\vartheta} \cong 0$ for small incidence angles and/or large roughness with respect to the wavelength, and at $\overline{\vartheta} \cong \vartheta_i$ for large incidence angles and small roughness with respect to the wavelength [18, 19].

Application of the above formulation to the problem of scattering from natural surfaces is subject to the adequacy of the surface model as well as to the validity of the Kirchhoff and small slope approximations.
Since natural surfaces satisfy (2.37) in a wide, but limited, range of scale lengths (range of fractalness), then the employed surface model applies only on condition that the range of scale lengths involved in the scattering phenomenon is included in the surface range of fractalness.

As a matter of fact, it can be proved that, depending on the scattering direction, a value $\tau*$ exists such that scale lengths much smaller or much larger than $\tau*$ do not appreciably contribute to the scattering process [16].

In the backscattering case such a value is equal to

$$\tau* = \left(\frac{\lambda}{4\pi s \sqrt{H_t} \cos \vartheta_i} \right)^{\frac{1}{H_t}} \tag{2.46}$$

and so at microwave frequencies, most natural surfaces can be modeled as fractals. Concerning the validity limits, KA holds if the surface mean radius of curvature is much greater than the wavelength while the small slope approximations can be used if the rms slope is much smaller than unity.

Both of these conditions are satisfied if it results [16]:

$$s/k \left(10/\tau*\right)^{2-H_t} << 1 \quad . \tag{2.47}$$

2.2.2 Kirchhoff scattering integral as a symmetric alpha-stable distribution

This subsection focuses on the scattering integral analytical expression and on its physical interpretation. First of all, here it is stated that for an fBm surface, the Kirchhoff scattering integral is directly proportional to a symmetric alpha-stable (SαS) distribution. The interpretation of this intriguing result leads to revisit the meaning of the Kirchhoff solution and of the Geometrical Optics (GO) even for a regular (classical, non fractal) rough surface.

Accordingly, concerning the rough scattering surface $z(x,y)$, let us first assume that it is regular (non-fractal), and it is modeled as a statistically isotropic and stationary zero-mean Gaussian stochastic process, with variance σ^2 and normalised autocorrelation function $C(\tau)$; in this case, dz/dx and dz/dy are independent zero-mean Gaussian random variables with variance equal to σ^2 times the absolute value of the second derivative of $C(\tau)$ evaluated at $\tau=0$ (in particular, for a Gaussian autocorrelation function with correlation length L, the slope variance turns out to be equal to $2\sigma^2/L^2$) [20].

Again, the Kirchhoff approximation can be used if the surface average radius of curvature is sufficiently larger than the electromagnetic wavelength λ, i.e., if the surface rms curvature is sufficiently smaller than the electromagnetic wavenumber $k=2\pi/\lambda$. For a Gaussian autocorrelation, this means that

$$\frac{1}{k\sigma}\left(\frac{\sigma}{L}\right)^2 << 1 \quad , \tag{2.48}$$

Also in this case, KA leads to the mean square value of the scattered field whose expression is given by (2.41), however with the difference that the structure function in (2.42) can be now related to the surface autocorrelation function as $Q(\tau)=2\sigma^2\left[1-C(\tau)\right]$.

Therefore, after the substitution $u_z\tau_x=t_x$, $u_z\tau_y=t_y$, in the Kirchhoff integral of (2.42), the equation (2.41) can be expressed as

$$<\left|E_{pq}\right|^2> = \frac{\left|E_p\right|^2\left|f_{pq}\right|^2 A\, p\left(-\frac{u_x}{u_z},-\frac{u_y}{u_z}\right)}{4R_0^2(\cos\vartheta_i+\cos\vartheta_s)^2} \quad , \tag{2.49}$$

with

$$p(a,b)=\frac{1}{4\pi^2}\iint \exp\{jat_x+jbt_y\}\exp\left\{-\frac{1}{2}u_z^2 Q\left(\frac{t}{u_z}\right)\right\}dt_x dt_y \tag{2.50}$$

and $t=\sqrt{t_x^2+t_y^2}$.

It is worth noting that $a=-u_x/u_z$ and $b=-u_y/u_z$ on one hand uniquely identify the scattering direction given the incident one, see (2.40); on the other hand they are equal to the surface slope values such that the local specular direction coincides with the scattering direction [3]. This twofold role of a,b is a key point of the following analysis.

By expanding $Q(\tau)$ in Taylor series around $\tau=0$ and assuming that $C(\tau)$ is a regular and even function, it results

$$\exp\left\{-\frac{1}{2}u_z^2 Q\left(\frac{t}{u_z}\right)\right\} = \exp\left\{-\frac{1}{2}\sigma^2\left|C^{(2)}(0)\right|t^2\right\}G(t_x,t_y) \qquad (2.51)$$

with

$$G(t_x,t_y) = G(t) = \exp\left\{\sum_{n=2}^{\infty}\frac{(-1)^n}{(2n)!}\frac{\sigma^{2n}\left|C^{(2n)}(0)\right|t^{2n}}{(\sigma u_z)^{2n-2}}\right\}, \qquad (2.52)$$

where $C^{(2n)}(0)$ are the derivatives of order $2n$ of $C(\tau)$ at $\tau=0$, so that $\sigma^2\left|C^{(2)}(0)\right|$ is the variance of the derivatives of $z(x,y)$, and the exponential at the right hand side of (2.51) is the joint characteristic function of dz/dx and dz/dy. For a Gaussian autocorrelation function with correlation length L, expression (2.52) takes the following form:

$$G(t) = \exp\left\{\sum_{n=2}^{\infty}\frac{(-1)^n}{n!}\left(\frac{\sigma}{L}\right)^{2n}\frac{t^{2n}}{(\sigma u_z)^{2n-2}}\right\}. \qquad (2.53)$$

The Geometrical Optics (GO) limit is obtained by letting $k\sigma>>1$, so that $\sigma u_z>>1$ and $G(t)$ can be approximated by 1 in the t interval for which the exponential at the right hand side of (2.51) is non-negligible. Accordingly, by substituting (2.51) with $G(t)=1$ in (2.50) we readily get

$$p(a,b) = p_N(a,b) = \frac{1}{2\pi\sigma^2 C^{(2)}(0)}\exp\left\{-\frac{a^2+b^2}{2\sigma^2 C^{(2)}(0)}\right\}, \qquad (2.54)$$

which is the joint probability density function (pdf) of $a=dz/dx$ and $b=dz/dy$: combining (2.49) and (2.54), allows us showing that the GO mean square value of the scattered field is proportional to the surface slope pdf evaluated at $-u_x/u_z, -u_y/u_z$, that, as already mentioned, are the slope values such that the local specular direction coincides with the scattering direction (in the backscattering case, $-u_x/u_z = \tan\vartheta_i, -u_y/u_z = 0$).

This is a well-known result that holds also for non-Gaussian stationary surfaces, provided that their derivatives have finite variance [3].

Let's move finally to assume that the rough scattering surface $z(x,y)$ is modeled by an fBm process.
Before focusing on the Kirchhoff scattering integral, notice that a bivariate centered symmetric (or isotropic) alpha-stable (SαS) random variable A,B, of characteristic exponent α ($\alpha \leq 2$) and dispersion index γ, is generally defined only through its characteristic function $P_\alpha(t_x, t_y)$ [21, 22]

$$P_\alpha(t_x, t_y) = \exp\left\{ -\frac{\gamma\left(t_x^2 + t_y^2\right)^\alpha}{2} \right\} \quad . \tag{2.55}$$

Accordingly, the joint pdf is:

$$p_\alpha(a,b) = \frac{1}{4\pi^2} \iint \exp\{jat_x + jbt_y\} \exp\left\{ -\frac{1}{2}\gamma t^\alpha \right\} dt_x dt_y \quad , \tag{2.56}$$

that usually cannot be computed in a closed form; however, series expansions are available [22], that are of the same form of those obtained in [15, 16].

At this stage, under the Kirchhoff approximation, equation (2.49) holds also for an fBm surface, provided that

$$p(a,b) = \frac{1}{4\pi^2} \iint \exp\{jat_x + jbt_y\} \exp\left\{ -\frac{1}{2}s^2 u_z^{2-2H_t} t^{2H_t} \right\} dt_x dt_y \quad . \tag{2.58}$$

Comparison of (2.58) with (2.57) shows that $p(a,b)$ is a SαS distribution with exponent $\alpha=2H_t$ and dispersion index

$$\gamma = s^2 u_z^{2-2H_t} = s^2 \left(\frac{2\pi(\cos\vartheta_i + \cos\vartheta_s)}{\lambda} \right)^{2-2H_t} \quad . \tag{2.59}$$

This value of the dispersion γ is then proportional to s^2/λ^{2-2H_t}, that is the variance of the slope of chords joining surface points at distance λ, and can be interpreted as the variance of the surface slopes observed at the scale of the electromagnetic wavelength [14]. It is therefore tempting to interpret (2.58) as the fBm counterpart of the GO expression (2.57). However, this is not the correct interpretation, because no GO limit has been used to obtain (2.58), and because fBm surface slopes are not SαS random variables, but they are Gaussian.

The physical interpretation of (2.58) and the meaning of GO limit for fBm surfaces are instead founded on the following discussion.

As known, in computing scattering from rough surfaces, GO can be used if the surface, although macroscopically rough, appears smooth at the electromagnetic wavelength observation scale, so that ray optics can be used, i.e., if the surface can be confused with the local tangent plane over an area of linear size of many wavelengths (significantly larger than the size necessary to use the tangent plane approximation for the computation of surface tangential fields). For a regular randomly rough surface, this means $k\sigma \gg 1$, and can be achieved by either decreasing the wavelength ($\lambda \to 0$), or equivalently by increasing σ while keeping σ/L constant to fulfill condition (2.48). In this case, the overall rough surface can be seen as composed of many smooth surface elements large with respect to the wavelength, for which ray optics can be used, so that their individual scattering pattern is a Dirac delta pulse, i.e., they contribute to the power density scattered along a given direction only if they have a slope such that the scattering direction coincides with the specular one.

That is why the GO mean scattered power density is proportional to the surface slope pdf evaluated at $-u_x/u_z, -u_y/u_z$, as shown by equations (2.49) and (2.54).

As a matter of fact, a similar physical interpretation can be given even if $k\sigma$ is not large. In fact, by recalling a well-known property of the Fourier transform, namely, the convolution theorem, equations (2.50) and (2.51) can be written as the following convolution:

$$p(a,b) = p_N(a,b) \otimes g(a,b) = \iint p_N(a',b')g(a-a',b-b')da'db' \quad , \quad (2.60)$$

where $p_N(a,b)$ is the Gaussian pdf of surface slopes, and $g(a,b)$ is the

(generalized) inverse Fourier transform of $G(t_x,t_y)$.

Note that (2.60) can be read as the statistical mean of $g(a–a',b–b')$ with respect to the surface slopes a',b', and $g(a–a',b–b')$ can be considered as the scattering diagram, evaluated at the scattering direction defined by a,b, of a surface element whose specular direction is defined by (or whose slope is) a',b'.

Accordingly, in some analogy with the usual two-scale models [4, 5], (2.49) and (2.60) can be interpreted as follows: the overall rough surface can be seen as composed of many rough surface elements large with respect to the wavelength, with random Gaussian slopes, and whose scattering pattern is $g(a–a',b–b')$, so that the mean square value of the field scattered by the overall surface is obtained by averaging $g(a–a',b–b')$ over the surface elements' slopes, (2.60). By increasing $k\sigma$ (while keeping σ/L constant) the surface elements become smoother and smoother, g tends to a Dirac delta pulse and (2.60) tends to the GO solution (2.58).

Moreover, notice that, even for $k\sigma$ not large, $p(a,b)$ can be considered a pdf, because it is non-negative and its integral over the entire a,b plane is unitary: hence, it can be interpreted as the pdf of the slopes of an equivalent rough surface whose GO scattered power density is equal to the scattered power density of the actual rough surface.

Let us now move to consider scattering from an fBm surface. First of all, it is worth to note that in this case GO cannot be achieved by decreasing the wavelength ($\lambda{\rightarrow}0$) because, due to the scale-invariance properties of the fBm (i.e., self-affinity), as the observation scale is reduced, finer and finer surface details appear, and the surface never appears smooth at any observation scale; actually, it can be seen that as the observation scale is reduced, the fBm surface appears rougher and rougher [14]. The only way to obtain a smooth fBm surface is to take $D{\rightarrow}2$, i.e., $H_t{\rightarrow}1$. Accordingly, it is appropriate to rewrite (2.58) by expanding t^{2H_t} in Taylor series around $H_t=1$. Series expansion of t^{2H_t} gives

$$t^{2H_t} = t^2 \sum_{n=0}^{\infty} \frac{\left(\ln t^2\right)^n}{n!} \left(H_t - 1\right)^n \quad . \tag{2.61}$$

By using (2.61) the integral in (2.58) becomes

$$p(a,b) = \frac{1}{4\pi^2} \iint \exp\{jat_x + jbt_y\} \exp\left\{-\frac{1}{2}s^2 u_z^{2-2H_t} t^2\right\} G_1(t_x, t_y) dt_x dt_y \quad , \quad (2.62)$$

wherein

$$G_1(t_x, t_y) = G_1(t) = \exp\left\{-\frac{1}{2}s^2 u_z^{2-2H_t} t^2 \sum_{n=1}^{\infty} \frac{(-1)^n}{n!} \left(\ln t^{2-2H_t}\right)^n\right\} \quad . \qquad (2.63)$$

By recalling again the convolution theorem, (2.62) can be rewritten as

$$p(a,b) = p_{N1}(a,b) \otimes g_1(a,b) = \iint p_{N1}(a',b') g_1(a-a', b-b') da' db' \quad , \quad (2.64)$$

where $g_1(a,b)$ is the (generalized) inverse Fourier transform of $G_1(t_x, t_y)$ and

$$p_{N1}(a,b) = \frac{1}{2\pi s^2 u_z^{2-2H_t}} \exp\left\{-\frac{a^2+b^2}{2s^2 u_z^{2-2H_t}}\right\} \qquad (2.65)$$

is, as dictated by the fBm model, the Gaussian pdf of surface slopes observed at the scale of the electromagnetic wavelength.

Equation (2.64) is the fBm counterpart of (2.60) and can be similarly interpreted: the overall rough fBm surface can be seen as composed of many rough surface elements large with respect to the wavelength, whose slopes have a pdf given by (2.65) and whose scattering pattern is $g_1(a-a',b-b')$, so that the mean square value of the field scattered by the overall surface is obtained by averaging $g_1(a-a',b-b')$ over the surface elements' slopes. When H_t tends to 1, the surface elements become smoother and smoother, g_1 tends to a Dirac delta pulse and (2.64) tends to the GO solution. Note that this is just a limit, because an fBm process is not defined for $H_t=1$, but only for $0<H_t<1$. When H_t is smaller than 1, then $p(a,b)$ is a SαS distribution, and it can be interpreted as the pdf of the slopes of an equivalent rough surface whose GO scattered power density is equal to the scattered power density of the actual fBm surface.

2.2.3 SPM solution for the scattered power density

The evaluation of the scattered field from such a rough (fractal) surface can be carried out employing a perturbative approach on condition that the surface variations are much smaller than the incident wavelength and the slopes of the rough surface are relatively small (i.e., the surface is just slightly rough). Making use of the Rayleigh hypothesis and of a surface field series expansion [3], the Small Perturbation Method allows to express the backscattered power density as [16]

$$< \left| E_{pq} \right|^2 > = \frac{\left| E_p \right|^2 4A \left| k^2 \beta_{pq} \cos^2 \vartheta \right|^2}{(2\pi R_0)^2} W(2k \sin \vartheta) \quad , \tag{2.66}$$

wherein $W(\cdot)$ is the (polarization independent) power spectral density of the fBm process equal to [14]

$$W(\kappa) = S_o \kappa^{-\eta} \quad , \tag{2.67}$$

with $\kappa = \sqrt{\kappa_x^2 + \kappa_y^2}$ (being κ_x and κ_y the Fourier mates of x and y), and S_0 and η the spectral parameters, given by:

$$\begin{cases} \eta = 2 + 2H_t = 8 - 2D \\ S_0 = s^2 2^{2H_t} 2\pi H_t \dfrac{\Gamma(1+H_t)}{\Gamma(1-H_t)} \end{cases} \quad . \tag{2.68}$$

As regards the coefficient β_{pq}, in the backscattering direction its expression simplifies to $\beta_{pq}=0$ for $p{\neq}q$, while for $p=q$ it results

$$\beta_{pp} = \begin{cases} \dfrac{\cos\vartheta - \sqrt{\varepsilon_r - sen^2\vartheta}}{\cos\vartheta + \sqrt{\varepsilon_r - sen^2\vartheta}} , & p = h \\[4mm] (\varepsilon_r - 1)\dfrac{sen^2\vartheta - \varepsilon_r(1 + sen^2\vartheta)}{\left(\varepsilon_r \cos\vartheta + \sqrt{\varepsilon_r - sen^2\vartheta}\right)^2} , & p = v \end{cases} \quad . \tag{2.69}$$

It must be underlined that equation (2.66) holds only within the range of fractalness of the surface and only if $s/\lambda{<<}1$.

References

[1] G. Franceschetti, "*Electromagnetics: Theory, Techniques, and Engineering Paradigms*", Plenum Publishing Corporation, New York, 1997.

[2] M. Born, E. Wolf, "*Principles of Optics: Electromagnetic Theory of Propagation, Interference and Diffraction of Light*", Cambridge University Press, Cambridge, 1997.

[3] L. Tsang, J. A. Kong, K. H. Ding, "*Scattering of Electromagnetic Waves: Theories and Applications*", Wiley-Interscience Publication, New York, 2000.

[4] F. T. Ulaby, R. K. Moore, A. K. Fung, "*Microwave Remote Sensing: Active and Passive -Vol. I*", Addison-Wesley, Advanced Book Program, Reading, 1982.

[5] F. T. Ulaby, R. K. Moore, A. K. Fung, "*Microwave Remote Sensing: Active and Passive -Vol. II*", Addison-Wesley, Advanced Book Program, Reading, 1982.

[6] J. S. Lee, E. Pottier, "*Polarimetric Radar Imaging: From Basics to Applications*", CRC Press, Boca Raton (FL), 2009.

[7] S. R. Cloude, "*Polarisation: Applications in Remote Sensing*", Oxford University Press, New York, 2010.

[8] C. Lòpez-Martìnez, L. Ferro-Famil, E. Pottier, Online notes on polarimetry, http://earth.eo.esa.int/polsarpro/tutorial.html.

[9] J. R. Huynen, "*Phenomenological Theory of Radar Targets*", Ph.D. thesis, University of Technology, Delft, 1970.

[10] S. R. Cloude, E Pottier, "A Review of Target Decomposition Theorems in Radar Polarimetry", *IEEE Transactions on Geoscience and Remote Sensing*, vol. 34, no. 2, pp. 498-518, March 1996.

[11] S. R. Cloude, E Pottier, "An Entropy Based Classification Scheme for Land Applications of Polarimetric SAR", *IEEE Transactions on Geoscience and Remote Sensing*, vol. 35, no. 1, pp. 68-78, January 1997.

[12] B. B. Mandelbrot, "*The Fractal Geometry of Nature*", Freeman & C., New York, 1983.

[13] K. Falconer, "*Fractal Geometry*", John Wiley & Sons, Chichester, 1990.

[14] G. Franceschetti, D. Riccio, "*Scattering, Natural Surfaces and Fractals*", Academic Press, Burlington, 2007.

[15] G. Franceschetti, G. Iodice, A. Migliaccio, D. Riccio, "Scattering from natural rough surfaces modelled by fractional Brownian motion two-dimensional processes", *IEEE Transactions on Antennas and Propagation*, vol. 47, no. 9, pp. 1405-1415, September 1997.

[16] G. Franceschetti, A. Iodice, D. Riccio, "Fractal models for scattering from natural surfaces" in *Scattering*, pp. 467-485, Academic Press, London, 2001.

[17] S. Perna, A. Iodice, "On the Use of Series Expansions for Kirchhoff Diffractals", *IEEE Transactions on Antennas and Propagation*, vol.59, no.2, pp. 595-610, February 2011.

[18] A. K. Fung, Z. Li, K. S. Chen, "Backscattering from a randomly rough dielectric surface", *IEEE Transactions on Geoscience and Remote Sensing*, vol. 30, no.2, pp. 356–369, March 1992.

[19] T. D. Wu, K. S. Chen, J. Shi, A. K. Fung, "A Transition Model for the Reflection Coefficient in Surface Scattering", *IEEE Transactions on Geoscience and Remote Sensing*, vol. 39, no. 9, pp. 2040–2050, September 2001.

[20] W. B. Davenport, W. L. Root, "*An Introduction to the Theory of Random Signals and Noise*", IEEE Press, New York, 1987.

[21] G. Samorodnitsky, M. S. Taqqu, "*Stable Non–Gaussian Random Processes*", Chapman & Hall, New York, 1994.

[22] V. V. Uchaikin, V. M. Zolatorev, "*Chance and Stability: Stable Distributions and Their Applications*", VSP, Utrecht, 1999.

Chapter 3

Dielectric Mixing Models

Soil water content and water availability are of great importance on land activities, especially those involving agriculture, forestry, hydrology and engineering. In particular, knowledge of soil water content m_v over extensive areas allows us to determine the repartition of the rainfalls into the surface run-off, seepage and evapotranspiration. Moreover, the information on the space-temporal behavior of the soil moisture represents a key factor in predicting rivers floods, rainfalls and landslides.

Of course, "in situ" measurements of this parameter can be considered ineffective from different points of view, as they do not allow getting information about wide areas or, however, are quite prohibitive if they regard unapproachable spots.

Actually, remote sensing may represent the best candidate to provide this information relevant to every corner of the world and in a comparatively short time, provided that it is able to relate the measured electromagnetic signal to the soil moisture in the observed scene.

As a matter of fact, apart from the wave frequency, the soil dielectric constant is affected by several factors, including moisture content, soil texture, specific surface area and bulk density. The most important influence on the dielectric constant of a soil is certainly its water content, indeed an appreciable rise in the ground relative permittivity is observed considering wet soils instead of dry ones [1].

Accordingly, in this chapter it is reported a short review of some dielectric mixing models, useful to express the soil moisture content in function of the ground permittivity, and vice versa.

3.1   The Wang & Schmugge mixing model

Wang and Schmugge proposed two simple empirical approaches to describe the dependence of the measured soil dielectric constants on the moisture content. In the first approach, the resultant dielectric constant of a soil-water mixture is expressed in terms of the direct mixing of the dielectric constants of the constituents. In the second approach, the complex indices of refraction of the constituents are mixed to give the resultant refractive index of the soil-water mixture [2]; however, only the former is reported here.

The biphase dielectric property for water in soils is assumed in both models, i.e. a transition soil moisture content Wt at which the dielectric constant increases steeply with increasing moisture content is defined. In particular, Wt represents the value of the moisture content below which most of the water molecules are tightly bound to the soil particles; as a consequence, it is difficult to polarize these water molecules and the bulk of water shows a smaller dielectric constant than that for the free water.

The measured data, displayed in Figures 3.1 (a) and (b) and relevant to different soils and measured at both 5 GHz and 1.4 GHz, clearly indicate two distinct regions in the variations of the soil dielectric constant with m_v.

The first region occurs at $m_v <$ Wt, where the real part of the dielectric constant ε, increases slowly with m_v. On the contrary, in the second region at $m_v >$ Wt, ε increases steeply with m_v.

The value of such a transition moisture, has been considered strongly correlated with the wilting point (WP) of the soils, as it results

$$\text{Wt} = 0.49 \times \text{WP} + 0.165 \quad , \tag{3.1}$$

which is itself dependent on the soil texture (see Figure 3.2).

In particular, the expression for WP in terms of the volumetric water content (cm^3/cm^3) is given by:

$$\text{WP} = 0.06774 - 0.00064 \times \text{SAND} + 0.0478 \times \text{CLAY} \quad , \tag{3.2}$$

where CLAY and SAND are the clay and sand contents in percent of dry weight in the analyzed soil.
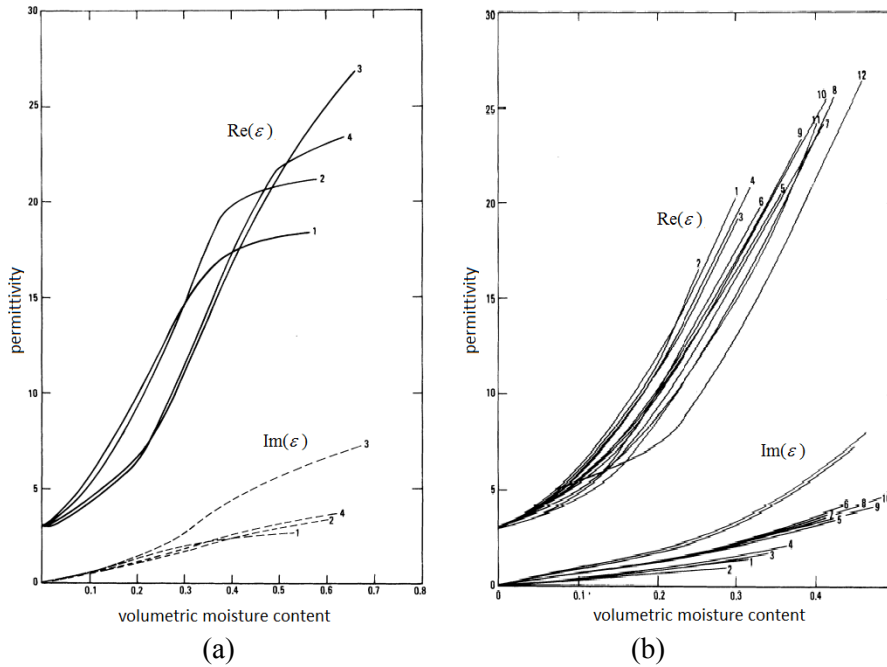
Figure 3.1: dielectric constants versus the water content relevant to different soil textures measured at 5 GHz (a) and 1.4 GHz (b).
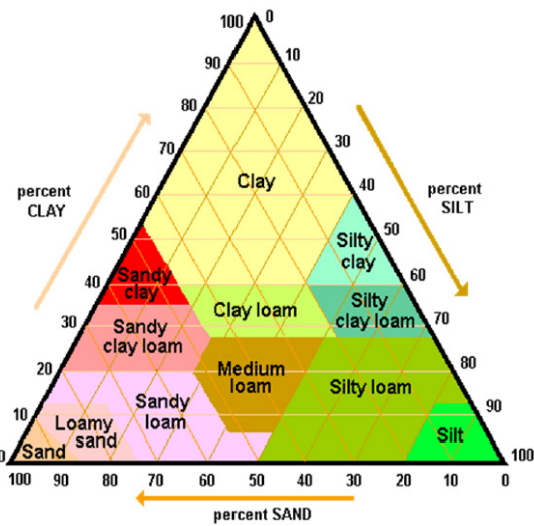

Figure 3.2: percentage of clay, silt and sand for different types of soil.

According to the assumption of such a biphase behaviour, two equations are necessary to define the relationship between the moisture content the complex permittivity within the moisture content range of 0 to 0.5:

$$\varepsilon = \varepsilon_x m_v + (P - m_v)\varepsilon_a + (1 - P)\varepsilon_r \quad , \qquad\qquad \text{for } m_v{\leq}Wt \quad (3.3)$$

$$\text{with } \varepsilon_x = \varepsilon_i + (\varepsilon_w - \varepsilon_i)\frac{m_v}{Wt}\gamma$$

and

$$\varepsilon = \varepsilon_x Wt + (m_v - Wt)\varepsilon_w + (P - m_v)\varepsilon_a + (1 - P)\varepsilon_r ..,.. \qquad \text{for } m_v{>}Wt \quad (3.4)$$

$$\text{with } \varepsilon_x = \varepsilon_i + (\varepsilon_w - \varepsilon_i)\gamma \quad ,$$

wherein P is the porosity of the dry soil, ε_a , ε_w , ε_r and ε_i , in sequential order, are the dielectric constants of air, water, rock, and ice, ε_x stands for the dielectric constant of the initially absorbed water and γ is a parameter which can be chosen to best fit (3.3) and (3.4) to the experimental data.

3.2   The Hallikainen mixing model

The empirical mixing model of Hallikainen et al. [3] was developed exploiting data relevant to five soils with different textural compositions and collected at frequencies equal to 1.4, 4, 6, 8, 10 12, 14, 16 and 18 GHz.
Plots similar to those in Figure 3.1 were generated by smoothing measurements obtained for each soil and frequency combination.
At each frequency, all the curves for both the real and imaginary parts of the ground permittivity exhibit the same general shape but have different curvatures for different soil types. At any given moisture content and at all frequencies, the real part of the permittivity was found to be roughly proportional to sand content (and inversely proportional to clay content); moreover, it was found that this

quantity, apart its magnitude, is soil-texture dependent in the same
fashion at all the employed frequencies.

Concerning the imaginary part of the dielectric constant, its behavior
in function of the soil texture is more complicated, however its value
is always significantly less than its real counterpart, above all at the
lower frequencies.

Moreover, for all soils, measurements indicate that the real
(imaginary) part of the permittivity decreases (increases) with
increasing frequency from 4 to 18 GHz.

Starting from the above mentioned plots, empirical polynomial
expressions were obtained for both the real and imaginary parts of the
ground dielectric constant as a function of the soil moisture content at
each frequency and soil type.

Accordingly, at each frequency, individual polynomial expressions
were generated by combining the expressions relevant to different
soils: they express the (complex) dielectric constant as a function of
the soil moisture content, the sand and clay textural components of a
soil in percent by weight.

(a)   (b)
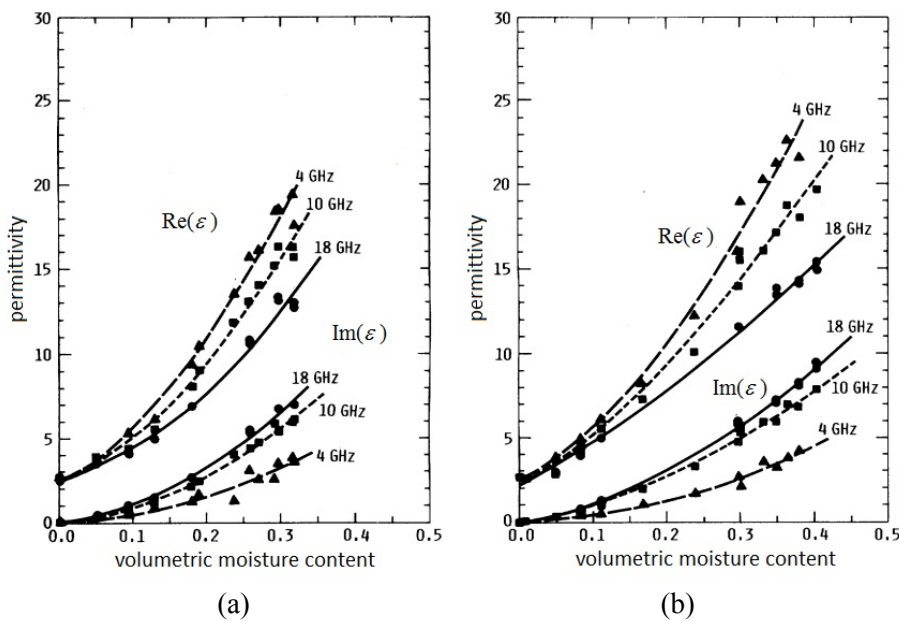
**Figure 3.3: measured dielectric constants (points) at 4, 10, and 18 GHz
for two different fields considered in [3] and polynomial regression fits
(lines).**

The general form of such polynomial is

$$
\begin{aligned}
\varepsilon = \left(a_0 + a_1 \times \text{SAND} + a_2 \times \text{CLAY}\right) \\
+ \left(b_0 + b_1 \times \text{SAND} + b_2 \times \text{CLAY}\right)m_v \quad , \\
+ \left(c_0 + c_1 \times \text{SAND} + c_2 \times \text{CLAY}\right)m_v^2
\end{aligned}
\tag{3.5}
$$

wherein coefficients a_i, b_i and c_i depend on the frequency and their values are listed in [3]. Examples of fit of these polynomials are depicted in Figures 3.3 (a) and (b) together with the relevant measured values, for two soil textures and three different frequencies.

3.3   The Miller & Gaskin mixing model

The above mentioned methods allow us to express the relationship between the ground complex dielectric constant and the soil moisture content provided that the soil texture is known. Of course, most of time this information is not available, if the goal is to obtain the soil moisture from the dielectric constant retrieved through remote sensing techniques. Unlike previous models, the empirical method recalled in this section [4] does not account specifically for the soil properties and instrument frequency. As a matter of fact, the Miller & Gaskin mixing method was developed exploiting measurements obtained by the Theta Probe (TP) and allows us to relate in a very simple manner the water content to the apparent dielectric constant ε^{app} as

$$
m_v = \frac{\sqrt{\varepsilon_{app}} - h_0}{h_1} \quad ,
\tag{3.6}
$$

with h_0 and h_1 generalized calibration constants, whose values are fixed in [4] to $\{h_0, h_1\}=\{1.6, 8.4\}$ for mineral soils and to $\{h_0, h_1\}=\{1.3, 7.7\}$ for organic soils.

As regards the apparent dielectric constant, it represents the output parameter of a Time Domain Reflectometer (TDR) and for low-loss, nearly homogeneous media it is approximately equal to the real part of the ground dielectric constant [5], that is $\varepsilon^{app} \cong \text{Re}\{ \varepsilon \}$.

3.4   Methods performances: a comparison

According to the results discussed in [1], a comparison of the dielectric mixing models is presented in this section.

In particular, on the grounds of measurements exploited in [1], Tables I, II and III contain the volumetric moisture content estimates for the sand, loam and clay soils. Dielectric constants for wet and dry soil were obtained by the GPR (Ground Penetrating Radar), TDR and TP, except in the case of the sand. In despite of its simplicity, as shown in Tables I,II and III, the Miller and Gaskin method (with h_0 and h_1 for mineral soil), provided the best estimate most of times, while the Hallikainen mixing model nearly always provided worst results. In general, all models performed poorly for the loam soil.

Table I

MIXING RESULTS FOR A SAND SOIL

SAND	W. & S.	Hallikainen	M. & G.	Measured m_v (%)
Dry/GPR	7.0	4.6	0.0	7.0
Wet/GPR	27.2	13.7	16.7	21.0
Dry/TDR	14.8	5.0	1.9	7.0
Wet/TDR	31.4	11.3	11.8	21.0

Table II

MIXING RESULTS FOR A LOAM SOIL

LOAM	W. & S.	Hallikainen	M. & G.	Measured m_v (%)
Dry/GPR	11.4	12.0	6.5	2.4
Wet/GPR	16.8	17.1	11.5	24.6
Dry/TDR	11.6	12.0	6.5	2.4
Wet/TDR	19.0	18.6	13.6	24.6
Dry/TP	14.6	14.8	9.1	2.4
Wet/TP	24.5	23.8	19.9	24.6

Table III

MIXING RESULTS FOR A CLAY SOIL

CLAY	W. & S.	Hallikainen	M. & G.	Measured m_v (%)
Dry/GPR	7.0	15.5	1.0	7.0
Wet/GPR	27.2	26.7	15.3	21.0
Dry/TDR	14.8	19.2	5.4	7.0
Wet/TDR	31.4	29.3	19.1	21.0
Dry/TP	19.6	22.2	9.1	7.0
Wet/TP	32.8	30.7	21.0	21.0

References

[1] E. Harmsen, H. Parsiani, M. Torres, "Evaluation of Several Dielectric Mixing Models for Estimating Soil Moisture Content in Land, Loam and Clay Soils," in Proocedings of ASAE American Society of Agricultural and Biological Engineers 2003, Las Vegas 2003.

[2] J. R. Wang, T. J. Schmugge, "An Empirical Model for the Complex Dielectric Permittivity of Soils as a Function of Water Content", *IEEE Transactions on Geoscience and Remote Sensing*, vol. 18, no. 4, pp. 288–295, October 1980.

[3] H. T. Hallikainen, F. T. Ulaby, M. C. Dobson, M. A. El-Rayes, L. K. Wu, "Microwave dielectric behavior of wet soils - Part I: Empirical models and experimental observations", *IEEE Transactions on Geoscience and Remote Sensing*, vol. 23, pp 25-34, January 1985.

[4] J. D. Miller, G. J. Gaskin, "Theta Probe ML2x Principles of Operation and Application", *MLURI Technical Note (2nd edition)*, Delta-T Devices (Cambridge) and MaCaulay Land Use Research Institute (Aberdeen), 1999.

[5] G. C. Topp, "Electromagnetic Determination of Soil Water Content: Measurements in Coaxial Transmission Lines", *Water Resources Research*, vol 16, no. 3, pp. 574-582, June 1980.

Chapter 4

The Polarimetric Two-Scale Model

The classical solutions for the electromagnetic scattering pay their simplicity at the cost of their reliability in describing actual phenomena, and vice versa. In particular, as shown in previous chapter, the Small Perturbation Method (SPM) and the Physical Optics (PO) fail to describe cross-polarization and de-polarization effects usually observed in actual data. Conversely, second-order SPM [1] and other more refined methods (e.g., Integral Equation Method, IEM [2]) account for cross-polarization, but their formulations are not in closed form and are too involved to be usefully employed in surface parameter retrieval algorithms. Accordingly, in this chapter a Polarimetric Two-Scale Model (PTSM) describing the scattering from bare soils and for the surface parameters retrieval from polarimetric SAR data is proposed. In order to account for de-polarization and cross-polarization phenomena, the scattering surface is here considered as composed of rough randomly tilted facets for which, depending on roughness values, the SPM or the PO holds. The facet random tilt causes a random variation of the local incidence angle, and a random rotation of the local incidence plane around the line of sight, which in turn causes a random rotation of the facet scattering matrix. Unlike other similar already existing approaches, this method considers both these effects by relating their analytical formulation to the stochastic description of the scattering surface. Approximated closed-form solutions of the Normalized Radar Cross Sections for the overall scattering surface are attained and compared with real data. The chapter is organized as follows: first section is devoted to describe the considered surface model, while in the second and third sections, NRCS for the single facet and for the whole surface are respectively evaluated. Finally, the direct model validation is provided in the last section.

4.1   Surface model

A bare soil surface is here considered as composed of large-scale variations on which a small-scale roughness is superimposed, so that a two-scale model of the surface is employed. Concerning the large-scale roughness, it is locally treated by replacing the surface with a rough tilted facet, whose slope is the same of the smoothed surface at the center of the pertinent facet, see Figure 4.1. The size of the facets is assumed greater than both the electromagnetic wavelength and the correlation length of the small-scale roughness, but much smaller than both the sensor geometric resolution and the correlation length of the large-scale roughness.
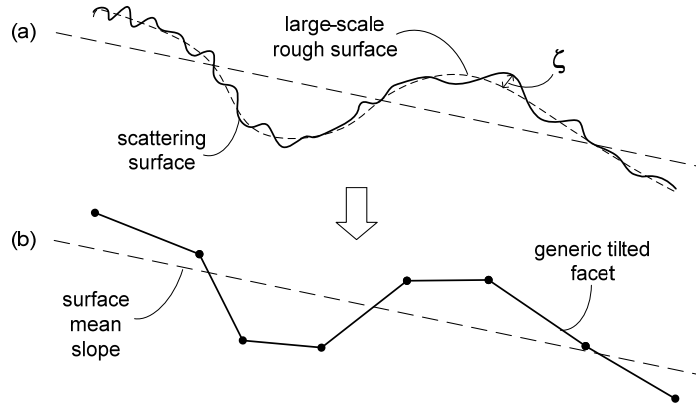
Figure 4.1: from the actual surface (a) to the faceted one (b).

Therefore, using the reference system depicted in Fig. 4.2 (wherein $\hat{n}_l$ is the local unitary normal vector), the randomly rough and randomly tilted facets are defined through the following formula:

$$z(x,y) = \tan\omega(x - x_i) + \tan\gamma(y - y_i) + z_i + \zeta(x,y) \quad , \quad \forall (x,y) \in D_i \quad , \qquad (4.1)$$

where $\tan\omega$ and $\tan\gamma$ are the local azimuth and range slopes, respectively, x_i, y_i, z_i are the coordinates of the i-th facet center, $\zeta(x,y)$ describes the small-scale roughness, and D_i is the i-th facet domain.
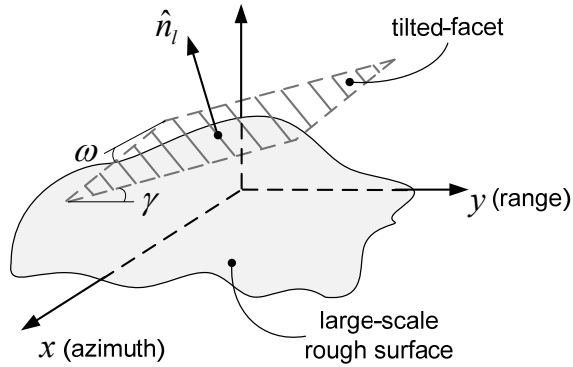
Figure 4.2: 3D sketch of a generic tilted facet.

Both large- and small-scale roughness are modeled as stochastic processes. In particular, the facet slopes along range and azimuth directions, assumed as independent σ^2-variance Gaussian random variables, i.e., $\tan\omega \sim N(\mu_\omega, \sigma^2)$ and $\tan\gamma \sim N(\mu_\gamma, \sigma^2)$.

This assumption only requires that the large-scale roughness is a Gaussian statistically isotropic stationary-increment (i.e., locally homogeneous) process, so that it is compatible with both classical surface models, employing stationary (i.e., homogeneous) processes [1, 3, 4], and fractal surface descriptions, employing the stationary-increment fractional Brownian motion (fBm) processes [5-8].

Moreover, since the mean values μ_ω and μ_γ of the local slopes generally have an arbitrary nonzero value, the considered surface's description may implicitly take into account the topographical features (if any) of the scene to be modeled [9]. Accordingly, as it will be shown in the next chapter, taking into account these mean values in the surface model allows us to improve estimation results in hilly or mountainous areas, if information provided by Digital Elevation Models (DEM) are considered in the retrieval algorithm.

Concerning the small-scale roughness $\zeta(x,y)$, it is modeled as a zero-mean stochastic process whose height standard deviation s is small compared to the electromagnetic wavelength λ. In the following, we assume that $\zeta(x,y)$ is a (band-limited) fractional Brownian motion (fBm) process because it is well recognized by now that fractal models are proper to describe natural surfaces [5-8].

4.2   Single tilted facet return

Let us assume that the sensor illuminates the scene with a (global) incidence angle ϑ, see Fig. 4.3, and let us consider the field scattered by a single tilted rough facet. Due to the facet tilt, the local incidence angle ϑ_l, see Fig. 4.3, is different from the global one, and is related to it and to the facet slopes by [10]:

$$\cos \vartheta_l = \frac{\cos \vartheta + \tan \omega \sin \vartheta}{\sqrt{1 + \tan^2 \omega + \tan^2 \gamma}} \quad . \tag{4.2}$$

In addition, the facet tilt causes a rotation of the local incidence plane around the look direction $\hat{k}$ by an angle β related to the facet slopes and to the global incidence angle by [10]:

$$\tan \beta = \frac{\tan \omega}{- \tan \gamma \cos \vartheta + \sin \vartheta} \quad . \tag{4.3}$$
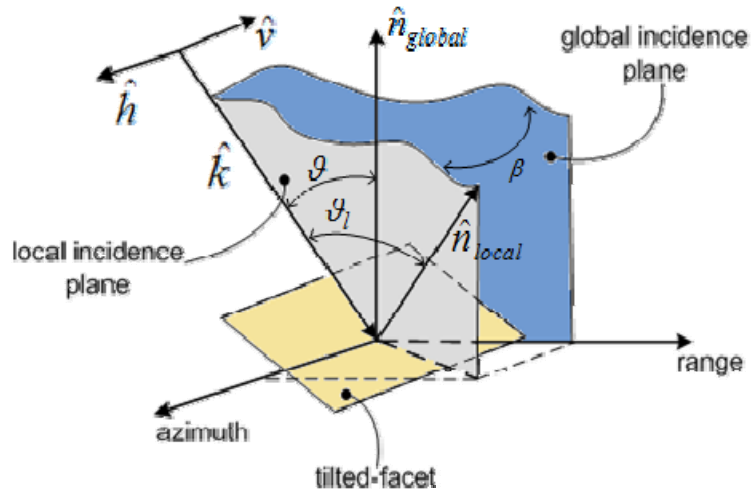
Figure 4.3: rotation of the local incidence plane and local incidence angle drift due to facet tilt.

Therefore, for every tilted facet, the local incidence angle ϑ_l and the rotation angle β of the local incidence plane are random variables, whose stochastic description can be related, from (4.2) and (4.3), to the surface model.

Moreover, since the local incidence angle drift around the radar look-angle is equal to $\Delta\vartheta = \vartheta_l - \vartheta$ then, for small facet's slopes and from (4.2), it results that $\left|\cos\vartheta_l - \cos\vartheta\right| \cong \left|\Delta\vartheta\right|\sin\vartheta \cong \tan\omega\sin\vartheta$, i.e. the standard deviation of such angle drift $\Delta\vartheta$ is approximately σ; likewise, as from (4.3) $\tan\beta \cong \beta \cong \tan\gamma/\sin\vartheta$, so the standard deviation of β is approximately $\sigma/\sin\vartheta$, which is larger than σ. This is in agreement with the intuition that the rotation angle β shows a wider distribution than the incidence angle variation $\Delta\vartheta$ but, of course, this also shows that the latter is not negligible with respect to the former. Such considerations represent the key concepts for the PTSM formulation [11]. Indeed, even though other existing theoretical two-scale methods [12-14] account for both de-polarization and cross-polarization, PTSM is the only one for which these phenomena rise straight from the surface description, considering both the (same order) facet's tilt effects.

As a matter of fact, in the well-established two-scale model presented in [13], there termed as X-Bragg, the rotation angle β is heuristically assumed equal to an uniform random variable, while the local incidence drift is not accounted for at all. Accordingly, the X-Bragg solution represents a particular, simplified case of the Polarimetric Two-Scale Model.

According to notations presented in Chapter 2, the backscattered (incoherent) field E_{pq}^s is given by [3]:

$$E_{pq}^s = \frac{E_p^i k^2 \cos^2\vartheta_l}{\pi r}\chi_{pq}(\vartheta_l,\beta)\,w(\vartheta_l)\exp\{-jkr\}\quad,\tag{4.4}$$

where E_p^i is the incident field, $k=2\pi/\lambda$ is the wavenumber, r is the radar-to-target distance, $w(\vartheta_l)$ is a polarization-independent function depending on microscopic roughness, p and q are the polarizations of the incident and scattered field, respectively, and can each stand for h

(horizontal) or v (vertical) and $\chi_{pq}(\vartheta_l,\beta)$ are the elements of the matrix

$$\underline{\underline{\chi}}(\vartheta_l,\beta)=\underline{\underline{R}}_2(\beta)\cdot\underline{\underline{F}}(\vartheta_l)\cdot\underline{\underline{R}}_2^{-1}(\beta) \quad . \tag{4.5}$$

wherein

$$\underline{\underline{R}}_2(\beta)=\begin{bmatrix} \cos\beta & \sin\beta \\ -\sin\beta & \cos\beta \end{bmatrix} \quad , \tag{4.6}$$

is the unitary rotation matrix, accounting for the rotation of the local polarization reference system with respect to the global one and it is responsible of the cross-polarization effect. This effect is often not included in usual two-scale models [1], but it is considered in [13]. On the other hand, in [13] ϑ_l is approximated by ϑ in equations (4.4, 4.5). As already underlined, here both the incidence plane rotation and the variations of ϑ_l are considered.

As regards $\underline{\underline{F}}$, it is the matrix of the Bragg or PO coefficients (according to the solution adopted for the electromagnetic scattering within a facet) of a single horizontal (i.e., non-tilted) facet

$$\underline{\underline{F}}=\begin{bmatrix} F_h(\vartheta_l) & 0 \\ 0 & F_v(\vartheta_l) \end{bmatrix} \quad , \tag{4.7}$$

whose entries F_h and F_v , have an analytical expression depending on which solution is adopted for the electromagnetic scattering within a facet.

Hence, the facet (incoherent) NRCS is defined as

$$\sigma_{pq}^0 = \frac{4\pi r^2 \left\langle \left| E_{pq}^s \right|^2 \right\rangle_{|\zeta}}{A\left| E_p^i \right|^2} \quad , \tag{4.8}$$

where A is the facet's area and the symbol $\left\langle f \right\rangle_{|\zeta}$ stands for "the mean of f with respect to the random variable ζ". So, using (4.5) in (4.8), it results:

$$\sigma_{pq}^0 = \frac{4}{\pi} k^4 \cos^4 \vartheta_l \left| \chi_{pq} \right|^2 W(\vartheta_l) \quad , \tag{4.9}$$

that is,

$$\begin{cases} \sigma_{hh}^0 = \frac{4}{\pi} k^4 \cos^4 \vartheta_l W(\vartheta_l) \left| F_h(\vartheta_l) \cos^2 \beta + F_v(\vartheta_l) \sin^2 \beta \right|^2 \\ \sigma_{vv}^0 = \frac{4}{\pi} k^4 \cos^4 \vartheta_l W(\vartheta_l) \left| F_v(\vartheta_l) \cos^2 \beta + F_h(\vartheta_l) \sin^2 \beta \right|^2 \\ \sigma_{hv}^0 = \frac{4}{\pi} k^4 \cos^4 \vartheta_l W(\vartheta_l) \left| (F_v(\vartheta_l) - F_h(\vartheta_l)) \sin \beta \cos \beta \right|^2 \end{cases} \tag{4.10}$$

wherein W is related to the mean of the square-modulus of w and its expression again depends on the adopted scattering solution.

As stated, full expression for the NRCS in (4.10) rely on the method chosen to solve the scattering problem from the microscopic roughness, i.e. on the specific expression assumed by F_h, F_v and W.
In particular, if the PTSM is used to describe the polarimetric scattering at lower bands (L, P bands) and the standard deviation s of the microscopic roughness is small with respect to the wavelength λ, then the first-order SPM is suitable to compute the electromagnetic scattering from the small-scale surface variations [9, 11, 15, 16] (SPM based PTSM).
It must be noted that in a very narrow cone around ϑ_l=0 (corresponding to $\tan\omega$=0,$\tan\gamma$=$\tan\vartheta$) whose angular width is of the order of λ/L (with L the facet linear size), the first-order SPM (and then equation 4.10) does not hold and the zero-order (coherent) SPM becomes non-negligible. However, for non-near-vertical incidence and moderate values of σ, we can ignore this effect.
Accordingly, in this case F_h and F_v represent the Bragg coefficients

$$\begin{cases} F_h = \dfrac{\cos \vartheta - \sqrt{\varepsilon_r - \sin^2 \vartheta}}{\cos \vartheta + \sqrt{\varepsilon_r - \sin^2 \vartheta}} \\ F_v = (\varepsilon_r - 1) \dfrac{\sin^2 \vartheta - \varepsilon_r (1 + \sin^2 \vartheta)}{\left(\varepsilon_r \cos \vartheta + \sqrt{\varepsilon_r - \sin^2 \vartheta} \right)^2} \end{cases} \tag{4.11}$$

with ε_r being the soil relative dielectric constant (or relative permittivity), while W is the power spectral density of the fBm process describing the small-scale roughness, whose expressions is

$$W(\vartheta) = \frac{S_0}{(2k \sin \vartheta)^{(2+2H_t)}} \quad , \tag{4.12}$$

where $0 < H_t < 1$ is the Hurst coefficient, related to the roughness fractal dimension D by the relation $D = 3 - H_t$ and S_0 is directly proportional to the microscopic roughness variance s^2 (see Section 2.2).

As a matter of fact, as the work frequency increases, the wavelength of the transmitted pulse cannot be considered larger than the standard deviation of the microscopic roughness and so the SPM is no longer appropriate to solve the scattering problem within the rough facet.
Therefore, if the PTSM is used to describe the scattering from bare soils at higher bands (S, C and X bands) or in an high (microscopic) roughness regime, then the terms F_h, F_v and W occurring in (4.10) can be evaluated according to the PO solution (PO based PTSM) [17].
Accordingly, in this case, F_h and F_v are proportional to the Fresnel reflection coefficients

$$\begin{cases} F_h = -\dfrac{2}{\cos \vartheta} \dfrac{\cos \vartheta - \sqrt{\varepsilon_r - \sin^2 \vartheta}}{\cos \vartheta + \sqrt{\varepsilon_r - \sin^2 \vartheta}} \\[4mm] F_v = -\dfrac{2}{\cos \vartheta} \dfrac{\varepsilon_r \cos \vartheta - \sqrt{\varepsilon_r - \sin^2 \vartheta}}{\varepsilon_r \cos \vartheta + \sqrt{\varepsilon_r - \sin^2 \vartheta}} \end{cases} \quad , \tag{4.13}$$

and W is related to the Kirchhoff scattering integral I by

$$W(\vartheta) = \frac{1}{(4k \cos^2 \vartheta)^2} I(\vartheta) \quad . \tag{4.14}$$

As stated in Section 2.2, the Kirchhoff scattering integral is proportional to the pdf of an isotropic Symmetric-alpha-Stable distribution with characteristic exponent $\alpha = 2H_t$ and, moreover, it can

be represented via two series expansions [7, 8], whose truncation criteria are detailed in [18].

Concerning the validity limits, the PO method holds if the surface mean radius of curvature is much greater than the wavelength while the small slope approximations can be used if the rms slope is much smaller than unity, i.e. (see Section 2.2)

$$ s/k \left(10/\tau * \right)^{2-H_t} << 1 \quad \text{with} \quad \tau* = \left(\frac{\lambda}{4\pi s \sqrt{H_t} \cos \vartheta} \right)^{\frac{1}{H_t}} . $$

4.3   Total scattered power

If the large-scale roughness height variations are larger than the wavelength and the facet size is larger than small-scale roughness correlation length, then the returns from different facets are uncorrelated, and NRCS a of the whole surface can be obtained by averaging those of a single facet over β and ϑ_l , or, equivalently, over $\tan\omega$ and $\tan\gamma$.

So, to average over β and ϑ_l, we should evaluate the joint probability density function (pdf) of these two random variables, starting from the one of $\tan\omega$ and $\tan\gamma$. However, although it is possible, invoking the fundamental random variable transformation theorem, to analytically compute the exact marginal pdf of β , see [19], the joint pdf of β and ϑ_l cannot be analytically evaluated. Therefore, the evaluation of the total scattered density power requires to average over $\tan\omega$ and $\tan\gamma$ which, first of all, implies to express (4.10) in terms of $\tan\omega$ and $\tan\gamma$ by using (4.2) and (4.3). This is quite straightforward, since it is easy to express all terms appearing in (4.10) in terms of $\cos\vartheta_l$ and $\tan\beta$. Accordingly, the expected value of NRCS can be computed as:

$$ \left\langle \sigma_{pq}^0 (\tan\omega, \tan\gamma) \right\rangle \Big|_{\substack{\tan\omega \\ \tan\gamma}} = \int\limits_{-\cot(\vartheta)}^{+\infty} \int\limits_{-\infty}^{+\infty} \sigma_{pq}^0 (\tan\omega, \tan\gamma) p(\tan\omega, \tan\gamma) d\tan\omega d\tan\gamma \quad , \ (4.15) $$

being $p(\tan\omega, \tan\gamma)$ the slopes joint pdf, i.e.:

$$p(\tan\omega,\tan\gamma)=\frac{1}{2\pi\sigma^2}\exp\left\{-\frac{(\tan\omega-\mu_\omega)^2+(\tan\gamma-\mu_\gamma)^2}{2\sigma^2}\right\}\quad.\qquad(4.16)$$

Notice that integration over $\tan\gamma$ is restricted to the range $-\cot\vartheta<\tan\gamma<+\infty$ to exclude values of ϑ_l greater than $\pi/2$, see (4.2), which correspond to shadowed facets (more exactly, these are the "self-shadowed" facets, whereas the facets shadowed by other facets are totally neglected).

However, the probability of self-shadowed facets is

$$\Pr(\tan\gamma<-\cot\vartheta)=\frac{1}{2}\mathrm{Erfc}\left(\frac{\mu_\gamma+\cot\vartheta}{\sqrt{2}\sigma}\right)\quad,\qquad(4.17)$$

being $\mathrm{Erfc}(\cdot)$ the complementary error function, which is smaller and smaller as its argument is greater than zero, thus - assuming μ_γ not too smaller than zero - for non-near-grazing angles and for moderate values of σ. Accordingly, in this case the integrals over $\tan\omega$ and $\tan\gamma$ can both span the entire real axis. Unfortunately, even with the above simplification, the integral in (4.15) cannot be computed in closed form.

However, assuming small values for facet slopes, the Taylor expansion of σ_{pq}^0 around $\tan\omega$=0, $\tan\gamma$=0 can be used.

Accordingly, the Mac Laurin series of $\sigma_{pq}^0(\tan\omega,\tan\gamma)$ is

$$\left\langle\sigma_{pq}^0\right\rangle\Big|_{\substack{\tan\omega\\\tan\gamma}}=\sum_{n=0}^{+\infty}\sum_{k=0}^{n}C_{k,n-k}^{pq}\left\langle(\tan\omega)^k\right\rangle\left\langle(\tan\gamma)^{n-k}\right\rangle\quad,\qquad(4.18)$$

wherein $C_{k,n-k}^{pq}$ are the series expansion coefficients, defined as

$$C_{k,n-k}^{pq}=\frac{1}{n!}\binom{n}{k}\frac{\partial^n\sigma_{pq}^0}{\partial(\tan\omega)^k\partial(\tan\gamma)^{n-k}}\Bigg|_{\tan\omega=\tan\gamma=0}\quad,\qquad(4.19)$$

whose full expression depends on which model has been chosen, between SPM and PO, to evaluate the scattering from the microscopic roughness.

Concerning the statistical averages occurring in the right hand side of (4.18), since both $\tan\omega$ and $\tan\gamma$ are Gaussian random variables, they can be evaluated by using the formula to obtain moments of any order for a Gaussian variable $Z \sim N(\mu, \sigma^2)$, that is:

$$\left\langle Z^m \right\rangle = \left(-j\right)^m \frac{d^m}{dt^m} \Phi_Z\left(t\right)\Big|_{t=0} \quad , \tag{4.20}$$

where $\Phi_Z\left(t\right) = \left\langle \exp\{jtZ\} \right\rangle = \exp\{jt\mu - t^2\sigma^2/2\}$ is the characteristic function of Z.

Hence, considering Taylor expansion terms up to the second order, we attain to the following expression for the NRCS pertinent to the whole surface

$$\left\langle \sigma^0_{pq} \right\rangle\Big|_{\substack{\tan\omega \\ \tan\gamma}} = C^{pq}_{0,0} + C^{pq}_{1,0}\mu_\omega + C^{pq}_{0,1}\mu_\gamma + C^{pq}_{1,1}\mu_\omega\mu_\gamma$$
$$+ C^{pq}_{2,0}\left(\mu_\omega^2 + \sigma^2\right) + C^{pq}_{0,2}\left(\mu_\gamma^2 + \sigma^2\right) \quad , \tag{4.21}$$

which represents the PTSM solution for the NRCS of the whole scattering surface. In particular, if coefficients in (4.19) are evaluated according to the SPM, then (4.21) represents the SPM based PTSM solution; conversely, if the PO is employed to compute the scattering from the small-scale roughness, (4.21) is referred as PO based PTSM solution.

Notice that in flat areas, i.e. in areas with no significant topography, equation (4.21) reduces to

$$\left\langle \sigma^0_{pq} \right\rangle\Big|_{\substack{\tan\omega \\ \tan\gamma}} = C^{pq}_{0,0} + C^{pq}_{2,0}\sigma^2 + C^{pq}_{0,2}\sigma^2 \quad , \tag{4.22}$$

which represents the only feasible solution also in the case of lack of knowledge on the value of the mean slopes (i.e., no DEM is available for the considered scene).

As mentioned, one of the main goals of the PTSM is to account for de-polarization phenomena, even though this information cannot be provided from the NRCS.

Nevertheless, in order to get other information about the scattering process, the Polarimetric Two-Scale Model allows to evaluate other second order statistics of the diffuse field provided that coefficients in (4.19) are appropriately defined [11].

Accordingly, to have a quantitative measure of how the large-scale roughness affects the polarization degree of the scattered field, the co-polarized correlation coefficient can be defined as

$$\rho_{hhvv} = \frac{\left|\left\langle S_{hh} S_{vv}^* \right\rangle\right|}{\sqrt{\left\langle |S_{hh}|^2 \right\rangle \left\langle |S_{vv}|^2 \right\rangle}} \quad , \tag{4.23}$$

wherein S_{pq} are the entries of the scattering matrix

$$\underline{\underline{S}} = \left(\frac{k \cos \vartheta_l}{\sqrt{\pi}} \right)^2 w(\vartheta_l) \underline{\underline{\chi}}(\beta, \vartheta_l) \quad . \tag{4.24}$$

The expression of (4.23) can be computed according to the PTSM formulation just considering the 2nd order Taylor expansion for each term to be averaged.

Hence, assuming $\mu_\omega = \mu_\gamma = 0$, the behavior of the correlation coefficient versus the standard deviation of the macroscopic roughness is depicted in Figures 4.4 – 4.9, for different values of the incidence angles and permittivity.

At this stage, it is worth underlining that the average of products between entries of the rotated matrix of (4.5) computed via PTSM depends on the small-scale roughness parameters s, H_t and S_0; nevertheless, this dependence tends to cancel out in the ratios of such mean values, i.e. the NRCS as well as the correlation coefficient are substantially independent on the microscopic roughness [11].

$\theta=30°$

ρ_{hhvv}
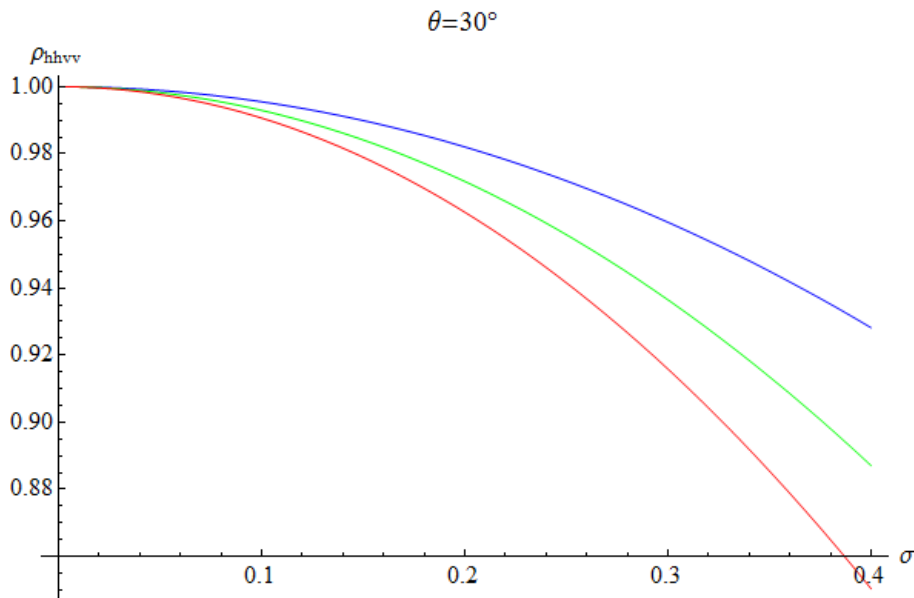
Figure 4.4: SPM based PTSM co-polarized correlation coefficient for $\varepsilon_r=5$ (blue line), $\varepsilon_r=10$ (green line) and $\varepsilon_r=20$ (red line), at $\vartheta=30°$.
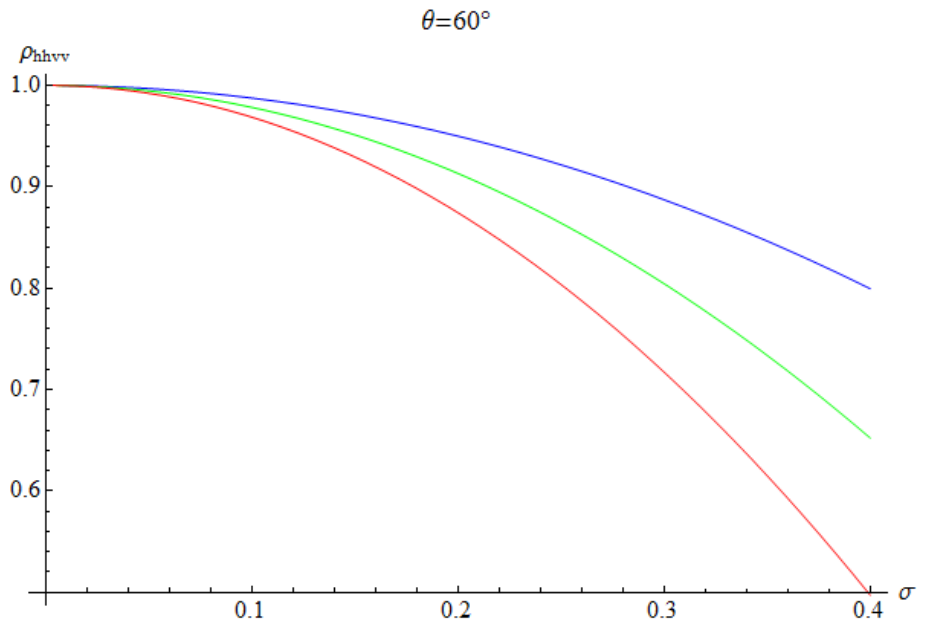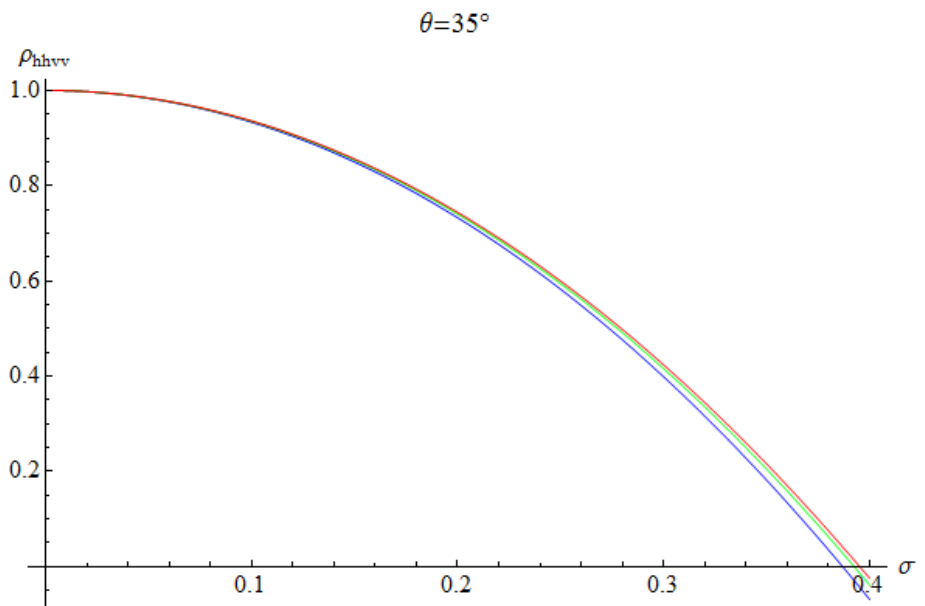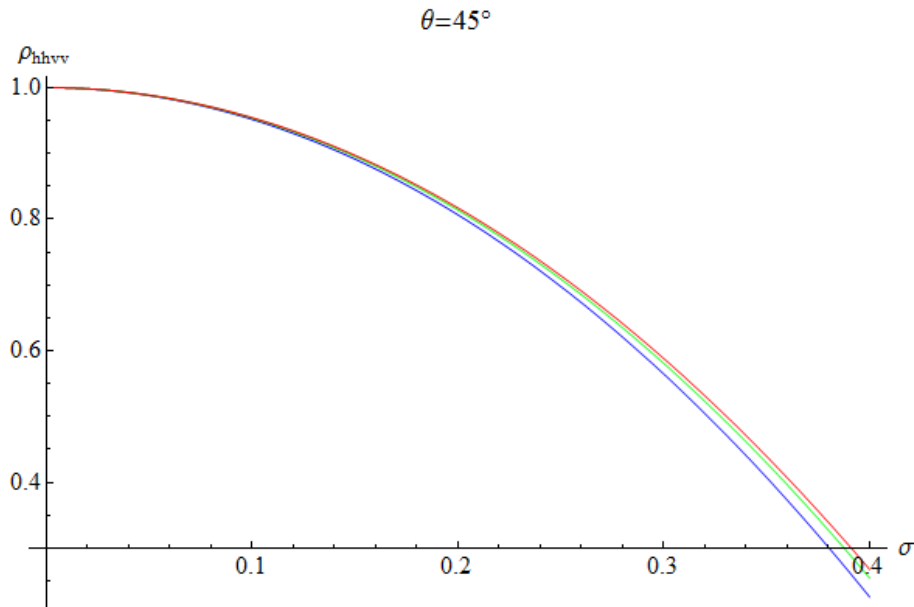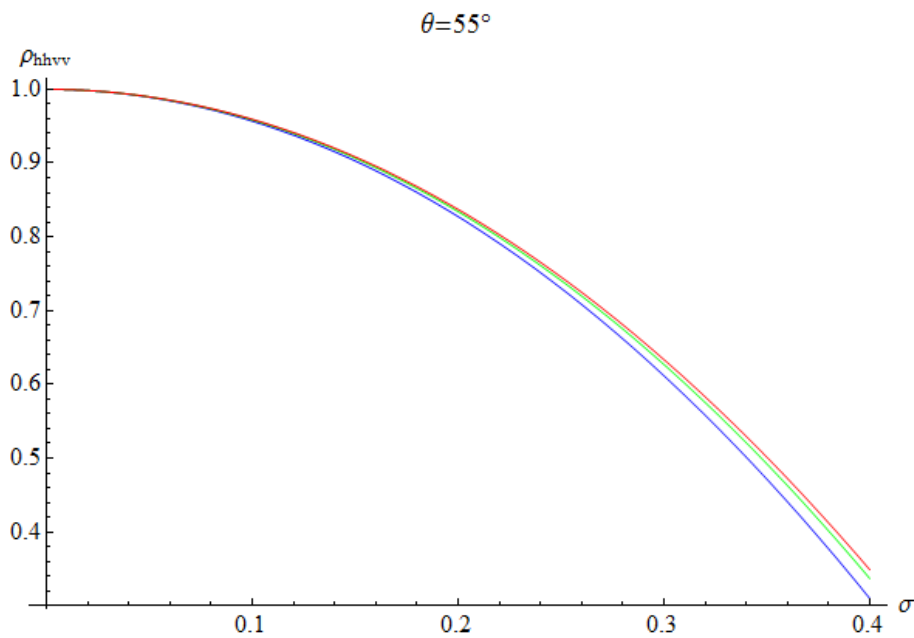
$\theta=45°$

ρ_{hhvv}
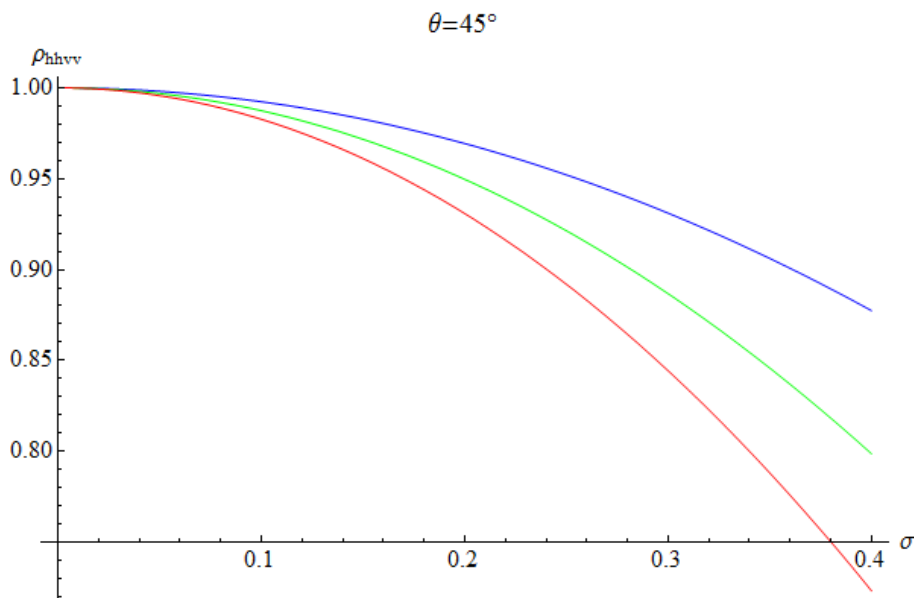
Figure 4.5: SPM based PTSM co-polarized correlation coefficient for $\varepsilon_r=5$ (blue line), $\varepsilon_r=10$ (green line) and $\varepsilon_r=20$ (red line), at $\vartheta=45°$.

$\theta=60°$

ρ_{hhvv}

Figure 4.6: SPM based PTSM co-polarized correlation coefficient for
ε_r**=5 (blue line),** ε_r**=10 (green line) and** ε_r**=20 (red line), at** ϑ**=60°.**

$\theta=35°$

ρ_{hhvv}

Figure 4.7: PO based PTSM co-polarized correlation coefficient for ε_r**=5
(blue line),** ε_r**=10 (green line) and** ε_r**=20 (red line), at** ϑ**=35°.**

$\theta=45°$

Figure 4.8: PO based PTSM co-polarized correlation coefficient for ε_r=5 (blue line), ε_r=10 (green line) and ε_r=20 (red line), at ϑ=45°.

$\theta=55°$

Figure 4.9: PO based PTSM co-polarized correlation coefficient for ε_r=5 (blue line), ε_r=10 (green line) and ε_r=20 (red line), at ϑ=55°.

4.4 Direct model validation

In order to provide a direct validation of the PTSM, a wide variety of scattering data at different frequencies, incidence angles, surface roughness and soil moisture contents, in conjunction with the corresponding ground measurements, should be available over bare or little vegetated soils. To this aim, HH, VV, and HV NRCS data at L band (1.5 GHz) acquired by the University of Michigan's LCX POLARSCAT [20] has been employed, together with "in situ" measurements, for incidence angles varying from 10 to 70 degrees and for four bare soil surfaces with different roughness, each observed in both dry and wet conditions [11]. Concerning the ground truths, only the height standard deviation s over 1m-long profiles and the relative dielectric constant ε_{ref} relevant to the top 4 cm soil layer are reported in [20], while, unfortunately, large-scale roughness σ was not measured. Accordingly, employing these "in situ" measurements (together with the value of σ estimated according to the retrieval procedure explained in next chapter), a comparison between the behavior of the PTSM solution for the NRCS as a function of the incidence angle and the measured backscattering data has been carried out.

In particular, in Figs. 4.10 and 4.11 the comparisons between theoretical trends (continuous lines) and measured values (dots, see Table I and II) of the NRCS, for the wet surfaces termed in [20] as L1 and L2 are shown: a very good agreement between PTSM results and measured backscattering data for all of the three polarization channels can be observed in both cases.

For a more exhaustive analysis on the direct model validation founded on LCX POLARSCAT data, refer to [11].

Table I
MEASURED NRCS [dB] FOR THE L1 WET SURFACE
GROUND TRUTH: ε_{ref}=15.57 , ks=0.13 ; RETRIEVED LARGE-SCALE ROUGHNESS: σ=0.15

ϑ	10°	20°	30°	40°	50°	60°	70°
HH	8	-15	-20	-25	-29	-34	-35
VV	4	-15	-18	-21	-23	-25	-29
HV	-	-38	-39	-40	-43	-44	-48

Table II

MEASURED NRCS [dB] FOR THE L2 WET SURFACE

GROUND TRUTH: ε_{ref}=14.43 , ks=0.10 ; RETRIEVED LARGE-SCALE ROUGHNESS: σ=0.14

ϑ	10°	20°	30°	40°	50°	60°	70°
HH	6	-11	-20	-26	-30	-32	-38
VV	4	-10	-18	-20	-23	-25	-28
HV	-24	-36	-40	-41	-42	-43	-47
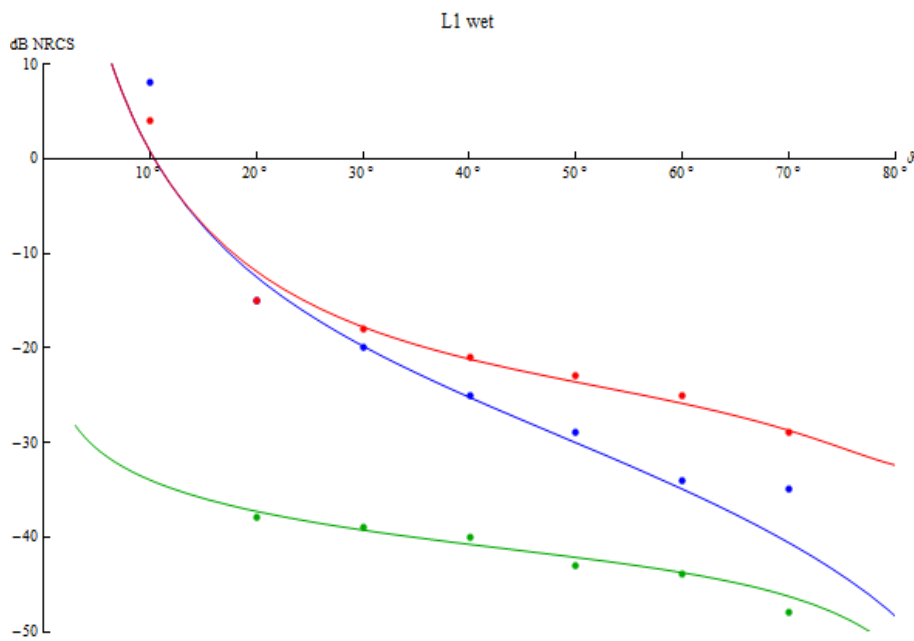
Figure 4.10: Measured (dots) and PTSM (lines) NRCS at VV (red line), HH (blue line) and HV (green line) polarizations for surface L1.
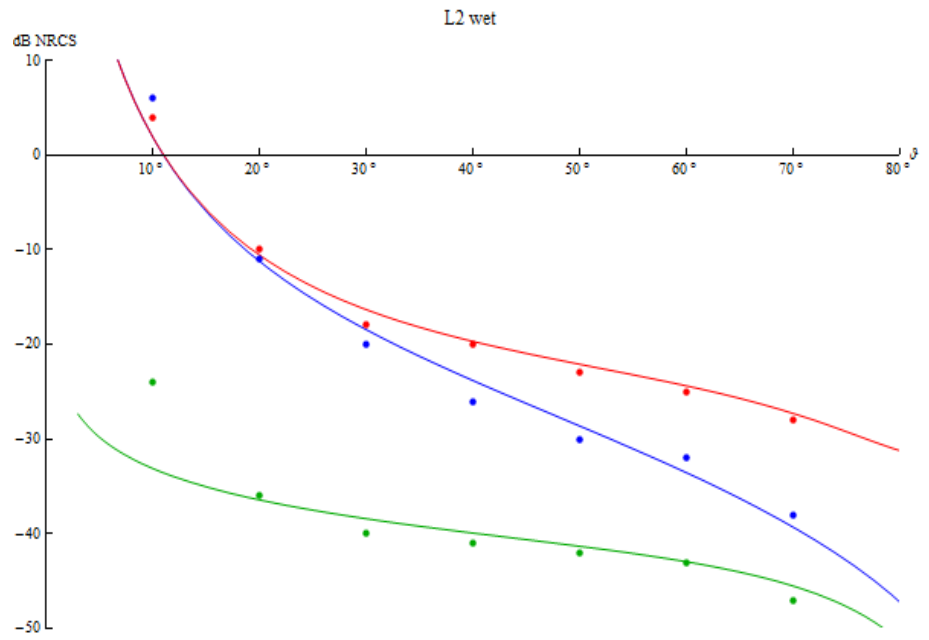
Figure 4.11: Measured (dots) and PTSM (lines) NRCS at VV (red line), HH (blue line) and HV (green line) polarizations for surface L2.

References

[1] F. T. Ulaby, R. K. Moore, A. K. Fung, "*Microwave Remote Sensing: Active and Passive -Vol. I*", Addison-Wesley, Advanced Book Program, Reading, 1982.

[2] A. K. Fung, Z. Li, K. S. Chen, "Backscattering from a randomly rough dielectric surface," *IEEE Transactions on Geoscience and Remote Sensing*, vol. 30, pp. 356–369, March 1992.

[3] L. Tsang, J. A. Kong, K. H. Ding, "*Scattering of Electromagnetic Waves: Theories and Applications*", Wiley-Interscience Publication, New York, 2000.

[4] F. T. Ulaby, R. K. Moore, A. K. Fung, "*Microwave Remote Sensing: Active and Passive -Vol. II*", Addison-Wesley, Advanced Book Program, Reading, 1982.

[5] B. B. Mandelbrot, "*The Fractal Geometry of Nature*", Freeman & C., New York, 1983.

[6] K. Falconer, "*Fractal Geometry*", John Wiley & Sons, Chichester, 1990.

[7] G. Franceschetti, D. Riccio, "*Scattering, Natural Surfaces and Fractals*", Academic Press, Burlington, 2007.

[8] G. Franceschetti, A. Iodice, D. Riccio, "Fractal models for scattering from natural surfaces" in *Scattering*, pp. 467-485, Academic Press, London, 2001.

[9] A. Iodice, A. Natale, D. Riccio, "Retrieval of Soil Surface Parameters via a Polarimetric Two-Scale Model in Hilly or Mountainous Areas", in *Proceedings of SPIE 2011*, Prague, 2011.

[10] J. S. Lee, D. L. Schuler, T. L. Ainsworth, "Polarimetric SAR Data Compensation for Terrain Azimuth Slope Variation", *IEEE Transactions on Geoscience and Remote Sensing*, vol. 38, no. 5, pp. 2153–2163, September 2000.

[11] A. Iodice, A. Natale, D. Riccio, "Retrieval of Soil Surface Parameters via a Polarimetric Two-Scale Model", *IEEE Transactions on Geoscience and Remote Sensing,* vol. 49, no. 7, pp. 2531-2547, July 2011.

[12] Y. Kim, J. van Zyl, J. Shi, "A soil moisture Algorithm Using Tilted-Bragg Approximation", in *Proceedings of IGARSS 2003*, pp.1402-1404, Toulouse 2003.

[13] I. Hajnsek, E. Pottier, S. R. Cloude, "Inversion of surface parameters from polarimetric SAR", *IEEE Transactions on*

Geoscience and Remote Sensing, vol. 41, no. 4, pp. 727–744, April 2003.

[14] M. Martone, T. Jagdhuber, I. Hajnsek, A. Iodice, "Modified Scattering Decomposition for Soil Moisture Estimation from Polarimetric X-Band Data", in *Proceedings of IEEE Gold Conference*, Livorno 2010.

[15] A. Iodice, A. Natale, D. Riccio, "A Polarimetric Two-Scale Model for the Soil Moisture Content Retrieval", in *Proceedings of the International Geoscience and Remote Sensing Symposium IGARSS2010*, Honolulu 2010.

[16] A. Iodice, A. Natale, D. Riccio, "Un modello polarimetrico a due scale per la stima dei parametri superficiali del suolo", in *Proceedings of Riunione Nazionale di Elettromagnetismo RiNEM2010*, Benevento, 2010.

[17] A. Iodice, A. Natale, D.Riccio, "A Physical Optics-based Polarimetric Two-Scale Model", in *Proceedings of URSI Commission F, Microwave Signatures 2010*, Firenze 2010.

[18] S. Perna, A. Iodice, "On the Use of Series Expansions for Kirchhoff Diffractals", *IEEE Transactions on Antennas and Propagation*, vol.59, no.2, pp. 595-610, February 2011.

[19] F. del Monaco, N. De Quattro, A. Iodice, A. Natale, "Extended Small Perturbation Method and Retrieval of Natural Surface Parameters", *Proceedings of the 6th European Radar Conference*, Rome, 2009.

[20] Y. Oh, K. Sarabandi, F. T. Ulaby, "An empirical model and an inversion technique for radar scattering from bare soil surfaces", *IEEE Transactions on Geoscience and Remote Sensing*, vol. 30, pp. 370–381, March 1992

Chapter 5

Retrieval of Surface Parameters via the Polarimetric Two-Scale Model Inversion

The field scattered by a bare soil depends on both surface roughness and soil dielectric constant, and, hence, on the terrain water content. Accordingly, it is possible, at least in principle, to retrieve soil moisture and roughness from appropriate scattering measurements. These retrieval approaches require multiple scattering measurements, supported by the use of scattering models. As for measurements, multi-polarimetric and/or multi-angle Synthetic Aperture Radar (SAR) or scatterometer data can be used; regarding the models, here the focus is on theoretical ones, as they allow to predict the behavior of the scattered field at the variance of the parameters to be estimated. Moreover, the employed model should be as general and accurate as possible, but not so involved to prevent the parameters inversion from the measured data.

To this aim, in the previous chapter, the Polarimetric Two-Scale Model (PTSM) has been presented, in order to account for an accurate and comparatively simple description of the polarimetric scattering process from bare soils. In this chapter a PTSM-based retrieval algorithm is described, using which it is possible to get an unsupervised estimation of the (large-scale, see Chapter 4) roughness and the soil permittivity (or, equivalently, the soil moisture content) from a set of polarimetric SAR or scatterometer data.

Accordingly, the first section of this chapter is devoted to explain how the forecasts on the NRCS provided by the PTSM are exploited to develop the estimation procedure. The retrieval algorithm is then applied on real data acquired at different bands, to provide maps of parameter estimates to and to get an idea of how the frequency affects the retrieving (Section 2).

Moreover, where possible, the retrieval results are compared with "in situ" measurements, in order both to test the performances of the retrieval algorithm and to provide the indirect validation of the PTSM (Section 2).
A comparison with other retrieval methods is also provided.

5.1   Retrieval algorithm

This section is addressed to show the fundamental concepts behind the proposed retrieval algorithm.
The procedure is founded on the forecasts on the power density scattered from bare soils provided by the Polarimetric Two-Scale Model described in the previous chapter.
Recall that the PTSM solution for the Normalized Radar Cross Section (NRCS) of a bare soil is:

$$\left\langle \sigma_{pq}^0 \right\rangle = C_{0,0}^{pq} + C_{1,0}^{pq}\mu_\omega + C_{0,1}^{pq}\mu_\gamma + C_{1,1}^{pq}\mu_\omega\mu_\gamma \\ + C_{2,0}^{pq}\left(\mu_\omega^2 + \sigma^2\right) + C_{0,2}^{pq}\left(\mu_\gamma^2 + \sigma^2\right) \quad , \qquad p,q \in \{h,v\} \quad (5.1)$$

wherein, according to the notation of the Chapter 4, μ_ω and μ_γ are the mean values of the independent stochastic processes describing, respectively, the azimuth and range local slopes, σ is the standard deviation of the large-scale roughness, while $C_{k,n-k}^{pq}$ are coefficients defined in (4.19), whose expressions depend on the radar look-angle, on the polarization, on the soil permittivity and on the solution adopted to evaluate the scattering from the microscopic roughness, whether it be SPM or PO [1-7]. Actually, the small-scale roughness parameters affect the value of each of the NRCS, even though this dependence becomes absolutely negligible in their ratio [2]. Therefore, the co-polar (CP) and cross-polar (XP) ratio, i.e. the ratio of the co-polarized of cross-polarized NRCS, respectively, result to be substantially independent on the microscopic roughness. Accordingly, assuming that the radar look-angle is known, then in principle it possible to get the soil permittivity ε and the large-scale roughness σ from a pair of measured co-polar and cross-polar ratio.

As a matter of fact, the dependence of these ratio on ε and σ is too involved to allow an analytical inversion, i.e. to express ε and σ in function of XP and CP; nevertheless, as CP and XP exhibit monotonic trends versus σ and ε, so it is possible to perform an effective inversion by building up numerical charts where co-polar, cross-polar loci for different values of σ and ε are plotted.

Notice that, the imaginary part of the permittivity is neglected in the retrieval procedure, as it is much smaller than the real part at microwave frequencies (see, e.g., [8]); however, a relationship between the real and imaginary parts of the dielectric constant at the considered frequency is available, [8], so that, if desired, above simplifying assumption can be relaxed (see also [2]).

Examples of such charts are reported in Figure 5.1 and Figure 5.2, where, assuming $\mu_\omega = \mu_\gamma = 0$, co-pol, cross-pol loci parameterized with respect to the electric permittivity ε, ranging from 2 to 22 with a step equal to 2, and to the large-scale roughness parameter σ, ranging from 0 up to 0.4, are shown for the SPM/PTSM and PO/PTSM solutions, respectively. By entering these charts with values of co-pol and cross-pol ratios computed from measured SAR (or, more in general, scattering) data, one can directly read the corresponding retrieved values of ε and σ.

Of course, it is possible to get a similar chart parameterized by the soil moisture content instead of the permittivity, using for instances the mixing model presented in [8-].

Notice that in the SPM based PTSM solution the sigma naught for the HH channel is always lower than that relevant to the VV channel, whereas the opposite happens for PO based PTSM. Therefore, in order to deal always with positive values (in dB), the co-polar ratio is defined as $\left\langle \sigma_{vv}^0 \right\rangle / \left\langle \sigma_{hh}^0 \right\rangle$ in the SPM/PTSM or, conversely, as $\left\langle \sigma_{hh}^0 \right\rangle / \left\langle \sigma_{vv}^0 \right\rangle$ in the PO-PTSM; in both cases the cross-polar ratio is defined as the ratio between $\left\langle \sigma_{hv}^0 \right\rangle$ and $\left\langle \sigma_{vv}^0 \right\rangle$.

It is worth to note that in the charts of Figs. 5.1 and 5.2 rms slope values σ as large as 0.4 are considered. This may seem inappropriate, if one considers that employed second order NRCS expansions hold only for small values of σ. Actually, it has been numerically verified that differences between higher and second order terms of NRCS

remain below 10% only up to values of σ of about 0.2; however, this range of validity extends up to more than 0.4 if we consider co-polarized ratio, and up to about 0.3 for cross-polarized ratio. This means that, fortunately, higher order effects tend to cancel out in the ratio, at least in the range of σ values from about 0.2 to 0.4.

From Figures 5.1 and 5.2 it appears that performances of the retrieval procedure deteriorate as the permittivity and the roughness increase, since higher values of parameters turn out in a reduction of co-pol cross-pol loci dynamic ranges and then in a reduced sensitivity on roughness and permittivity (or, equivalently, in a greater sensitivity to measurement errors).

Moreover, it should be noted that a decrease in the performances is also due to a sensitive reduction of the radar look-angle; indeed, as shown in Figure 5.3, where charts (obtained with $\mu_\omega{=}\mu_\gamma{=}0$, $\varepsilon \in \{2,20\}$ and $\sigma \in \{0,0.4\}$) for $\vartheta{=}20°$, $\vartheta{=}40°$ and $\vartheta{=}60°$ are depicted, the smaller is the angle the narrower becomes the chart, with a consequent decreasing in the reliability of the retrieval result.
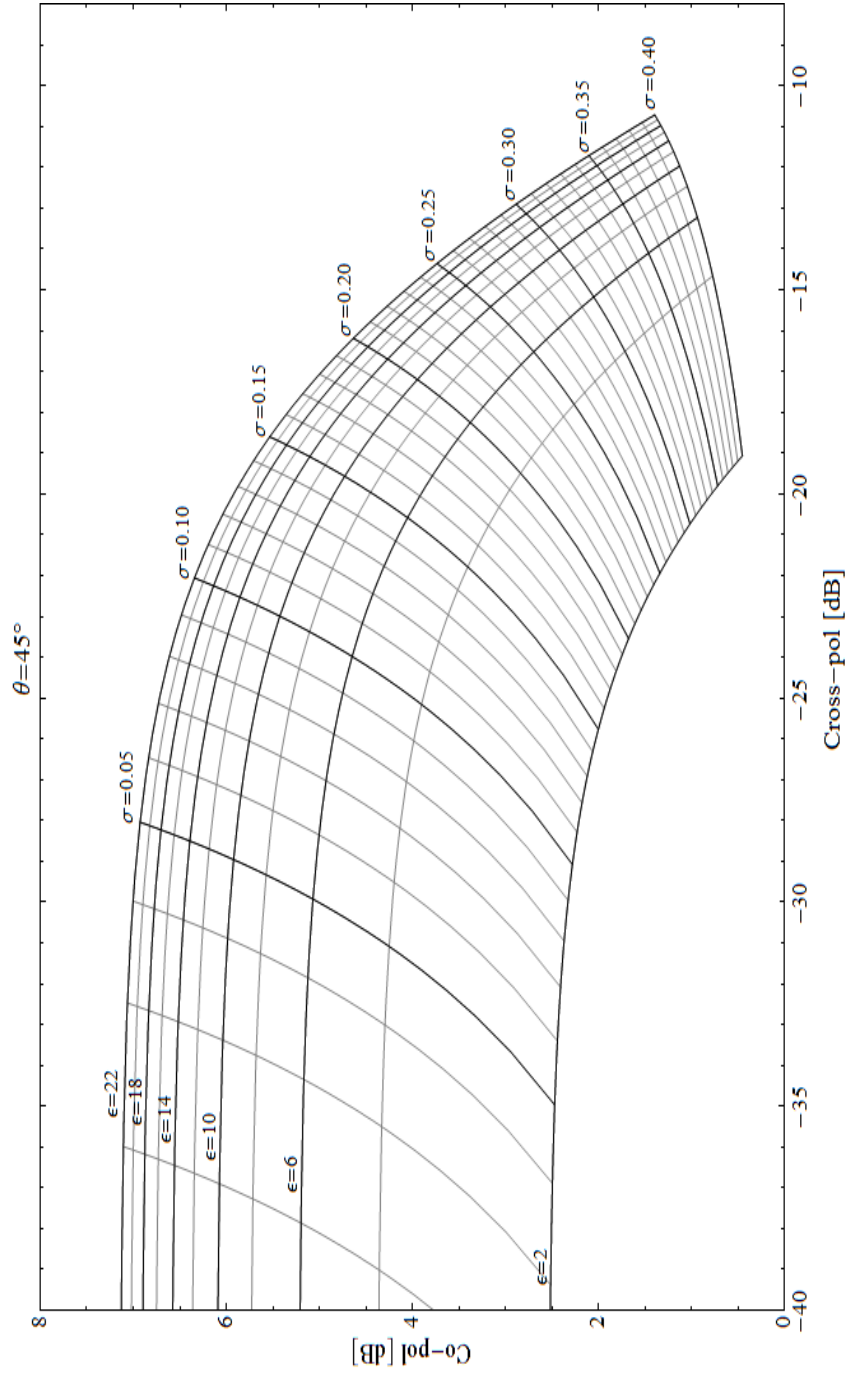
Figure 5.1: SPM based PTSM co-pol cross-pol chart for ϑ=45°.
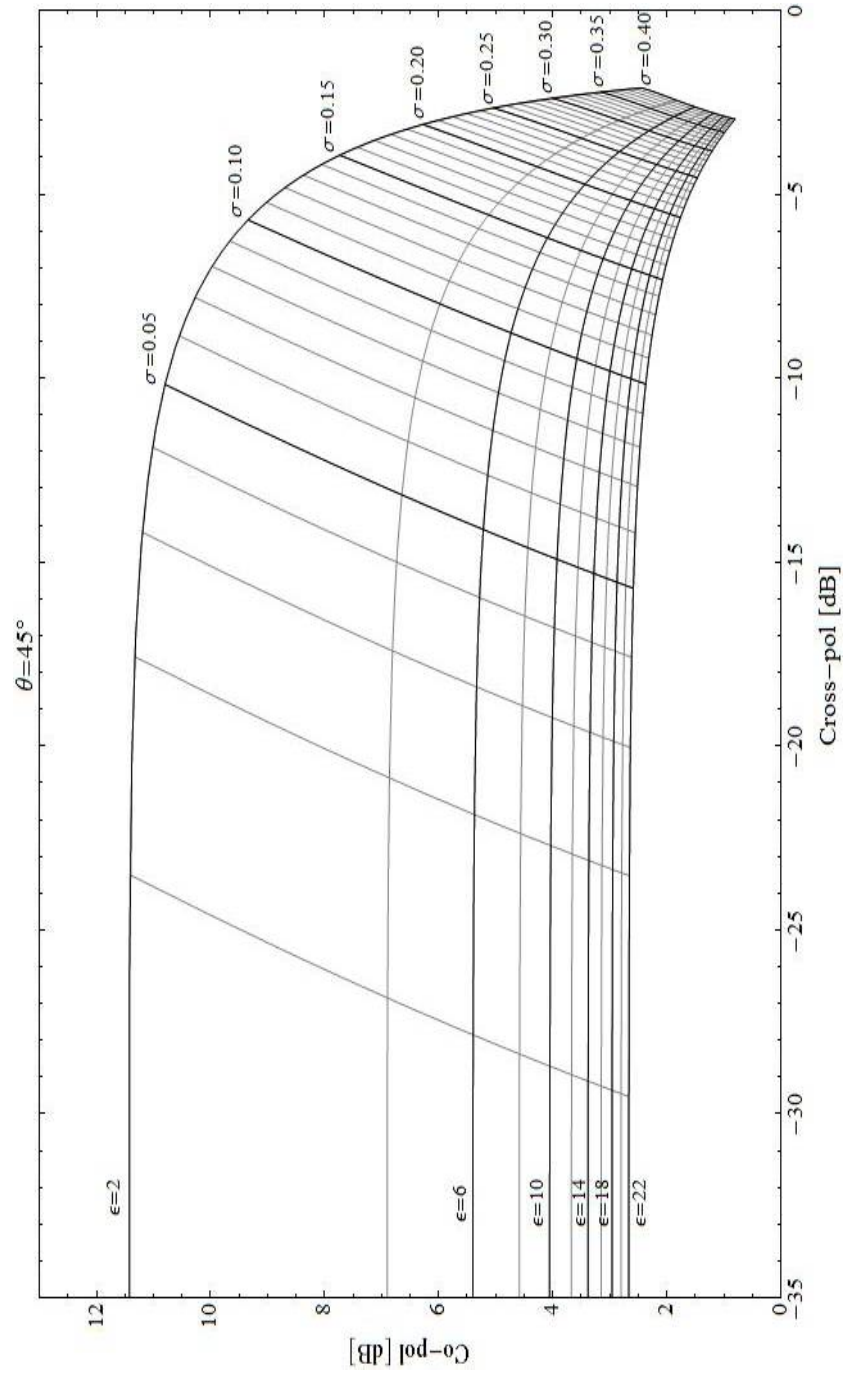
Figure 5.1: PO based PTSM co-pol cross-pol chart for ϑ=45°.
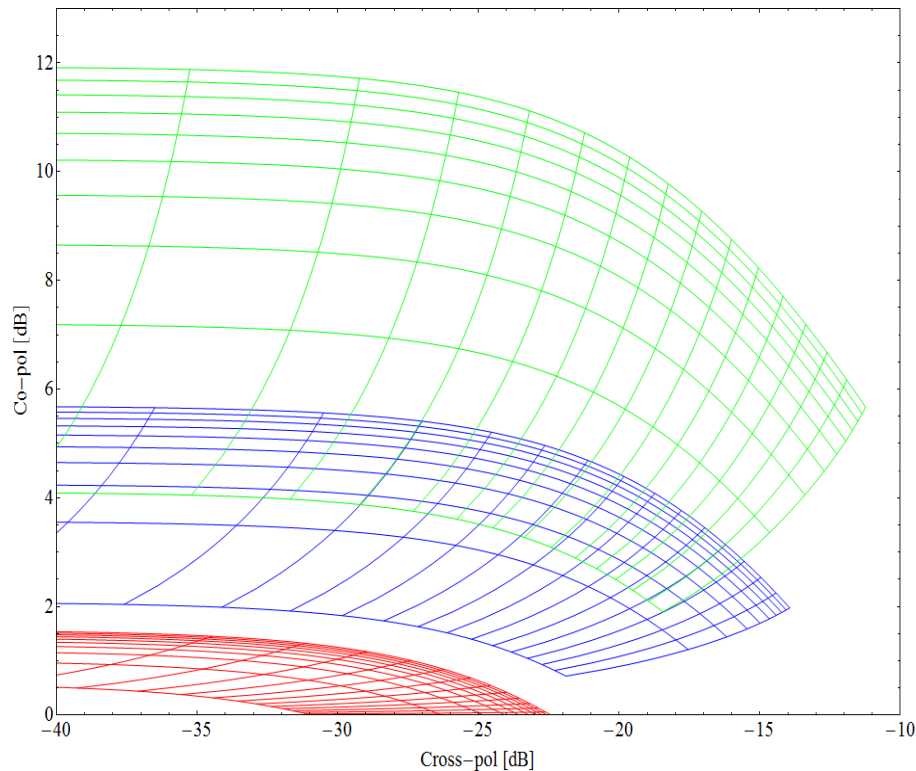
Figure 5.3: SPM based PTSM co-pol cross-pol charts for ϑ=20° (red), ϑ=40° (blue) and ϑ=60° (green).

Of course, this approach can be performed in an unsupervised way, simply making use of special purpose look-up software.

Accordingly, a software has been developed to create soil moisture maps, roughness maps and permittivity maps of sensed scenes just comparing processed input SAR data with correspondence tables built up like above mentioned charts.

Accordingly, as shown in the flow chart of Figure 5.4, the algorithm builds up the co-pol, cross-pol multilooked images from the polarimetric SAR data relevant to the observed scene. At the same time, once set reasonable ranges of values for the permittivity (or the soil moisture content) and the large-scale roughness, these values are used to get tables of theoretical co-polar and cross-polar ratio based on NRCS of equation (5.1).

In the most general case, these tables are computed for every pixel,

because the radar look-angle can span in a wide angular range within the considered image (consider, for instance, airborne SAR images), hence affecting the shape of the co-pol cross-pol chart.

Moreover, if the sensed scene exhibits a significant topography and the relevant Digital Elevation Model (DEM) is available, then it is possible to get the local azimuth (μ_ω) and range (μ_γ) slopes matrices and use these values to evaluate chart according to the pertinent mean slope. Anyway, this step (depicted as the gray rectangle in the flow chart of Figure 5.4) is subject to the availability of a-priori information about the observed area, and so it should not necessarily be carried out. Notice that the tables are built-up according to the SPM based PTSM solution or to the PO based PTSM solution, depending on the sign of every pixel of the co-pol image (in dB).

Additionally, the value assumed by every pixel of co-pol and cross-pol images is checked in order to reject values not compatible with the theoretical model; then, for every pixel with an allowable value, the software looks within the table for the pair of theoretical PTSM-based ratio closest to the pair of measured ones.

Finally, estimation results are obtained just considering the values of ε and σ that correspond to such a theoretical pair.

It is also important to note that this retrieval procedure implicitly provides a reduction of the speckle. Indeed, because of the significant correlation between the noise realizations which affect different polarimetric channels [12], the speckle tends to cancel out in the images of the ratios. Nevertheless, a further speckle reduction is performed using spatial multilook techniques on each of the NRCS images.

As a matter of fact, unlike other estimate procedures (see, for instance [13]), the above algorithm is able to create retrieval maps just from the magnitude of the different polarimetric channels; this could be a fundamental requirement to obtain the parameters estimation even if fully (i.e., both the amplitude and the phase) polarimetric measurements are not available. Indeed, although fully polarimetric SAR sensors are available today (e.g., PALSAR, E-SAR, TERRASAR-X), and accurate calibration is today state-of-the-art, there are still important SAR systems (e.g., ENVISAT, COSMO-SkyMed) that only implement selectable dual-pol.
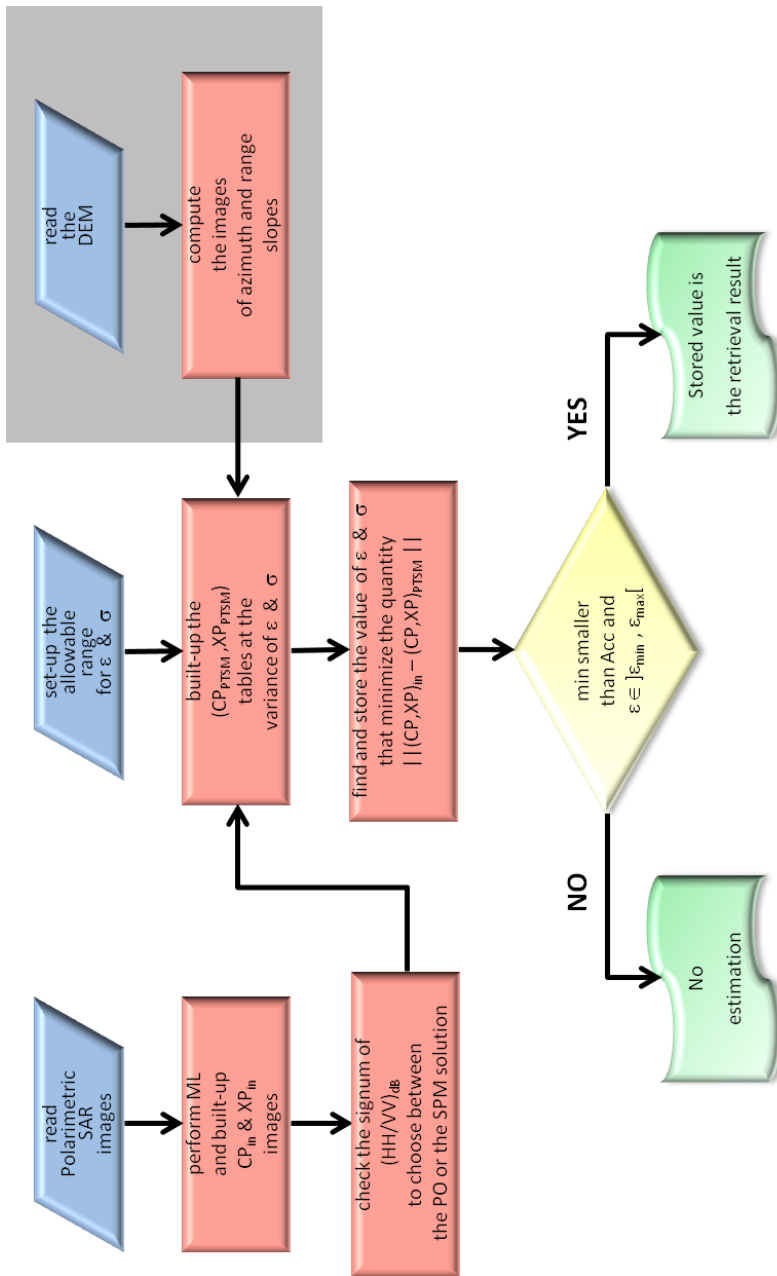
Figure 5.4: retrieval algorithm flow chart.

5.2   Numerical results

The algorithm presented in the previous section is here applied to a large quantity of SAR data acquired at different bands.
Accordingly, in the following, retrieval results relevant to various areas observed at different work frequencies and with different look-angles are provided, in order to get an idea of the algorithm performances at the variance of the scene's characteristics and the sensor parameters.
Moreover, estimate results obtained with the PTSM based retrieval algorithm are compared with in "situ" measurements, if any, to provide an indirect model validation, and with other retrieval methods.

5.2.1   Retrieval results at L band: lack of topography

Here retrieval results relevant to L band and obtained ignoring the effects of the topography (i.e., assuming $\mu_\omega=\mu_\gamma=0$) in the estimate procedure are presented. In particular, NRCS acquired by both by the University of Michigan's LCX POLARSCAT and the NASA AIRSAR are employed; since ground truths are available in correspondence of both of these radar measurements, then an indirect model validation can is carried out exploiting these data.
Concerning the former, HH, VV, and HV NRCS data at L, C, and X band acquired by the University of Michigan's LCX POLARSCAT are available, together with "in situ" measurements, for incidence angles varying from 10 to 70 degrees and for four bare soil surfaces with different roughness, each observed in both dry and wet conditions. Such scattering and "in situ" data were reported and used for instance in [14].
Here L-band (1.5 GHz) POLARSCAT data relevant to the slightly rough bare soil surfaces 1 and 2 of [14] are employed.
Let us first analyze surface 1 in the "wet" and "dry" cases.
Corresponding "in situ" measured parameters are reported in the first row of Tables I and II, where s is the height standard deviation measured over 1m-long profiles [14] and ε_{ref} is the measured relative dielectric constant in the top 4 cm soil layer [14]. Unfortunately, large-scale roughness was not measured in [14], so that only the ε retrieval can be verified, and no direct validation of the σ retrieval is

possible. Tables I and II collect the retrieval results obtained via both the theoretical method presented in [13], there referred as X-Bragg, and the PTSM by considering co-pol and cross-pol ratio at incidence angles from 20 to 60 degrees (the smallest and the highest incidence angles are discarded because, as explained in the previous chapter, the model is not appropriate in correspondence of both small incidence angles and grazing angles) [2].

In these tables, a dash indicates that the considered co-pol cross-pol values do not correspond to any physically acceptable value of ε, so that the inversion algorithm automatically assumes that the model does not hold in these cases.

Table I
RETRIEVAL RESULTS FOR SURFACE 1-WET AT L-BAND
A DASH "-" IS SHOWN FOR RETRIEVED ε VALUES > 20 OR < 2

| surface 1-wet   L-band (1.5 GHz) $ks = 0.13$ ε_{ref}=15.57 | | | | | | |
ϑ	cross-pol [dB]	co-pol [dB]	ε (X-Bragg)	ε (PTSM)	σ (X-Bragg)	σ (PTSM)
20^0	-23	0	_	14	_	0.27
30^0	-21	2	7.8	16.5	0.19	0.16
40^0	-19	4	8.5	16.5	0.18	0.16
50^0	-20	6	6.5	9.5	0.15	0.14
60^0	-19	9	8.0	12.8	0.15	0.14

Table II
RETRIEVAL RESULTS FOR SURFACE 1-DRY AT L-BAND
A DASH "-" IS SHOWN FOR RETRIEVED ε VALUES > 20 OR < 2

| surface 1-dry   L-band (1.5 GHz) $ks = 0.13$ ε_{ref}=7.99 | | | | | | |
ϑ	cross-pol [dB]	co-pol [dB]	ε (X-Bragg)	ε (PTSM)	σ (X-Bragg)	σ (PTSM)
20^0	-23	2	_	_	_	_
30^0	-19	1	7.0	10.5	0.31	0.24
40^0	-19	3	4.75	7.8	0.22	0.19
50^0	-20	4	3.75	4.75	0.20	0.17
60^0	-18	6	3.75	5.75	0.21	0.18

By comparing the retrieved permittivity values reported in the fourth (for X-Bragg) and fifth (for PTSM) columns of Tables I and II with the measured values reported in the first row, it is clear that the PTSM ε retrieval results are in better agreement with ground measurements than the X-Bragg ones in all of the considered cases, except that at 30 degrees for the "dry" surface.

In general, a significant underestimation of ε is obtained by the X-Bragg method, whereas a reasonable or good agreement with measured ε is obtained by the PTSM. Fluctuations of ε estimates are probably due to measurement uncertainty (POLARSCAT measurement precision is ±0.4 dB [14]).With regard to the σ estimates, by comparing the sixth and seventh columns of Tables I and II (however, similar results are obtained also for surface 2) it is clear that they are smaller for the PTSM, and this seems more reasonable for the considered surface (which is rather smooth according to [14]). We note that there is a slight difference between the σ values obtained for the wet and dry cases, and this indicates that the model is still not fully appropriate (in fact, roughness should be the same in both cases). However, this difference is smaller for the PTSM than for the X-Bragg. A completely analogous discussion can be conducted regarding the estimation results (shown, among others, in Figures 5.5 and 5.6 for PTSM and X-Bragg, respectively) relative to the surface 2.

As regards the L-band AIRSAR data (1.5 GHz), the polarimetric set acquired in several different days over the Little Washita basin, during a measurement campaign, in June 1992 is here considered [15].

In particular, for each of the measurement day, the permittivity, soil moisture and roughness retrieval maps has been obtained (Figures 5.9–5.15), exploiting the relevant (only magnitude-) polarimetric sets freely available online (see, for instance, the 10/06/92-image pixel distribution on the CP/XP dB-plane depicted in Figure 5.7). The original images cover an area of about 20km x 20km, and were acquired at a radar look-angle ranging from 20° (the bottom of the image in Figure 5.8) to 60° (the top of the image in Figure 5.8), with a pixel spacing in range and azimuth coordinates of 12m x 12m. The bare soil field labeled in [15] as AG002 has been selected (see the yellow rectangle in Figure 5.8), for which the volumetric soil moisture content was monitored "in situ", and the average NRCS evaluation for

the different polarimetric channels over three 30x30 pixels windows within the considered field has been computed. The retrieved values of the relative dielectric constant are converted into volumetric moisture values m_v by using the Hallikainen mixing model of [8], with percentages of sand and clay equal to 45.5 and 13.4, respectively [15]. The retrieved results for PTSM, and those provided by X-Bragg and by the Oh [14] and Shi [16] empirical methods, are reported in Table III, together with in situ measured values.

As shown, the estimates provided by PTSM are always in better agreement with measured values than X-Bragg and Shi methods, but they are sometimes worse than Oh retrieval results. However, every method provides a decreasing behavior of the retrieved soil moisture content, according to the rainfall trend registered in the measurement days [15]. In order to obtain an overall view of the retrieval methods performances, above described results (together with retrieval results relevant to surfaces 1 and 2 observed at L band of [14]) are collected in Figures 5.5 and 5.6 for PTSM and X-Bragg, respectively. The root mean square (rms) value of differences between retrieved and "in situ" measured ε values is 6.01 for the X-Bragg method and 3.24 for the PTSM method. In addition, the correlation coefficient r between retrieved and "in situ" measured ε values is 0.655 for the X-Bragg method and 0.740 for the PTSM method. These quantitative results confirm that PTSM ε estimates are in better agreement with ground measurements than its "theoretical counterpart".

Table III
SOIL MOISTURE RETRIEVAL RESULTS FOR AIRSAR DATA

Day	PTSM	X-Bragg	Oh	Shi	In Situ
10/06/92	0.247±0.091	0.146±0.054	0.301±0.104	0.161±0.048	0.287
13/06/92	0.217±0.080	0.135±0.070	0.294±0.100	0.131±0.032	0.214
14/06/92	0.127±0.063	0.076±0.055	0.186±0.083	0.105±0.025	0.181
16/06/92	0.110±0.079	0.082±0.055	0.153±0.084	0.087±0.012	0.173
18/06/92	0.107±0.092	0.101±0.068	0.130±0.092	0.078±0.018	0.114
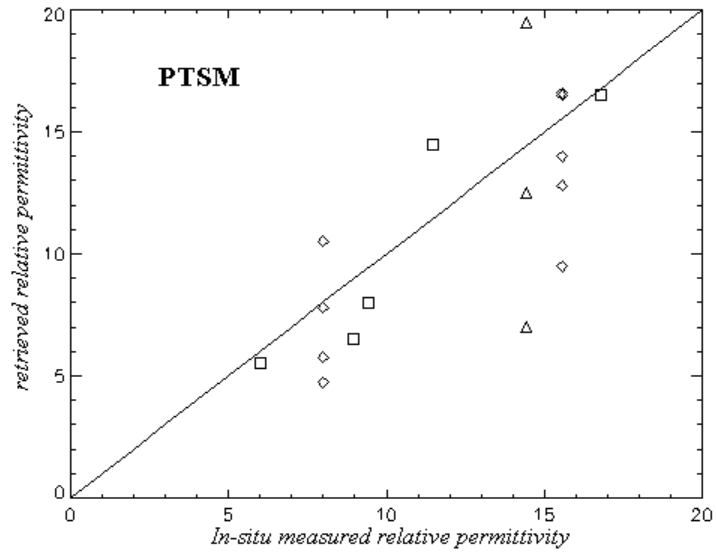
Figure 5.5: PTSM L-band retrieval results for surface 1 (diamonds) and surface 2 (triangles) of [14], and for the Little Washita Basin (squares) [15].The rms error is 3.24 and correlation coefficient *r* is 0.740.
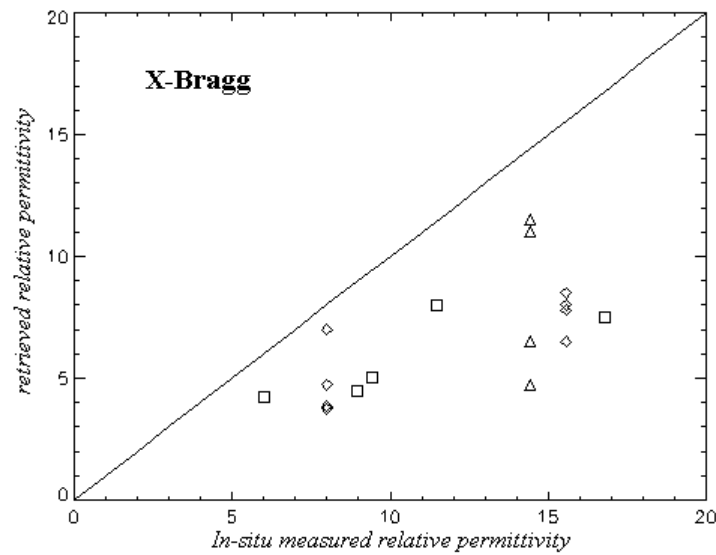
Figure 5.6: X-Bragg L-band retrieval results for surface 1 (diamonds) and surface 2 (triangles) of [14], and for the Little Washita Basin (squares) [15]. The rms error is 6.01 and correlation coefficient *r* is 0.655.
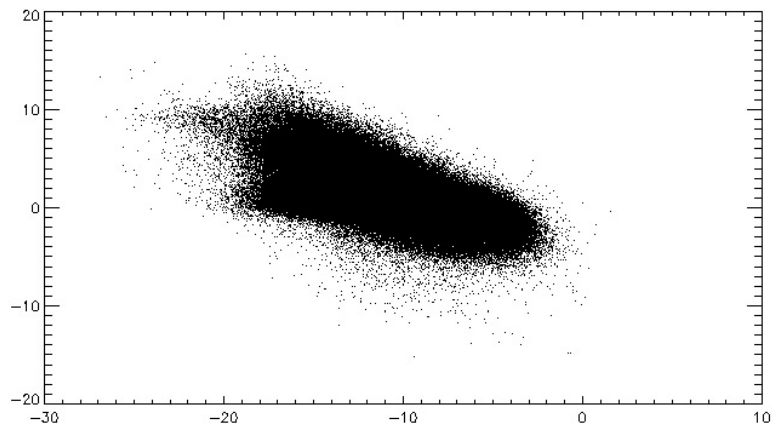
Figure 5.7: pixel distribution on the CP/XP dB-plane for the AIRSAR dataset acquired on 10/6/92 over the Little Washita basin.
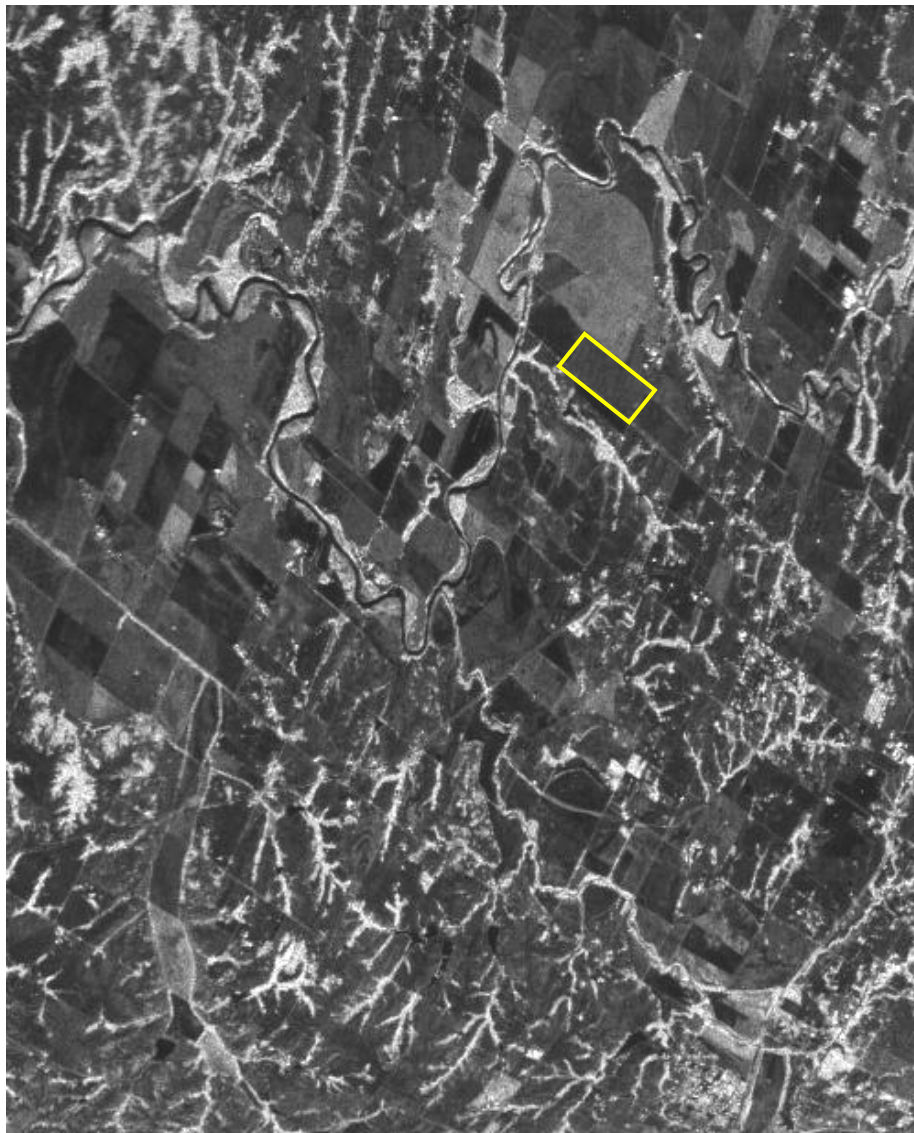
Figure 5.8: L band, σ_{vv} AIRSAR image acquired on 10/6/92 over the Little Washita basin. The yellow rectangle indicates the AG002 site.
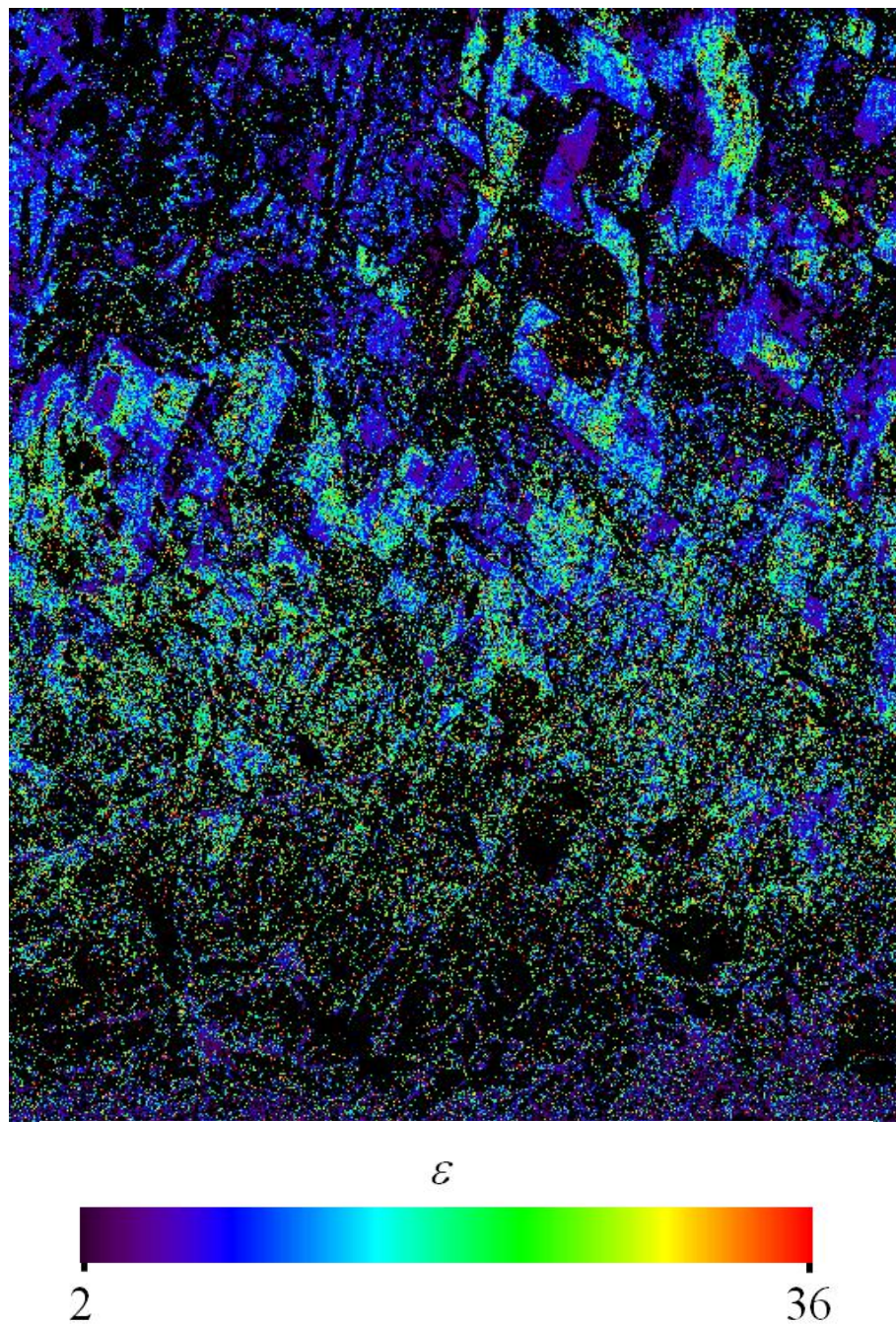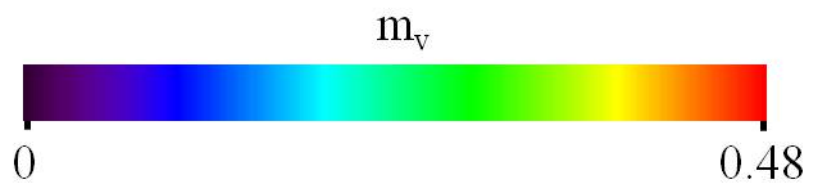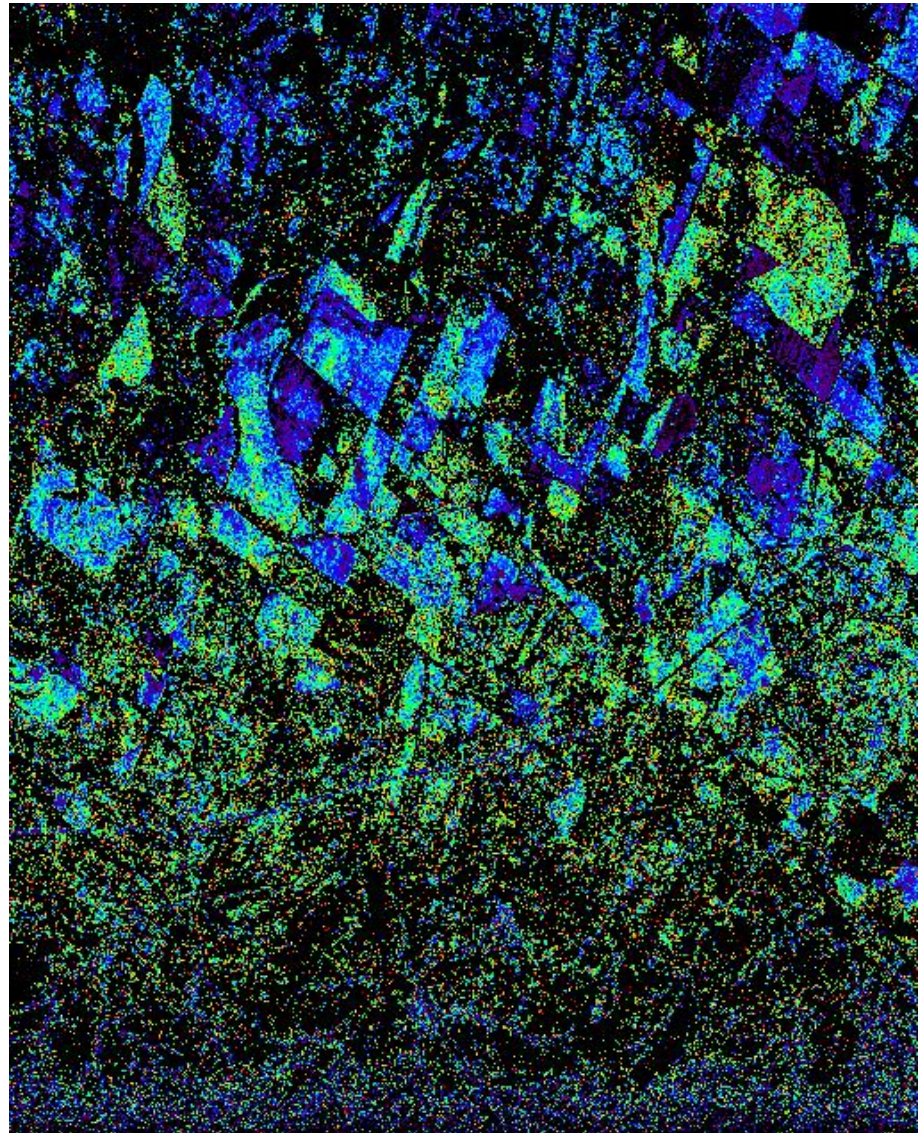
Figure 5.9: permittivity map relevant to the AIRSAR acquisition on 10/6/92 over Little Washita. Black pixels: parameter non retrieved.

m_v

0   0.48
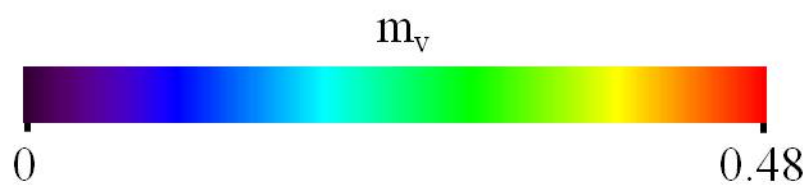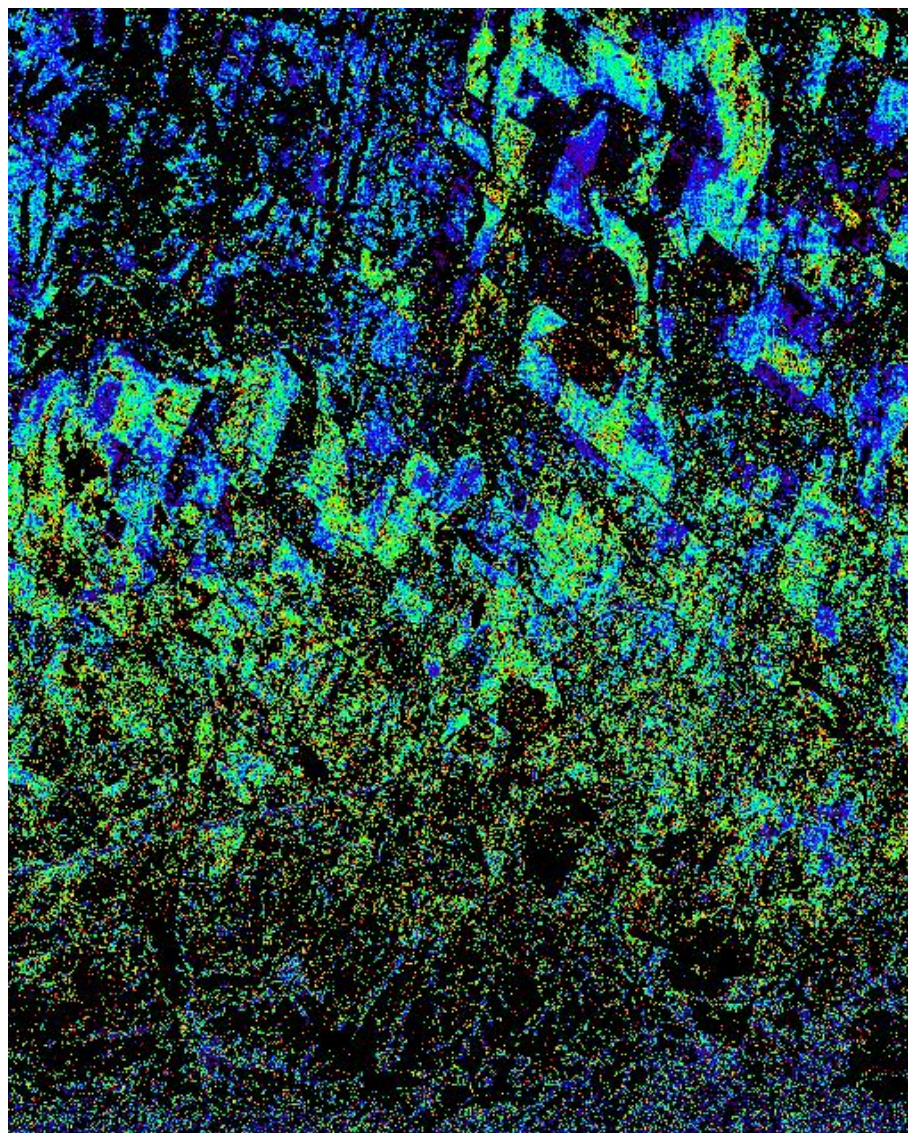
Figure 5.10: soil moisture map relevant to the AIRSAR acquisition on 10/6/92 over Little Washita. Black pixels: parameter non retrieved.

σ

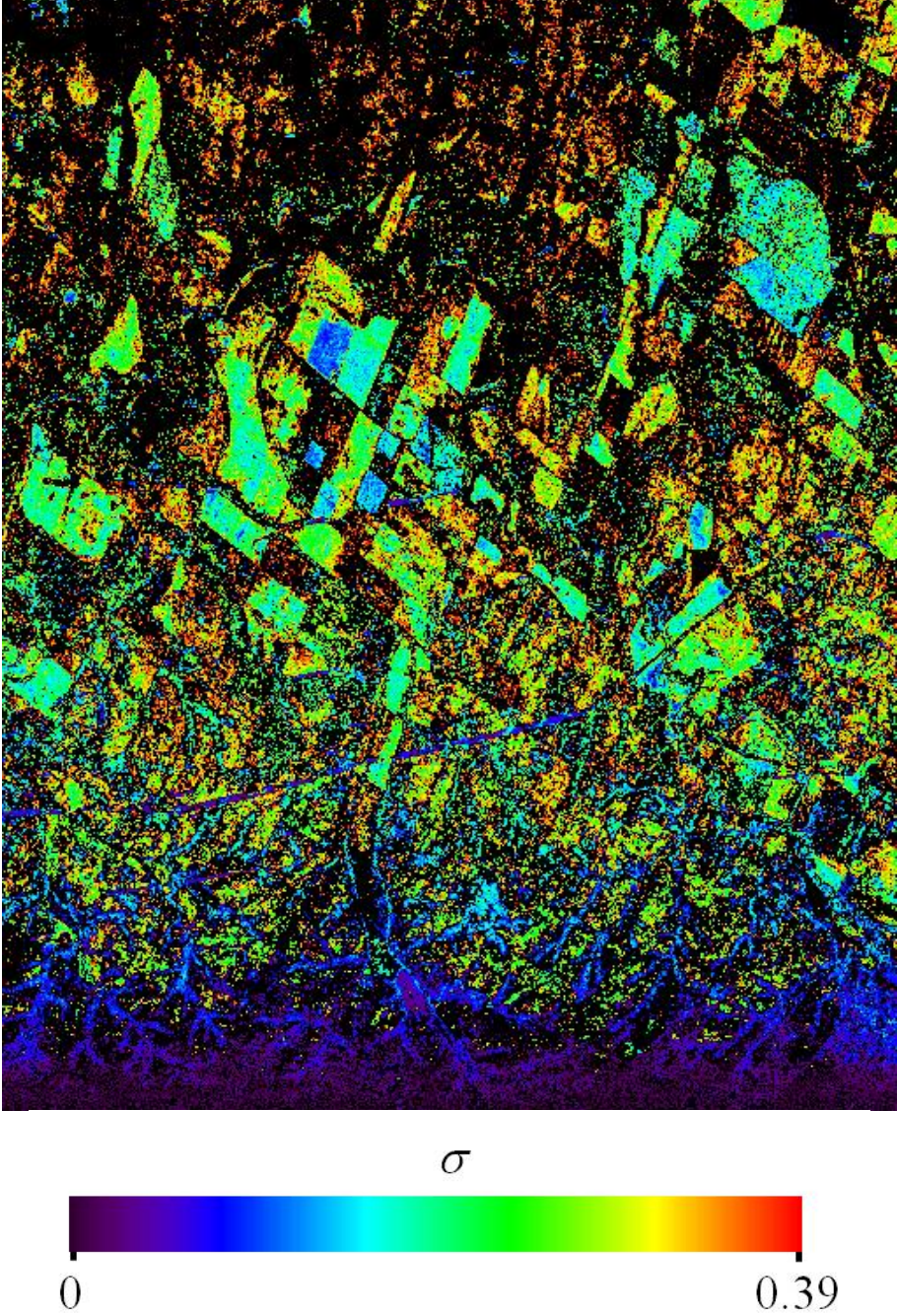0   0.39
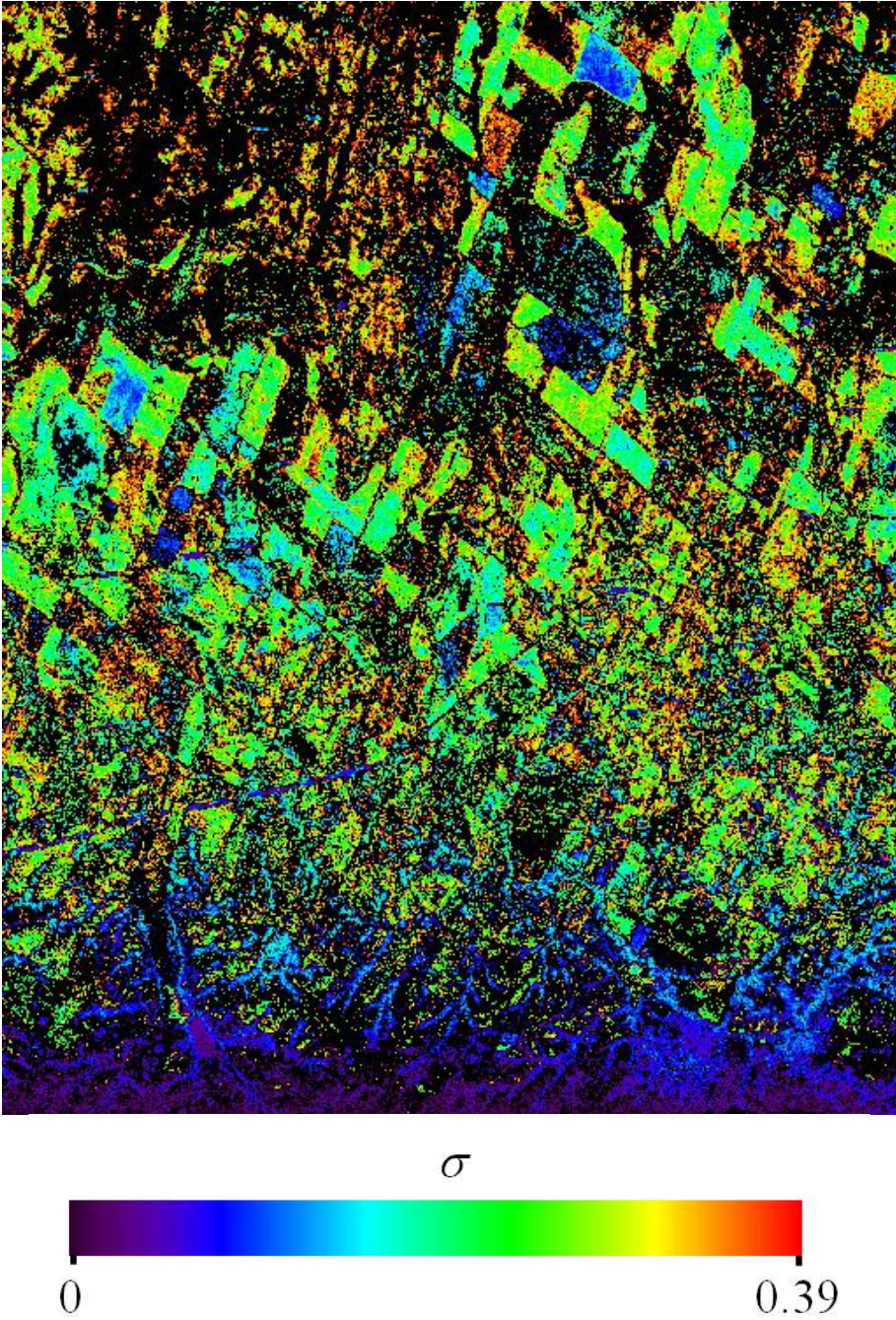
Figure 5.11: roughness map relevant to the AIRSAR acquisition on 10/6/92 over Little Washita. Black pixels: parameter non retrieved.

m_v

0   0.48
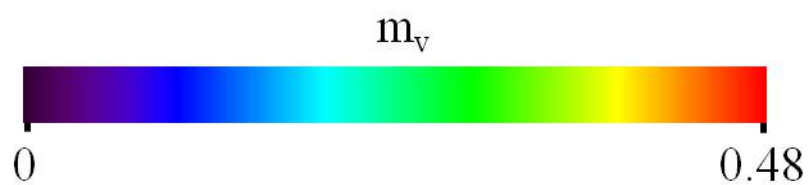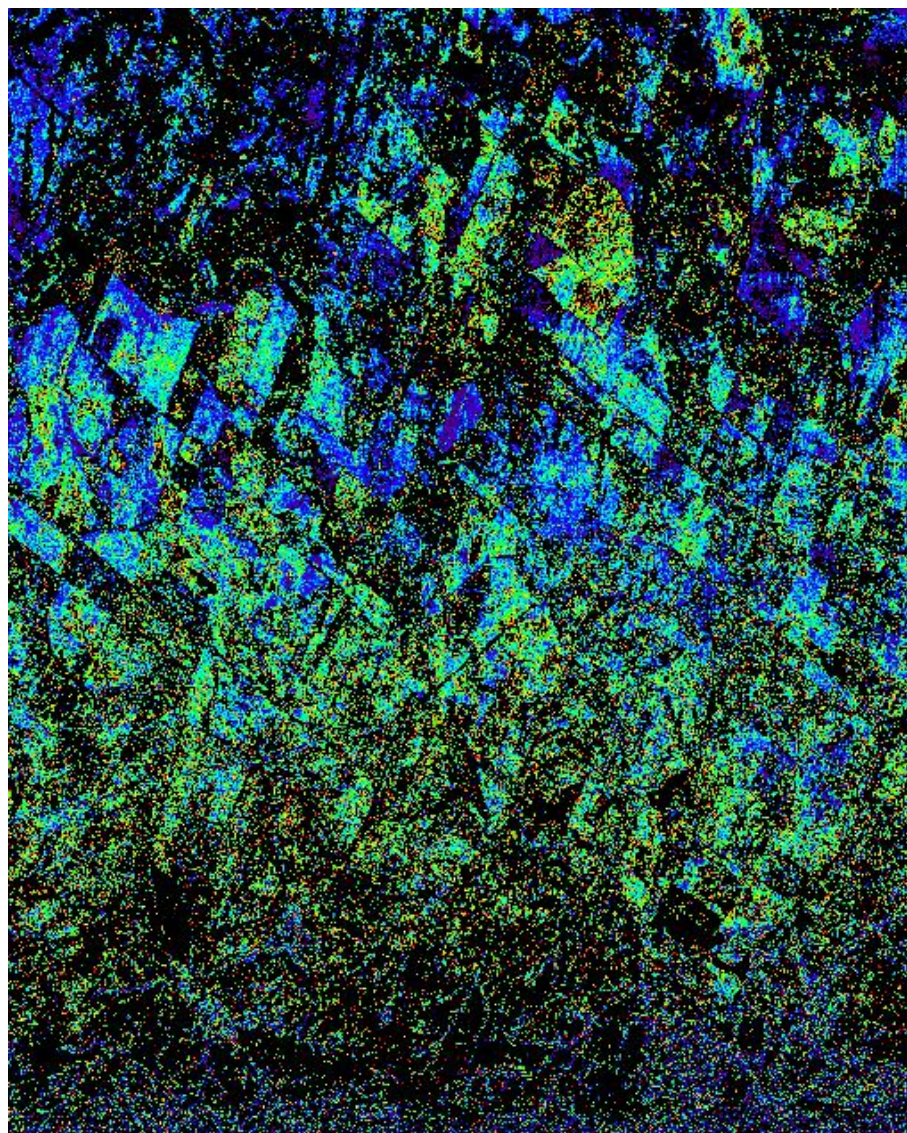
Figure 5.12: soil moisture map relevant to the AIRSAR acquisition on 13/6/92 over Little Washita. Black pixels: parameter non retrieved.

σ

0   0.39
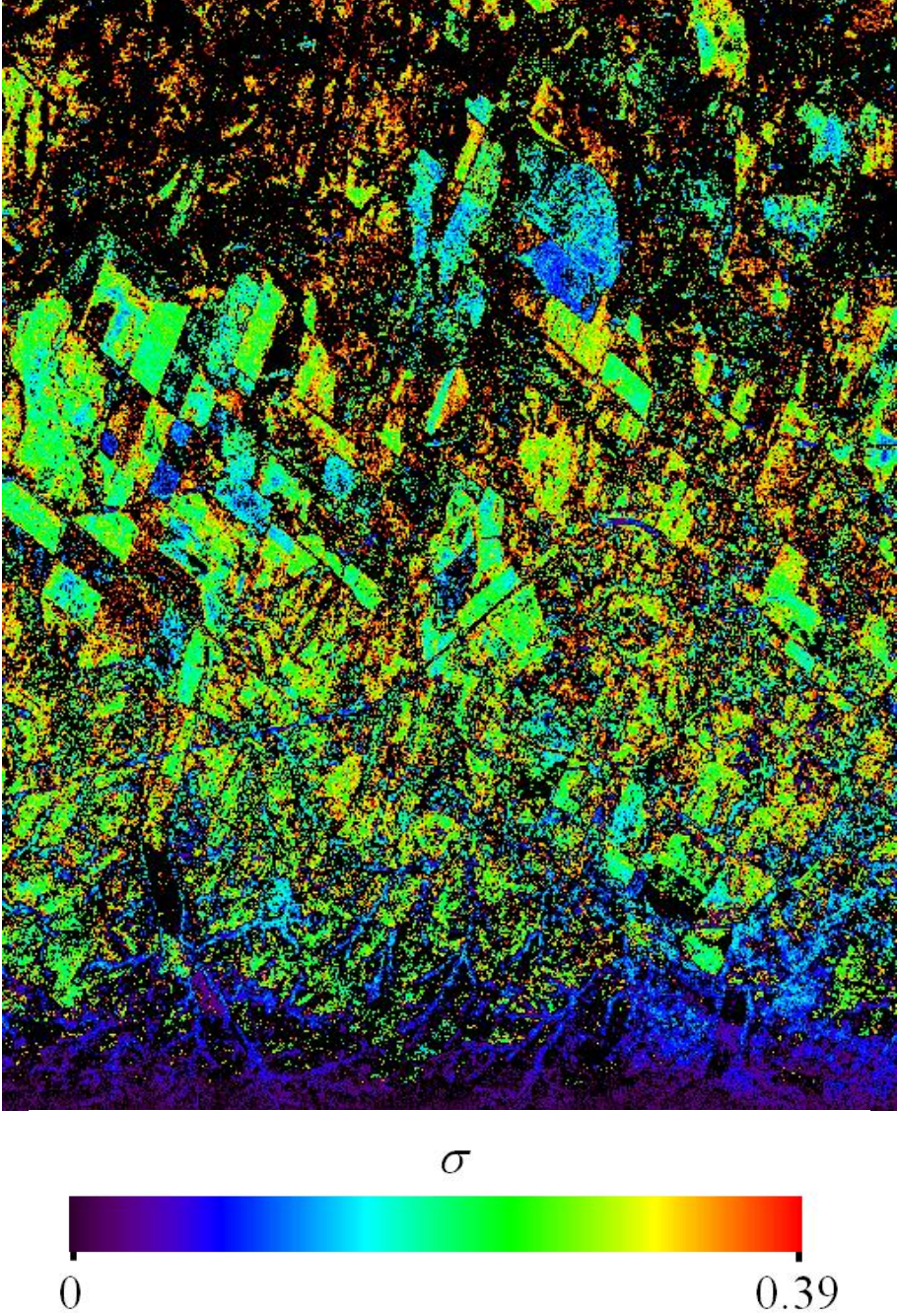
Figure 5.13: roughness map relevant to the AIRSAR acquisition on 13/6/92 over Little Washita. Black pixels: parameter non retrieved.

m_v

0   0.48

Figure 5.14: soil moisture map relevant to the AIRSAR acquisition on 18/6/92 over Little Washita. Black pixels: parameter non retrieved.

σ

0   0.39

Figure 5.15: roughness map relevant to the AIRSAR acquisition on 18/6/92 over Little Washita. Black pixels: parameter non retrieved.

5.2.2 Retrieval results at L band: the usage of DEM

In this section the retrieval procedure is performed on the very challenging case of the polarimetric ALOS/PALSAR dataset relevant to the mountainous area in the neighbourhood of Collazzone, in Italy. Accordingly, by using ALOS/PALSAR data (work frequency equal to 1.27 GHz) acquired in March 2009 (see Figure 5.16, in which the VV backscattering coefficient is depicted) at a radar look-angle of about 23° with a pixel spacing in range and azimuth coordinates of 10m x 3.65m, maps of estimate have been obtained, both considering and neglecting the information provided by the SRTM (Shuttle Radar Topography Mission) Digital Elevation Model (see Figure 5.17, where the image of the range slopes is shown), in order to get the mean value of the facet slopes in every pixel.

In particular, the soil moisture map (obtained from the permittivity map, using the Miller & Gaskin mixing model [11]) is shown in Figure 5.18, and the difference with the retrieved maps of Figures 5.10, 5.12 and 5.14 straightaway leaps out: indeed, in this case the retrieval algorithm returns allowable values of soil moisture only for a small percentage of pixels (the non-black ones). Most likely, this is due to the presence of dense vegetation in most part of the scene and to the small radar look-angle employed by PALSAR, which turns in a thickening of the image pixel distribution on the CP/XP dB-plane (see Figure 5.19) and in a consequent reduction of the PTSM sensitivity with respect to the dielectric constant (see Figure 5.3).

Unfortunately, no "in situ" measurements on this site were carried out at the same time of PALSAR acquisitions, and so a comparison between retrieved values and the ground truth cannot be performed. Nevertheless, to get an idea of how the slope-correction improves the performances of the retrieval algorithm, it is possible to compare retrieval results obtained by using information provided by the DEM with those obtained assuming $\mu_\omega=\mu_\gamma=0$ (i.e., ignoring the DEM) [1]. On this purpose, the histograms of retrieved pixels for the two considered methods, together with their difference, are depicted in Fig. 5.20.: as shown, a larger number of retrieved pixels is obtained after the compensation of the mean slopes for values of slopes higher than about 0.02 and lower than about 0.3. As expected, in flat areas no improvement is obtained from the use of DEM information.
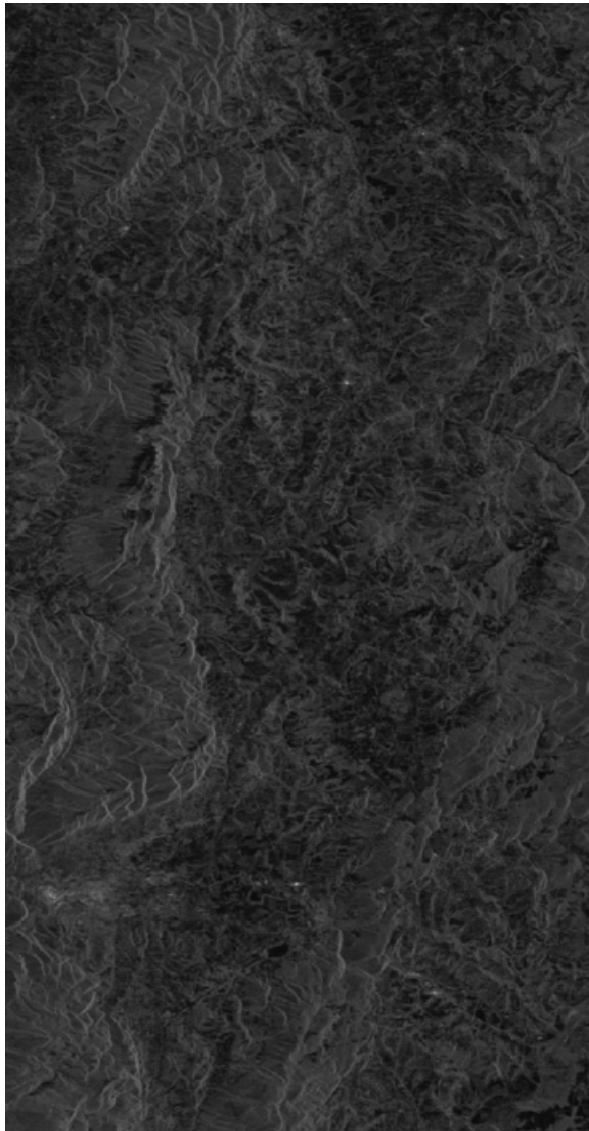
Figure 5.16: L band, σ_{vv} ALOS/PALSA image acquired on 30/3/09 over the Collazzone area.

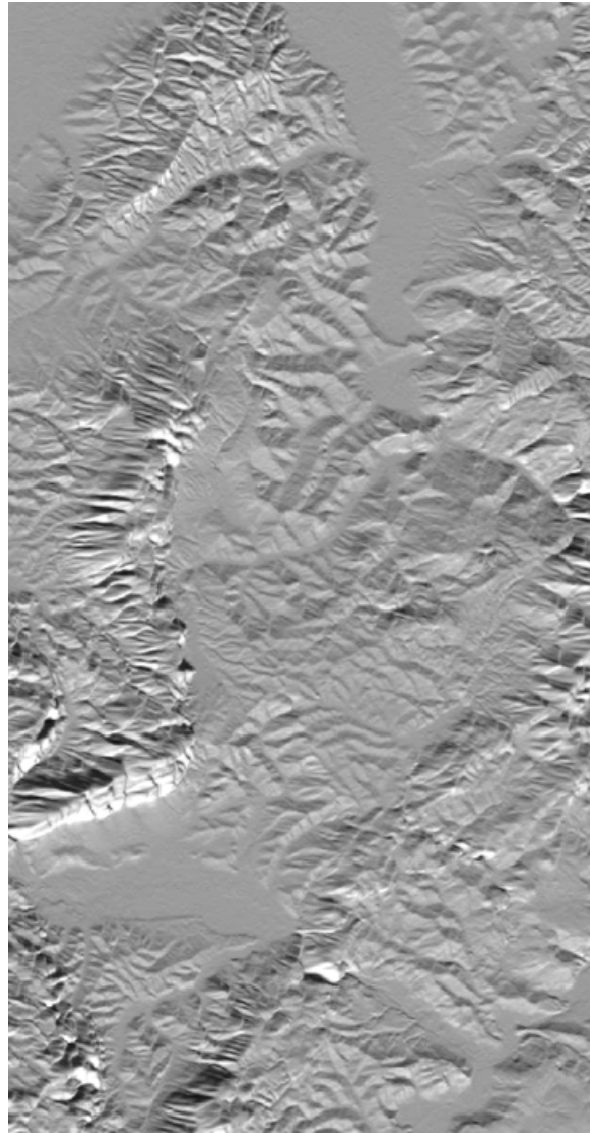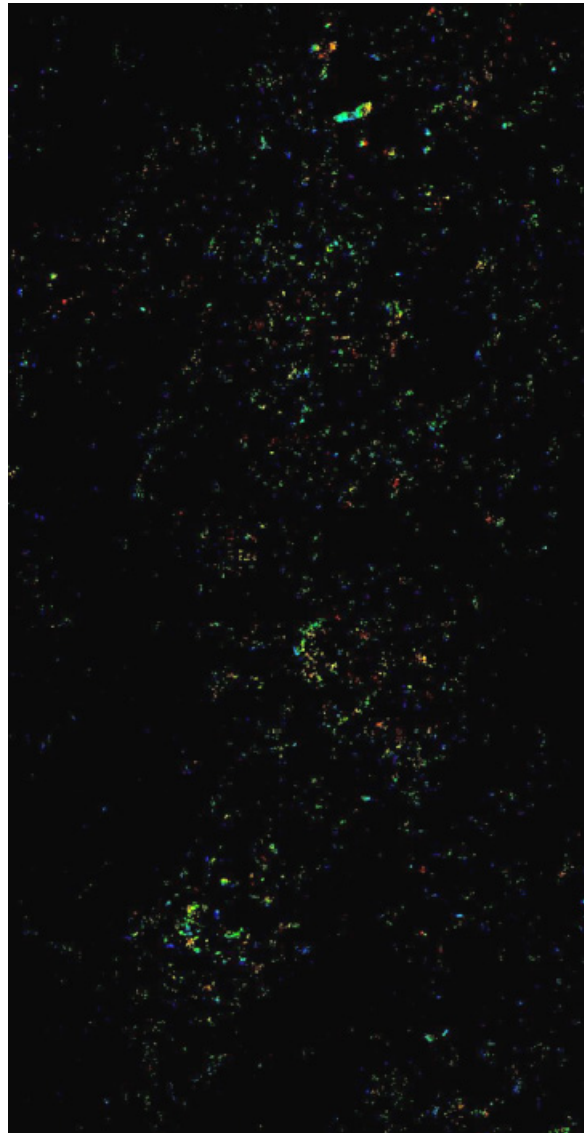**Figure 5.17: range slopes image obtained from the DEM of the neighbourhood of Collazzone.**

m_v

0   0.51

Figure 5.18: soil moisture map relevant to the ALOS/PALSAR acquisition over Collazzone. Black pixels: parameter non retrieved.
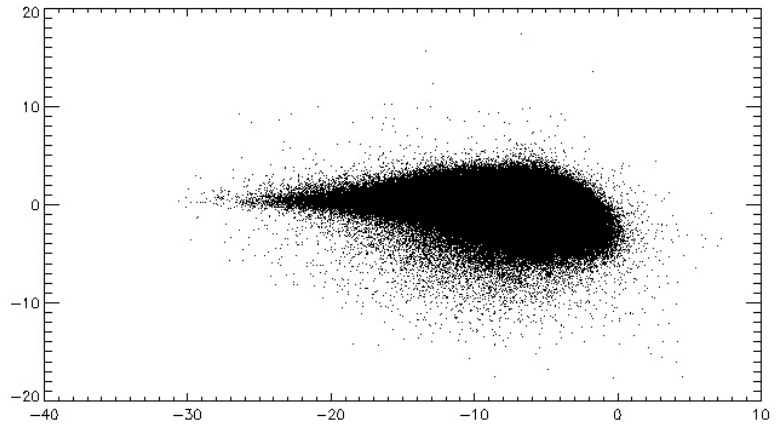
Figure 5.19: pixel distribution on the CP/XP dB-plane for the PALSAR dataset acquired on 31/03/2009 over the Collazzone area.

$$100\sqrt{\mu_\omega^2 + \mu_\gamma^2}$$
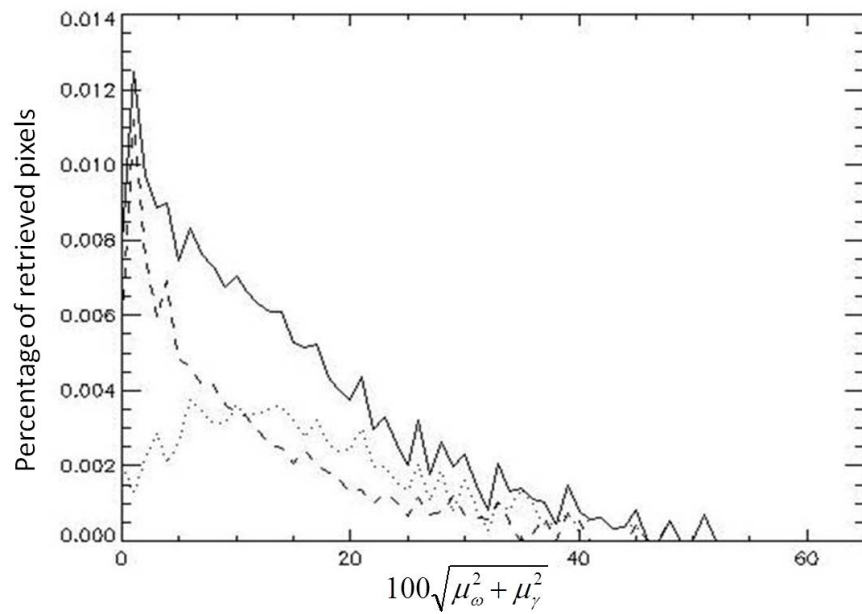
Figure 5.20: normalized number of retrieved pixels at the variance of the facet slopes obtained with (continuous line) and without (dashed line) the slope correction. The dotted line represents the difference between the two histograms.

5.2.3 Retrieval results at S band

In this subsection the backscattered coefficients acquired by the Astrium Ltd. airborne SAR demonstrator (work frequency equal to 3.2 GHz) are employed, to test the PTSM based retrieval algorithm on the not often inspected S band SAR data [17, 18].

In particular, the fully polarimetric sets acquired over the Marlborough area, in UK,(whose the HV NRCS are depicted in Figure 5.21-(a)), at a radar look-angle ranging from 10° to 43°, with a pixel spacing in range and azimuth coordinates of 0.835m x 0.35m are used to perform the estimate. As the area does not exhibit a significant topography, no DEM information has been exploited in the retrieving procedure.

It is clear, from Figures 5.22-(a) and (b), that the parameters are retrieved in only few fields, but in most of the pixels of the images the algorithm didn't succeed. Probably, this is due again to the presence of dense vegetation in most areas of the observed scene.

Unfortunately, also in this case no "in-situ" measurements were carried out at the same time of the SAR acquisitions, and so a comparison between retrieved values and the ground truth cannot be performed.

However, since both the amplitude and phase information are available, the Pauli decomposition (Section 2.1.5) has been performed on these polarimetric sets, in order to represent the dominant scattering mechanism for each pixel (see Figure 5.21-(b),wherein the volume, surface and double bounce scattering type components are coded in red, green and blue, respectively) and to have a qualitative measure of the algorithm performances. Accordingly, as expected, in Figure 5.21-(b) all the forestry areas are represented in a reddish color (as they are representative of the scattering from canopy) and they are substantially the areas for which the algorithm does not return an allowable retrieval result.

Conversely, in most of the areas classified in shade of blue or green, the algorithm works and, even if a comparison with the ground truth cannot be performed, it seems to return reasonable values.
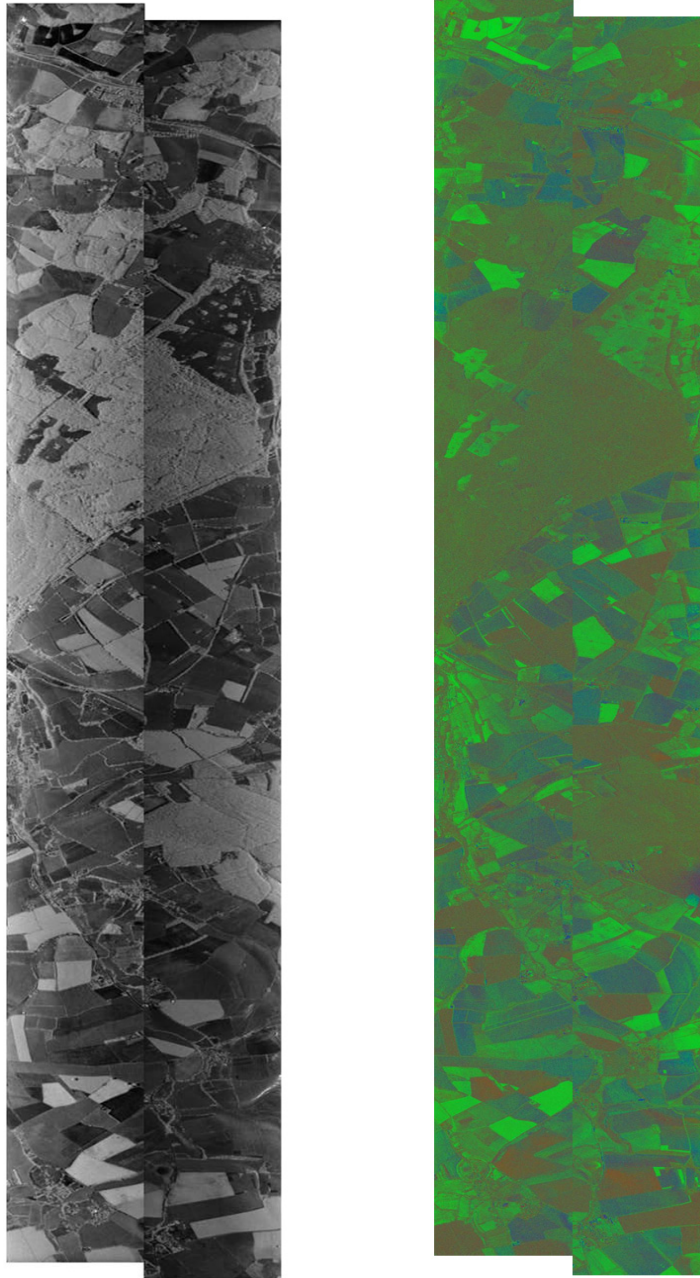
(a)   (b)

Figure 5.21: S band, σ_{hv} Astrium images (a) and the relevant RGB-coded Pauli decompositions (b) for the Marlborough area.

m_v

σ

0   0.52   0   0.39
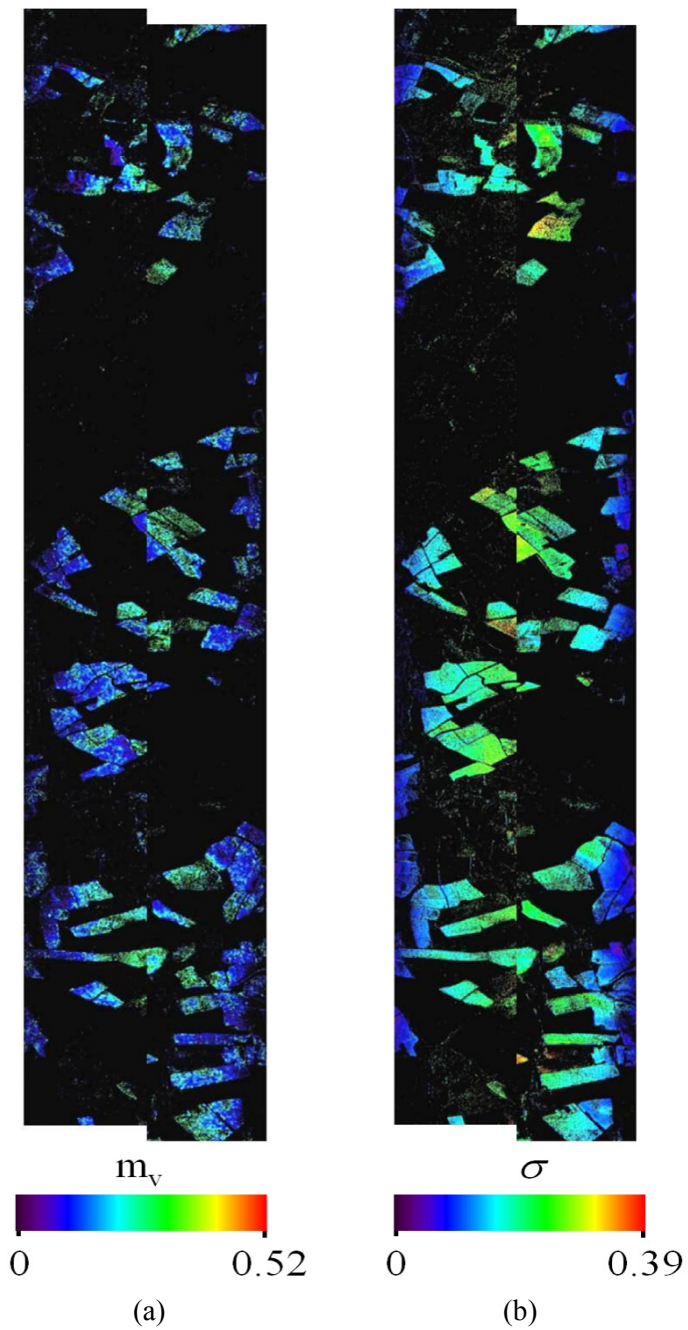
(a)   (b)

Figure 5.22: soil moisture (a) and roughness (b) retrieved map for the Marlborough area. Black pixels: parameter non retrieved.

5.2.4 Retrieval results at X band

In this section retrieval results at X band are finally discussed. In particular, here are considered COSMO-SkyMed images (work frequency equal to 9.6 GHz) acquired on 03/05/2010 (VV and VH channels) and 04/05/2010 (VV and HH channels) over the area of Collazzone, in Italy, at a look-angle of 40° with a pixel spacing in range and azimuth coordinates of 10 m x 10 m, and again the retrieval procedure is performed on these data, obtaining the soil moisture and roughness map depicted in Figures 5.24 and 5.25. As it might be expected, due to the higher frequency, the measured NRCS tend to cover a narrow region on the CP/XP the dB-plane (see Figure 5.23) and the overall appearance of the retrieval maps in X band turns out to be noisier than L and S band ones.Unfortunately, in situ measurements in conjunction with COSMO-SkyMed acquisitions are not available until now, so a direct method validation at X band cannot be provided. However, just to get an idea of the potentialities of the PTSM at X band, a simulated COSMO-SkyMed image is here used. In particular, COSMO-SkyMed parameters has been exploited to simulate [19] bare soil SAR images at the variance of the permittivity and the roughness (see Figure 5.27). Accordingly, the X-Bragg, Shi and Oh retrieval techniques has been performed on this simulated data set, but in this case only the PTSM provides physically meaningful results (see Table IV), while other methods provide retrieval results out of the reasonable ranges (permittivity values lower than 2 or larger than 40).
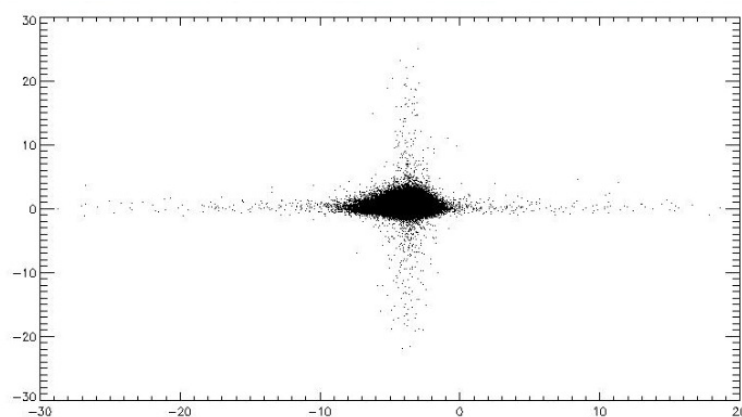

Figure 5.23: pixel distribution on the CP/XP dB-plane for the COSMO-SkyMed dataset over Collazzone.
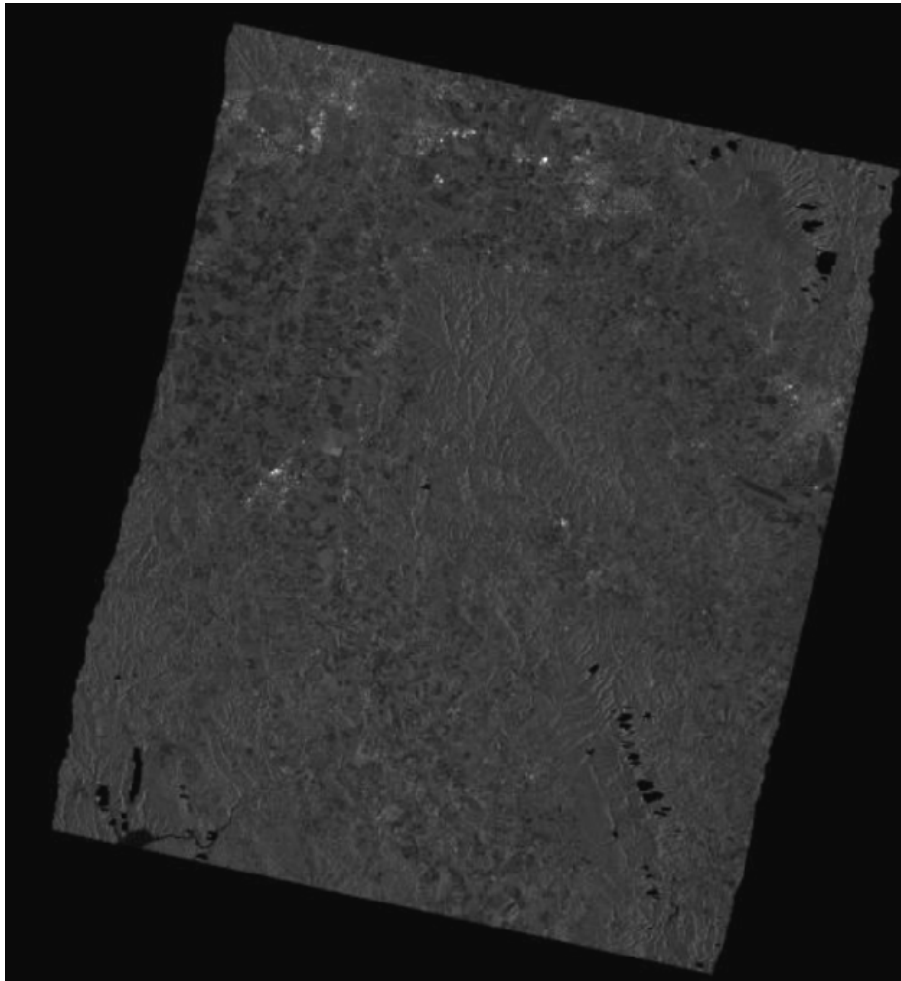
Figure 5.24: X band, σ_{hh} COSMO-SkyMed image acquired on 04/05/2010 over Collazzone.
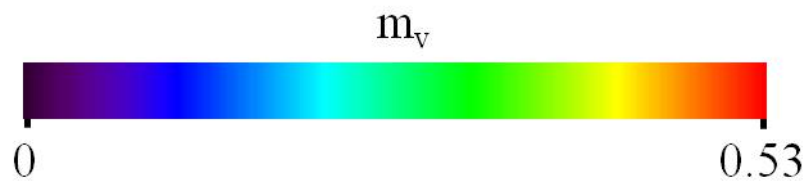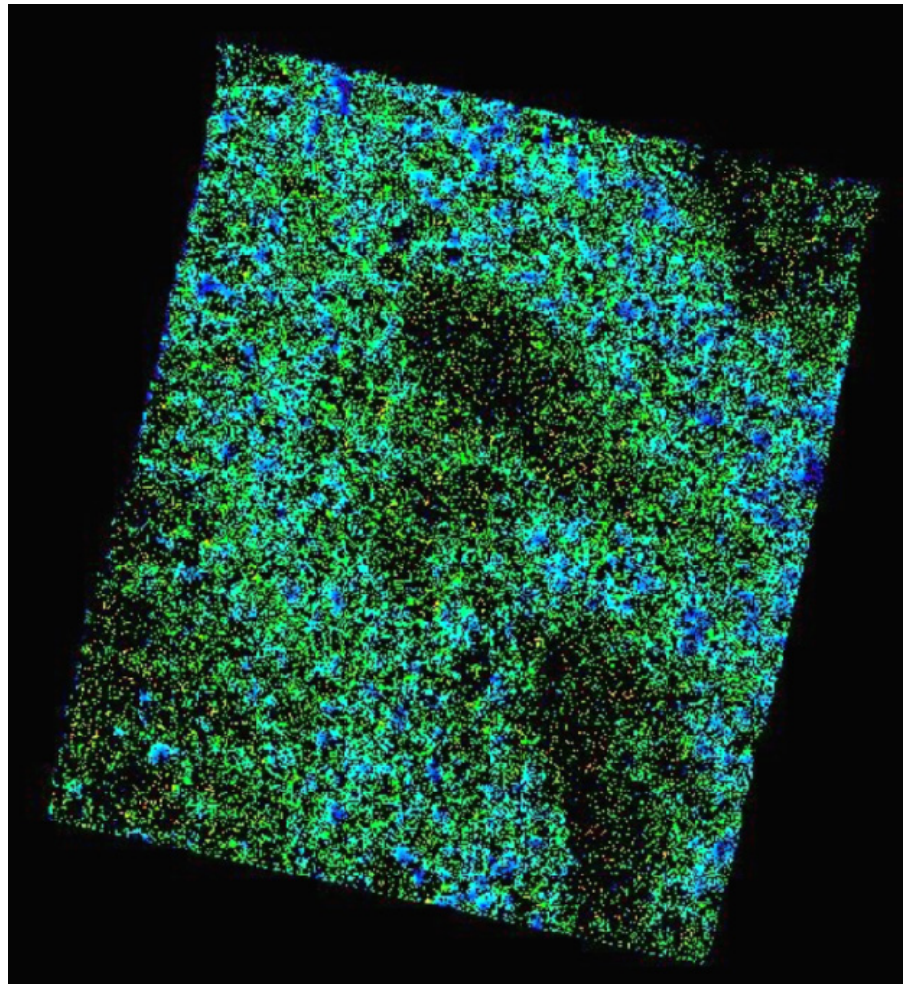
Figure 5.25: soil moisture map relevant to the COSMO-SkyMed acquisition over Collazzone. Black pixels: parameter non retrieved.
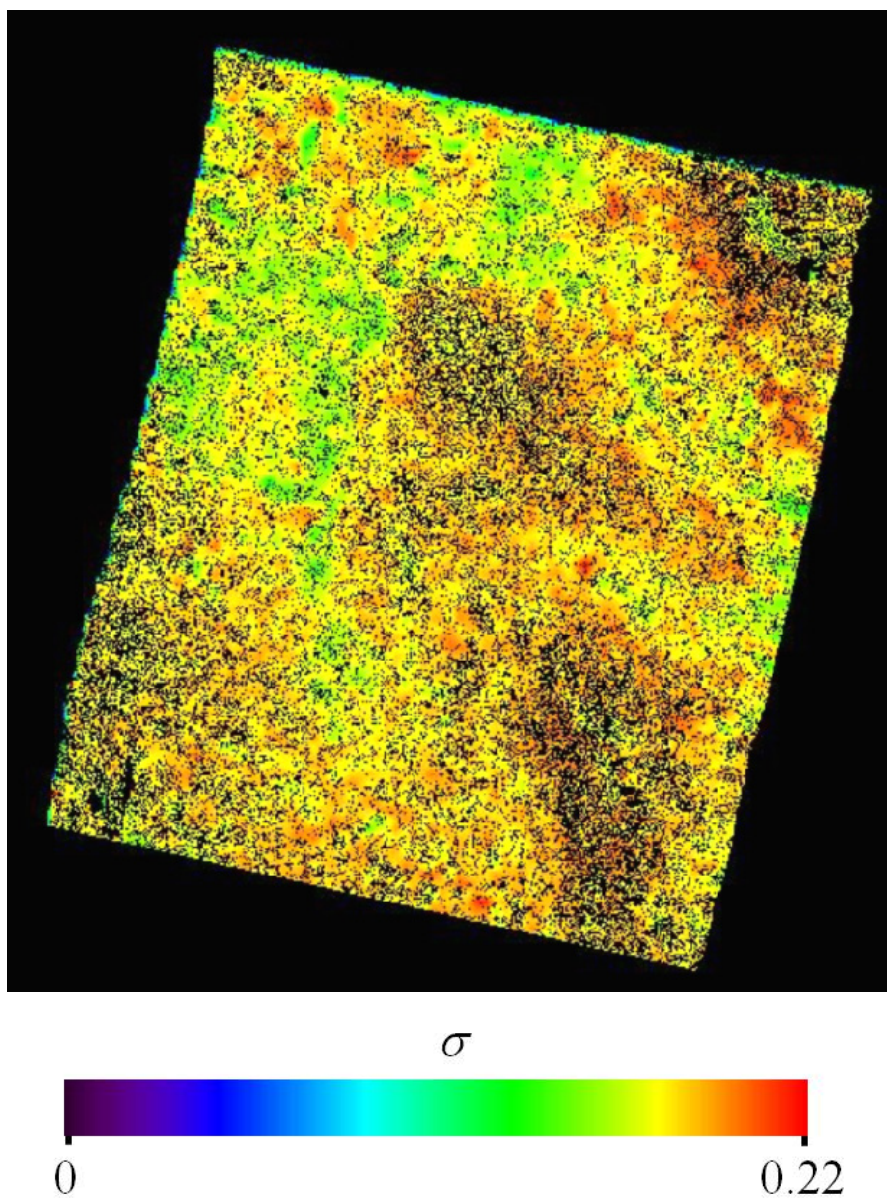
Figure 5.26: roughness map relevant to the COSMO-SkyMed acquisition over Collazzone. Black pixels: parameter non retrieved.
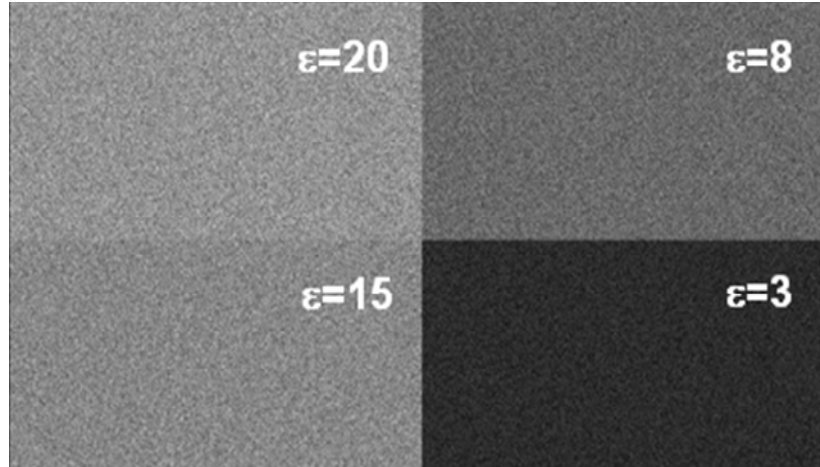
Figure 5.27: simulated COSMO-SkyMed image with areas with different relative dielectric constants.

Table IV

PERMITTIVITY RETRIEVAL RESULTS FOR SIMULATED COSMO-SKYMED DATA

Simulated ε	$\sigma = 0.01$	$\sigma = 0.1$
3	3.31	2.55
8	8.27	6.64
15	15.00	12.2
20	20.00	16.2

References

[1] A. Iodice, A. Natale, D. Riccio, "Retrieval of Soil Surface Parameters via a Polarimetric Two-Scale Model in Hilly or Mountainous Areas", in *Proceedings of SPIE 2011*, Prague, 2011.

[2] A. Iodice, A. Natale, D. Riccio, "Retrieval of Soil Surface Parameters via a Polarimetric Two-Scale Model", *IEEE Transactions on Geoscience and Remote Sensing,* vol. 49, no. 7, pp. 2531-2547, July 2011.

[3] A. Iodice, A. Natale, D. Riccio, "A Polarimetric Two-Scale Model for the Soil Moisture Content Retrieval", in *Proceedings of the International Geoscience and Remote Sensing Symposium IGARSS2010*, Honolulu 2010.

[4] A. Iodice, A. Natale, D. Riccio, "Un modello polarimetrico a due scale per la stima dei parametri superficiali del suolo", in *Proceedings of Riunione Nazionale di Elettromagnetismo RiNEM2010*, Benevento, 2010.

[5] A. Iodice, A. Natale, D.Riccio, "A Physical Optics-based Polarimetric Two-Scale Model", in *Proceedings of URSI Commission F, Microwave Signatures 2010*, Firenze 2010.

[6] F. del Monaco, N. De Quattro, A. Iodice, A. Natale, "Extended Small Perturbation Method and Retrieval of Natural Surface Parameters", *Proceedings of the 6th European Radar Conference*, Rome, 2009.

[7] A. Iodice, A. Natale, D. Riccio, "An SPM/PO-based Polarimetric Two-Scale Model", accepted for publication on the special issue of *The Italian Journal of Remote Sensing*, tbe 2012.

[8] H. T. Hallikainen, F. T. Ulaby, M. C. Dobson, M. A. El-Rayes, L. K. Wu, "Microwave dielectric behavior of wet soils - Part I: Empirical models and experimental observations", *IEEE Transactions on Geoscience and Remote Sensing*, vol. 23, pp 25-34, January 1985.

[9] J. R. Wang, T. J. Schmugge, "An Empirical Model for the Complex Dielectric Permittivity of Soils as a Function of Water Content", *IEEE Transactions on Geoscience and Remote Sensing*, vol. 18, no. 4, pp. 288–295, October 1980.

[10] G. C. Topp, "Electromagnetic Determination of Soil Water Content: Measurements in Coaxial Transmission Lines", *Water Resources Research*, vol 16, no. 3, pp. 574-582, June 1980.

[11] J. D. Miller, G. J. Gaskin, "Theta Probe ML2x Principles of Operation and Application", *MLURI Technical Note (2nd edition)*, Delta-T Devices (Cambridge) and MaCaulay Land Use Research Institute (Aberdeen), 1999.

[12] G. Franceschetti, A. Iodice, S. Maddaluno, D. Riccio "A fractal based theoretical framework for the retrieval of surface parameters from electromagnetic backscattering data", *IEEE Transactions on Geoscience and Remote Sensing*, vol. 38, no. 2 , pp. 641-650, March 2000.

[13] I. Hajnsek, E. Pottier, S. R. Cloude, "Inversion of surface parameters from polarimetric SAR", *IEEE Transactions on Geoscience and Remote Sensing*, vol. 41, no. 4, pp. 727–744, April 2003.

[14] Y. Oh, K. Sarabandi, F. T. Ulaby, "An empirical model and an inversion technique for radar scattering from bare soil surfaces", *IEEE Transactions on Geoscience and Remote Sensing*, vol. 30, pp. 370–381, March 1992.

[15] http://hydrolab.arsusda.gov/washita92/wash92.htm

[16] J. Shi, J. Wang, A. Y. Hsu, P.E. O'Neill, E. Engman, "Estimation of bare surface soil moisture and surface roughness parameter using L-band SAR image data", *IEEE Transactions on Geoscience and Remote Sensing*, vol. 35, no. 5, pp. 1254–1266, September 1997.

[17] R. Guida, A. Natale, R. Bird, P. Whittaker, D. Hall, M. Cohen, "Demonstration and analysis of the applications of S-band SAR", in *Proceedings of APSAR 2011*, Seoul 2011.

[18] R. Guida, A. Natale, R. Bird, P. Whittaker, D. Hall, M. Cohen, "Validation of S-band data performance for future spaceborne SAR missions", accepted for publication in *Proceedings of EUSAR 2012*, Nuremberg 2012.

[19] G. Franceschetti, M. Migliaccio, D. Riccio, G. Schirinzi, "SARAS: a Synthetic Aperture Radar (SAR) raw signal simulator", *IEEE Transactions on Geoscience and Remote Sensing*, Vol. 30, No 1, January 1992.

Summary and conclusions

In this thesis polarimetric two-scale surface scattering model (PTSM) has been introduced and employed to retrieve the surface parameters of bare soils from polarimetric SAR data. Unlike other similar existing approaches, here large-scale-roughness induced random variations of both local incidence angle and local incidence plane have been considered, and their statistical modeling has not been arbitrarily chosen, but it has been derived from a proper statistical description of the scattering surface. The model can be applied to scenes with a significant topography, as it also provides the opportunity to get information from Digital Elevation Models in order to account for a non-zero-mean terrain slope within a resolution cell.

The forecasts on the power density of the diffuse field provided by the PTSM represented the core on which the developed estimate procedure has been founded. In particular, the proposed retrieval algorithm returns the permittivity, soil moisture and (large scale) roughness estimate maps from measured co-pol cross-pol ratio. It is worth noting that the proposed method only requires the amplitudes of the three polarimetric channels, whereas phase information is not needed. Accordingly a wide variety of SAR data, acquired at different bands has been employed, to provide retrieval results and to test the performances of the model.

In particular, presented results at L band show that the proposed technique is very promising, as the retrieved values are in very good agreement with the available ground truth. Although for the moment "in situ" measurements are only available for flat areas, an indirect validation has been presented for a region with a significant topography.

Concerning the performances at S band, the method has been tested on a natural area, where it succeeds in most of the bare soil fields

Although no "in situ measurements" were executed on this site at the same time of the sensor acquisitions, retrieval results seems to be reasonable and in accordance with the features of the scene.

Finally, as regards estimate maps at X band, of course they appear more noisy than those obtainable at lower bands, even if a comparison with simulated data show good potentialities of the retrieval procedure also in the high frequency case.

Besides, a second original contribution presented in this work regards the physical reading of the Kirchhoff Approach (KA) solution for the electromagnetic scattering from natural surfaces. Accordingly, first of all, it has shown that the Kirchhoff scattering pattern of an fBm (fractional Brownian motion) surface is proportional to the probability density function (pdf) of a symmetric alpha-stable 2D random variable, whose dispersion parameter γ is related to the variance of fBm surface slopes, as observed at the electromagnetic wavelength scale. Such a pdf that can be interpreted as the pdf of the slopes of an equivalent rough surface whose GO (Geometrical Optics) scattered power density is equal to the scattered power density of the actual fBm surface.

In order to give a physical interpretation to this interesting result, it has been stated that the fBm surface Kirchhoff scattering pattern expression can be interpreted by considering the overall fBm surface as composed of many rough surface elements large with respect to the wavelength, so that the mean square value of the overall scattered field is obtained by averaging the scattering diagrams of rough surface elements over the their slopes, as observed at the wavelength scale. This is in some analogy with the usual two-scale or composite surface methods, with the important difference is that the surface multi-scale behavior is "intrinsically" taken into account by the scattering formulation, so that no artificial separation, or cut-off, scale need to be defined.